EXPLORING DRIVEN, HIGH LUNDQUIST NUMBER MAGNETIC RECONNECTION IN THE LABORATORY: STUDIES OF SUB-ION SCALE PLASMOIDS, AND THE INTERPLAY BETWEEN SHOCKS AND MAGNETIC FLUX PILEUP

by

Joseph Olson

A dissertation submitted in partial fulfillment of
the requirements for the degree of

Doctor of Philosophy

(Physics)

at the

UNIVERSITY OF WISCONSIN–MADISON

2020

Date of final oral examination: July 2, 2020

The dissertation is approved by the following members of the Final Oral Committee:

Jan Egedal, Professor, Physics
Cary Forest, Professor, Physics
John Sarff, Professor, Physics
Carl Sovinec, Professor, Engineering Physics

Don’t let the perfect be the enemy of the good.

Common Aphorism

EXPLORING DRIVEN, HIGH LUNDQUIST NUMBER MAGNETIC RECONNECTION IN THE LABORATORY: STUDIES OF SUB-ION SCALE PLASMOIDS, AND THE INTERPLAY BETWEEN SHOCKS AND MAGNETIC FLUX PILEUP

Joseph Olson

Under the supervision of Professor Jan Egedal
At the University of Wisconsin-Madison

A new experiment for studying magnetic reconnection, the process in a magnetized plasma which allows for the magnetic topology to change rapidly, has been constructed and is currently in operation. Magnetic reconnection is of great interest because while it occurs in localized regions, it influences the macroscopic behavior of many plasmas systems including space and astrophysical plasmas as well as laboratory experiments. An emerging frontier of reconnection research has been the study of collisionless magnetic reconnection in Earth's magnetosphere. Extensive studies in theory, simulation, and spacecraft observations have been successful in developing our understanding of these systems while there are few laboratory experiments capable of exploring similar parameters. The Terrestrial Reconnection Experiment (TREX) marks the first experiment dedicated to the study of these kinetic effects in low collisional plasmas.

In operation at the Wisconsin Plasma Physics Laboratory (WiPPL), TREX has undergone multiple hardware upgrades in order to access new regimes of reconnection. The experiment consists of a large spherical vacuum vessel housing internal reconnection drive coils that force magnetic reconnection with a background plasma. This generates a strong toroidal current layer near the coils that is driven inward to the central axis as reconnection proceeds. An extensive suite of magnetic and electrostatic diagnostics allow for fine measurement of the local and global dynamics of the system.

Two important results are reported in this thesis. The first is the direct observation of the spontaneous formation of plasmoids, or magnetic islands, which occur at the electron scale inside the ion diffusion region. The experiments show that the plasmoid instability, a fundamental ingredient in models for electron energization and increased reconnection dynamics, is active at a smaller system size than predicted by theory. The second investigation examines the dynamics of strongly driven magnetic reconnection in which a shock interface between the supersonically driven plasma inflow and a region of magnetic flux pileup develops. The observations elucidate the role of shock formation in permitting the normalized reconnection rate to self regulate to a fixed value.

To Hollie

ACKNOWLEDGMENTS

Nearly eight years ago, I started my graduate school career at UW–Madison with little more than a vague idea of what I was getting myself into and where this journey would lead. Now, after an incredible amount of work and dedication, I've realized that this is merely a jumping off point for the next stages in life and I still have no idea where this all ends. What I do know is the same people who helped and supported me throughout this journey will still be there for the next one. I write these thanks as a small token of the enormous gratitude and appreciation for what they've all done for me.

I would first like to thank Professor Jan Egedal, my faculty advisor and mentor, who was the driving force behind all the scientific investigations throughout my PhD. Jan taught me so much about being a physicist and how to conduct research through his active involvement in the work as well as his willingness to let me make and fix my own mistakes. His ability to laser focus on a new task until its completion is awe inspiring and his natural physical intuition is something I greatly admire. I consider myself extremely fortunate to have been able to work with and learn from Jan. I also owe a lot to Professor Cary Forest, who acted as an unofficial co-advisor to me. I'm not sure what would have happened without his initial endorsement for Jan to bring me on as a student. Cary is truly a "big idea" type of guy, always looking ahead to the next big thing, and it can be quite a challenge to keep up. Having gone through the process, I believe I'm prepared for anything future research can throw at me.

I had the pleasure of working with essentially two separate research groups for my PhD, TREX and BRB. As the only student on TREX when I started, I was adopted by the BRB group and couldn't be happier with the people I ended up doing the majority of my work with. I'm delighted that I've gotten to know and work with Dr. Ethan Peterson, Dr. Jason Milhone, Dr. Ken Flanagan, and (basically a Dr.) Doug Endrizzi, and I treasure the friendships that we've created. A lot of thanks go to Sam Greess, Rachel Myers, and Alex Millet-Ayala for their contributions to the TREX facility, development of diagnostics, and their willingness to help run the experiment during some long days and nights. Huge thanks go out to John Wallace and Mike Clark, the engineers on the BRB and TREX. If you need something done, they'll find a way to do it, and the lab truly wouldn't run without their efforts. Thanks also go to Paul Nonn and Bill Zimmerman who I learned most of my electrical and fabrication skills from and enjoyed numerous conversations with throughout my years. I also gleaned a lot from former students and post-docs, Dr. Matt Brookhard, Dr. Dave Weisberg, and Dr. Chris Cooper, who were willing to share their knowledge with a naive graduate student.

Special thanks goes to PLU Professors Katrina Hay, Bogomil Gerganov, Bret Underwood, Bill Greenwood, and Rich Louie. With PLU Physics being such a close knit department, each one has contributed to my career in lasting ways, and I cherish the education that I received. These thanks also extend to my time before my continued education, to the many teachers who encouraged me throughout the years and helped foster my curiosity and wonder in the world.

Looking back, there's no single defining moment that lead me down this path of higher education. I do know that growing up I was never told I couldn't accomplish something, so why not try it all? Without the constant love and support from my family, I would never have the courage to do all that I've done. So, to Mom and Dad, thank you for everything. Dawn-Marie, you've been with me as long as most people through all this and I'm blessed to call you family. To Dan, I wish you could have been around for this and I know you would have been so proud. To my siblings, Jordan, Jake, Amy, and Dallas, thank you all for being there to help bring my mind back from the tedium of grad school.

Finally, the utmost gratitude goes to my spouse and partner, Hollie. This is as much your accomplishment as it is mine. You've been through all of this just as I have, and I admire your dedication and support throughout. I couldn't be more thankful that you followed me to Madison for this chapter in our lives. I am so grateful to share this with you and can't wait to see what comes next. Together, I'm sure it will be amazing.

TABLE OF CONTENTS

Page

Page

LIST OF TABLES

LIST OF FIGURES

Figure Page

Figure Page

Chapter 1

Introduction

1.1 Our Explosive Solar System

From the farthest galaxies to our own magnetosphere, space is filled with magnetized plasmas. The basic properties and processes of these charged particles and their interaction with electric and magnetic fields play an important role in the dynamics of such systems. One such process is known as magnetic reconnection which describes the breaking and rearranging of the magnetic field in a plasma [1]. This process typically occurs very rapidly and permits the release of built up magnetic stress into plasma flows and heating. It is this energy conversion which is thought to be a critical mechanism for particle energization throughout space.

Observations of often explosive solar dynamics originally inspired the first theories on magnetic reconnection in the 1950s [2, 3, 4]. It is now understood that reconnection drives the evolution of solar flares and coronal mass ejections (CMEs) [5, 6]. Figure 1.1 shows one such event, the burst of a solar flare and the large mass of plasma that is ejected at high energies away from the sun as a CME. Typically, emanating from the solar corona is a constant stream of plasma, dragging the solar magnetic field with it in what's known as the solar wind, permeating throughout the Solar System. As the solar wind flows past Earth it reconnects at the dayside magnetopause [7] and then drags the magnetosphere away from the sun, driving reconnection again in the magnetotail. Events like those in Figure 1.1 disrupt this steady drive from the solar wind and lead to much more

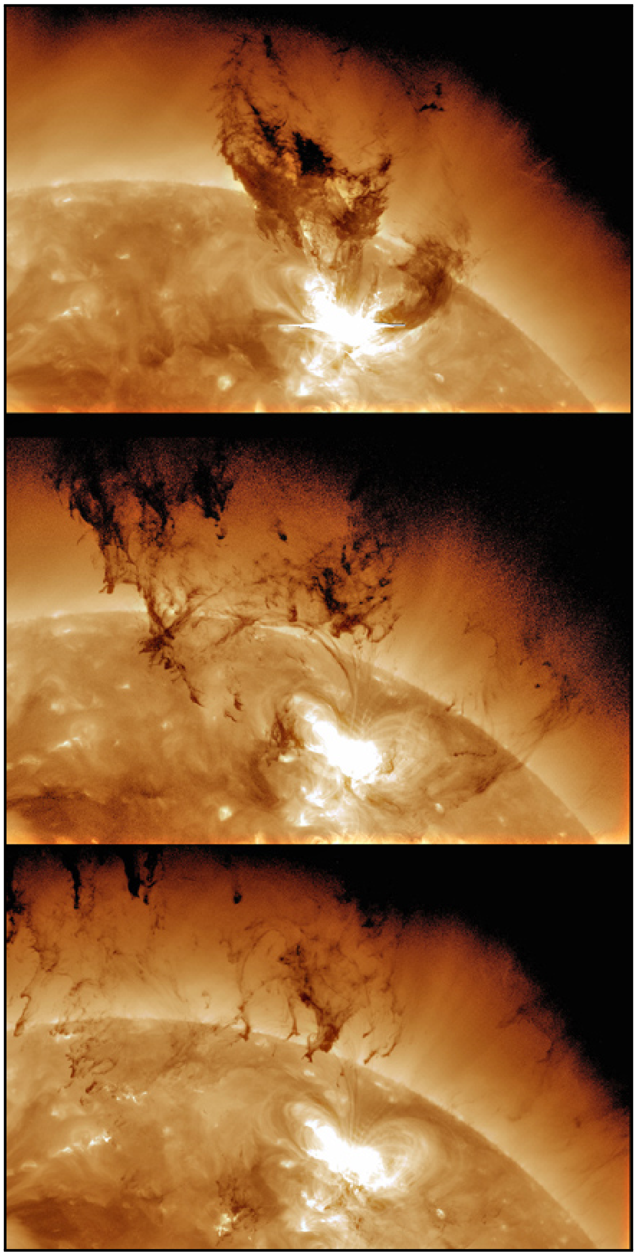

Figure 1.1: Images of the Sun taken over a 30 minute period, starting from the top down, showing a medium sized solar flare (the bright flash) and subsequent CME (the dark material). These images were recorded by the Solar Dynamics Laboratory (SDO) on June 7, 2011 at 193 Å (extreme ultraviolet wavelength). SDO is a NASA mission launched to study variations in solar activity and its impact on Earth (from sdo.gsfc.nasa.gov).

impulsive reconnection behavior, driving magnetospheric substorms that result in magnificent auroral displays near the poles [8]. Over the past several decades, there have been numerous space satellites and probes, like NASA's Magnetospheric Multiscale (MMS) mission providing the most detailed observations of the electron diffusion region to date [9], dedicated to the study of the Sun, the solar wind, and the magnetosphere, thus making our very own solar system the best natural laboratory for the study of magnetic reconnection.

Magnetic reconnection is not limited to space plasmas but also occurs in terrestrial plasmas. It allows for non-ideal instabilities to develop in tokamak devices, leading to the loss of peaked temperature profiles across flux surfaces in what's known as a sawtooth crash [10, 11]. Additionally, there have been a plethora of experiments dedicated to reconnection throughout the years, four of which are illustrated in Fig. 1.2. Experiments like these continue to be significant contributors in confirming spacecraft observations and theoretical studies, benchmarking simulations, and to the discovery of new phenomena [12, 13, 14]. The subject of magnetic reconnection is filled with a richness that many before have dedicated their study to and many after will choose to do the same. While there has been extensive research to date, much is still left to discover and it is through this lens that motivation for the following dissertation is derived.

The remainder of this chapter will introduce ideas important to the work presented beginning with the basic theory of magnetic reconnection in Section 1.2. Section 1.3 contains a description of kinetic effects during collisionless reconnection, and section 1.4 details the proposed experiment motivated by this discussion. Finally, the goals for this thesis and an outline of the remaining chapters are presented in Section 1.5.

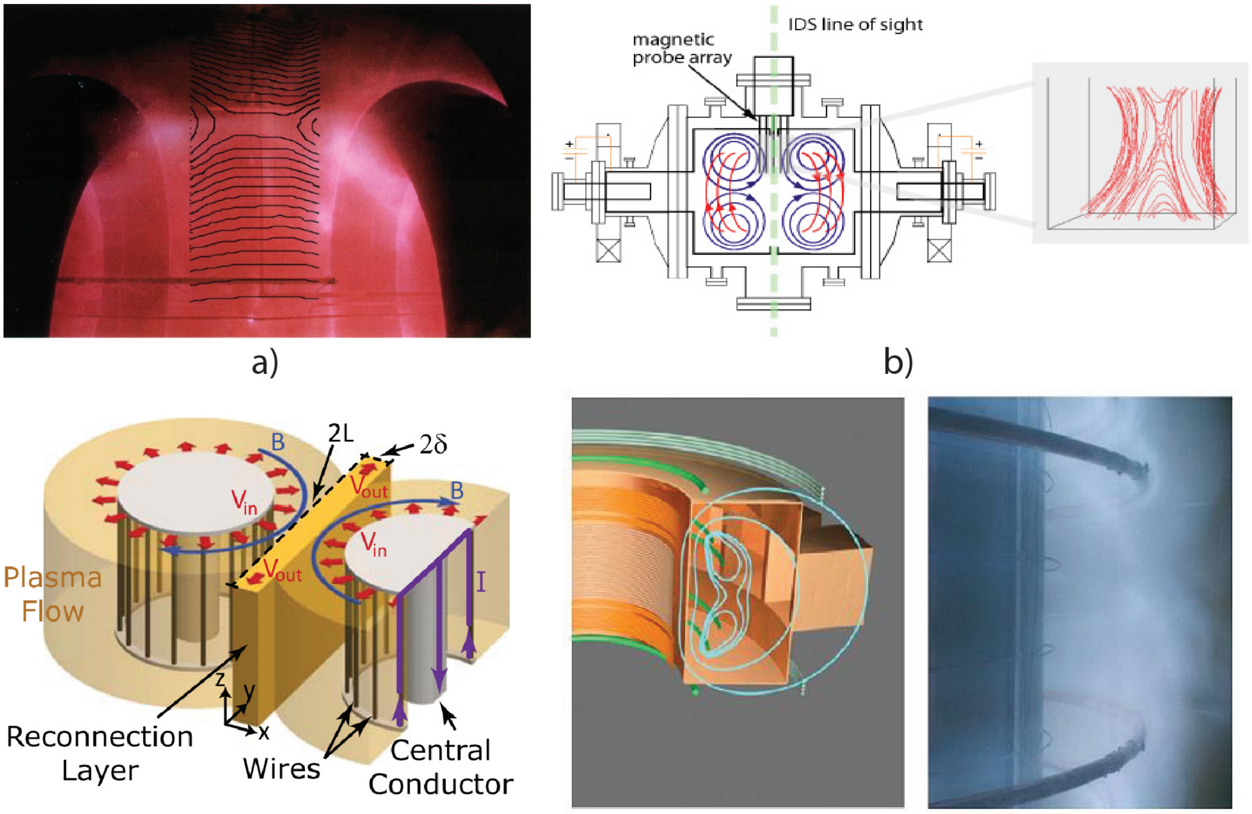

a) b)

c) d)

Figure 1.2: (a) Visible light image of the MRX experiment at Princeton Plasma Physics Laboratory during a discharge. The poloidal magnetic field lines are overlaid, indicating the reconnection X-line (from Ref. [15]). (b) SSX studied reconnection by colliding two spheromaks inside its chamber (left). A simulation of the magnetic field (right) demonstrates what the reconnection region might look like during operation (from Ref. [16]). (c) A schematic cartoon of a pulsed power experiment in which vaporized material is driven together to form a reconnection layer (from Ref. [17]). (d) The Versatile Toroidal Facility specialized in strong guide field reconnection. A visible light image (right) shows a discharge with strong emission closely following the theoretical field lines shown in the schametic cross section (left) (from psfc.mit.edu).

1.2 The Basics of Magnetic Reconnection

1.2.1 Alfvén's Theorem

Ohm's law, in the single fluid approximation of resistive magnetohydrodynamics (MHD), states that the current $\mathbf{J}$ is proportional to the electric field $\mathbf{E}'$ in the frame moving at velocity $\mathbf{v}$ with the plasma

$$\mathbf{E}' = \mathbf{E} + \mathbf{v} \times \mathbf{B} = \eta \mathbf{J}\,, \tag{1.1}$$

where $\eta = m_e/ne^2\tau_{ei}$ is the Spitzer resistivity and τ_{ei} is the electron-ion collision time. Combining Ohm's law with Faraday's law, Ampere's law, and the divergence constraint

$$\boldsymbol{\nabla} \times \mathbf{E} = -\frac{\partial \mathbf{B}}{\partial t} \tag{1.2}$$

$$\boldsymbol{\nabla} \times \mathbf{B} = \mu_0 \mathbf{J} \tag{1.3}$$

$$\boldsymbol{\nabla} \cdot \mathbf{B} = 0\,, \tag{1.4}$$

we get the familiar magnetic induction equation

$$\frac{\partial \mathbf{B}}{\partial t} = \boldsymbol{\nabla} \times (\mathbf{v} \times \mathbf{B}) + \frac{\eta}{\mu_0}\nabla^2 \mathbf{B}\,, \tag{1.5}$$

where the resistivity is assumed to be uniform. Thus, the time evolution of the magnetic field can be described by two parts, an advection term and a diffusion term. Assuming L is the typical length scale of the system and the Alfvén velocity $v_A = B/\sqrt{\mu_0 n m_i}$ as the characteristic MHD speed, then taking a ratio of these two terms provides a dimensionless ordering of their relative strengths known as the Lundquist number

$$S = \frac{\mu_0 L v_A}{\eta}\,. \tag{1.6}$$

For $S \ll 1$, Eq. 1.5 reduces to a pure diffusion equation with a resistive timescale $\tau_{\mathrm{R}} = \mu_0 L^2/\eta$. For $S \gg 1$, the advection term dominates and the plasma flow controls field transport. The characteristic timescale in this limit is the Alfvén time $\tau_{\mathrm{A}} = L/v_A$.

This latter limit is often sufficient to describe the macroscopic behavior of a plasma since S is typically very large for most space plasmas [18]. As an example, coronal structures can have a range of parameters of $L \sim 10^6$–10^8 m, $B \sim 10^{-2}$–10^{-4} T, $n \sim 10^{14}$–10^{16} m^{-3}, $T \sim 10^6$ K

($\sim$ 100 eV), $v_A \sim 10^4$–10^6 m/s, and $\eta/\mu_0 \sim 1$ m^2/s, resulting in Lundquist numbers of $S \sim 10^{10}$–10^{14}. Similarly, the solar wind and magnetosphere may have $S \sim 10^{12}$ while solar flares have $S \sim 10^8$, all of which are much greater than unity [19, 1]. With such high S, the diffusion term in Eq. 1.5 becomes negligible, and plugging back in to Faraday's law reduces to

$$\mathbf{E} + \mathbf{v} \times \mathbf{B} = 0\,, \tag{1.7}$$

also known as the ideal MHD limit for a perfectly conducting fluid. In such a limit, the magnetic field is said to be frozen into the plasma. It is easy to see this by considering the magnetic flux Ψ through some closed surface that moves with a plasma

$$\Psi = \int_{\mathbf{S}} \mathbf{B} \cdot d\mathbf{S}\,. \tag{1.8}$$

Taking the time derivative requires considering the variation in both $\mathbf{B}$ and the changing area such that

$$\frac{d\Psi}{dt} = \int_{\mathbf{S}} \frac{\partial \mathbf{B}}{\partial t} \cdot d\mathbf{S} + \oint \mathbf{B} \cdot (\mathbf{v} \times d\mathbf{r})\,. \tag{1.9}$$

Using Faraday's law in the first term and Stokes' theorem for the second results in

$$\frac{d\Psi}{dt} = -\int_{\mathbf{S}} \boldsymbol{\nabla} \times (\mathbf{E} + \mathbf{v} \times \mathbf{B}) \cdot d\mathbf{S} = 0\,, \tag{1.10}$$

where Eq. 1.7 is used in the final equality. This indicates that the magnetic flux through any arbitrary loop of plasma remains constant and that the magnetic field lines move with the plasma, and vise versa, also known as Alfvén's theorem or the frozen flux theorem. Flux freezing then implies that there can be no topological change in the magnetic field, i.e., any plasma associated with one field line is not allowed to move to another and that the field lines cannot break apart and reconnect. Even with finite η, using the case of the solar corona from earlier, from diffusion alone the macroscopic resistive time is $\tau_{\mathrm{R}} \sim 10^{12}$–$10^{16}$ s, or more than 30000 years! This is astronomically large, and to account for the observed solar dynamics timescales, further consideration is required.

1.2.2 Sweet-Parker Reconnection

In the case of a perfectly conducting plasma, if two distinct regions of opposing magnetic field flow together then ideal MHD prohibits any inductive electric field at the resulting null point. The plasma will generate a current sheet, characterized by large magnetic field gradients, in order to counteract any topology change and not allow any dissipation, simply storing the original magnetic energy. If instead of a perfectly conducting plasma, we allow for some small but finite η, then diffusion may become significant due to the Laplacian in the second term of Eq. 1.5. It is this dissipation in thin current sheets that underpins magnetic reconnection theory and provides the mechanism possible in order to help explain the observed rates of reconnection.

The concept of magnetic fields breaking apart and recombining in thin current sheets was first suggested by R. Giovanelli (Ref. [20]) with the term "reconnection" being coined by J. Dungey in Ref. [2]. However, it was P. Sweet (Ref. [3]) and E.N. Parker (Ref. [4]) who used MHD to provide the first formal theory for magnetic reconnection now known as Sweet-Parker reconnection (SP reconnection). The rest of this section outlines the important qualities of this theory.

We first start with the steady state and 2-dimensional system sketched in Fig. 1.3. Two regions of anti-parallel magnetic field with strength B flow at v_{in} into a thin current sheet (also called a diffusion region) of length $2L$ and width 2δ. From the inflow region, the magnetic field diffuses with some finite η into the current layer and flows out into the outflow region, or exhaust, at v_{out}.

A uniform out-of-the-page electric field E will exist in order to balance inductive field line motion outside the layer with diffusion inside. The ideal Ohm's law (Eq. 1.7) can be used for the inflow while the resistive Ohm's law (Eq. 1.1) applies in the layer with $B = 0$ such that

$$E = v_{\text{in}} B = \frac{\eta B}{\mu_0 \delta} \tag{1.11}$$

where Ampere's law, $J = B/(\mu_0 \delta)$, was used in the last equality. Thus, the inflow velocity is

$$v_{\text{in}} = \frac{\eta}{\mu_0 \delta}\,. \tag{1.12}$$

Assuming incompressibility and particle continuity, the rate of particles into and out of the layer is equal such that

$$v_{\text{in}} L = v_{\text{out}} \delta\,. \tag{1.13}$$

Following from the conversion of magnetic energy in the inflow into kinetic energy in the exhaust, the pressure along the layer is approximately

$$\frac{B^2}{2\mu_0} = \frac{1}{2} n m_i v_{\text{out}}^2 \,. \tag{1.14}$$

Thus, the maximum possible outflow speed is simply the Alfvén speed calculated from the upstream magnetic field

$$v_{\text{out}} = \frac{B}{\sqrt{\mu_0 n m_i}} = v_A \,. \tag{1.15}$$

Finally, combining Eqs. 1.12, 1.13, and 1.15, the ratio of the inflow to the outflow speed, which is commonly referred to as the reconnection rate, is then

$$\frac{v_{\text{in}}}{v_{\text{out}}} = \frac{\delta}{L} = \left(\frac{\eta}{\mu_0 L v_A}\right)^{1/2} = S^{-1/2} \,. \tag{1.16}$$

The timescale for SP reconnection can be estimated as $\tau_{\text{SP}} = L/v_{\text{in}} = S^{1/2}\tau_{\text{A}} = (\tau_{\text{R}}\tau_{\text{A}})^{1/2}$, such that it is significantly faster than resistive diffusion across the plasma system alone, but because of its dependence on S, SP reconnection is still relatively slow due to the large aspect ratio of the

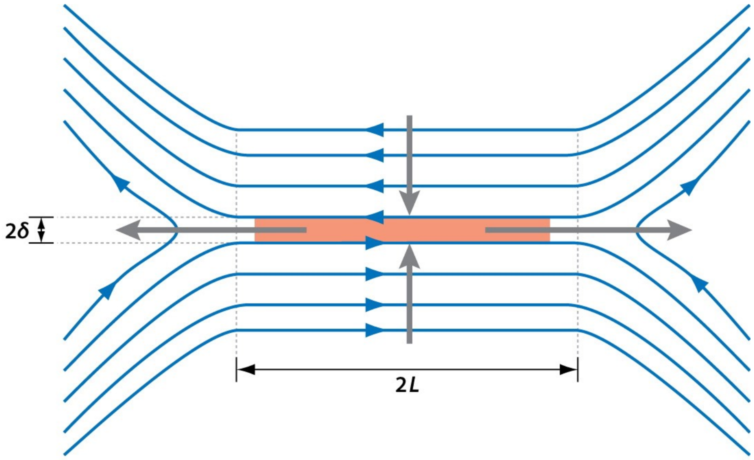

Figure 1.3: A drawing of the magnetic field geometry during Sweet-Parker reconnection. The magnetic field flows into a thin region of current with finite resistivity η. The blue lines are the magnetic field and the grey arrows show the direction of flow into and out of the diffusion region. The figure is taken from Ref. [21].

SP current layer. The diffusion region must be very thin in order to support the necessary current, but this width becomes the bottleneck in allowing the total flux to pass into the exhaust. Due to this limitation, SP reconnection is inappropriate for describing most astrophysical reconnection phenomena. For example, when using the appropriate parameters in the solar corona provided earlier, $\tau_{\text{SP}} \gtrsim 10^7$ s, or a few months, compared to the observed timescales of minutes to hours. However, while not suitable to describe all reconnection, SP reconnection has still been shown to be applicable numerically [22] and experimentally [23] under the appropriate conditions [24], and introduces many of the common features of reconnection theory.

1.2.3 Two Fluid Reconnection

The approximations used in MHD theory imply there is no inherent plasma length scales and that the gradient length scales are much larger than the plasma inertial lengths/skin depths and Larmour radii. In physical systems, however, the width of the current sheet that is predicted by SP reconnection can drop below these fundamental length scales where the ion and electron velocities are quite different and no longer satisfy the conditions for MHD. To account for this, it is appropriate to use a "two fluid" description where the electrons and ions are treated as separate fluids. The reconnection dynamics are then characterized by the generalized Ohm's law instead of the resistive Ohm's law (Eq. 1.1).

Taking the electron momentum balance equation and recasting with the appropriate fluid parameters, the generalized Ohm's law can be written as

$$\mathbf{E} + \mathbf{v} \times \mathbf{B} = \eta \mathbf{J} + \frac{\mathbf{J} \times \mathbf{B}}{ne} - \frac{\boldsymbol{\nabla} \cdot \mathbf{P_e}}{ne} + \frac{m_e}{ne^2}\frac{d\mathbf{J}}{dt}\,, \tag{1.17}$$

where $\mathbf{P_e}$ is the full electron pressure tensor. The new terms on the RHS are known as the Hall, electron pressure, and electron inertia terms, respectively. A new length scale appears when comparing the Hall term with the inductive term. This ratio can be approximated as

$$\frac{|\mathbf{J} \times \mathbf{B}/ne|}{|\mathbf{v} \times \mathbf{B}|} \cong \frac{B^2/\mu_0 \delta ne}{v_A B} = \frac{1}{\delta}\left(\frac{m_i}{\mu_0 ne^2}\right)^{1/2} = \frac{d_i}{\delta}\,, \tag{1.18}$$

where again δ is the width of the current layer and $d_i = c/\omega_{pi}$ is the ion inertial length. When $\delta \lesssim d_i$, the ions decouple from the magnetic field and the Hall term dominates in Eq. 1.17.

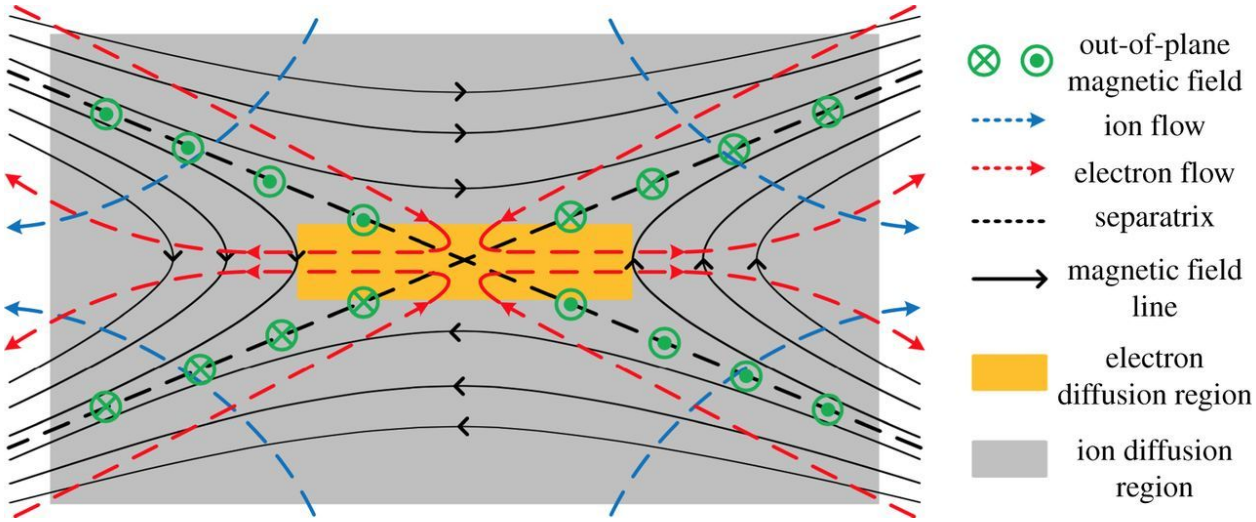

Figure 1.4: Two anti-parallel fields enter the ion diffusion where ions decouple from the magnetic field and the electrons continue flowing with the field until they reach the electron diffusion region. The difference in the ion and electron flow creates a quadrupolar magnetic field out-of-the-page known as the Hall field. Reproduced from [27].

A picture of this process is shown in Fig. 1.4 where the ions become unmagnetized in the ion diffusion region (grey area) while the electrons remain frozen into the field until they enter the electron diffusion region (orange) before both ions and electrons become re-magnetized in the exhaust. The difference between the ion and electron flows is what's known as the Hall currents and is the cause of a quadrupolar magnetic field structure perpendicular to the reconnecting plane known as the Hall field. The electron pressure and inertia terms become strong in the electron diffusion region which occurs at length scales approaching the electron inertial length $d_e = c/\omega_{pe}$ [25, 26].

These effects lead to a reconnection rate that is much faster than SP reconnection and is commonly referred to as fast reconnection. The opening angle of the exhaust must increase (decreased aspect ratio of the current layer length to width) in order to allow more flux through the region and accommodate the large Hall electric field. This removes the bottleneck found in SP reconnection and results in a rate independent of S where $v_{\text{in}}/v_{\text{out}} \sim 0.1$ and more accurately describes observed reconnection timescales. It has been shown that this reconnection rate is largely independent of the exact mechanism beyond classical resistivity that breaks the frozen in condition [28]. Here, it should be noted that the Hall term does not actually break the frozen in condition as $\mathbf{v} - \mathbf{J}/ne = \mathbf{v_e}$, and therefore the magnetic field is simply tied with the electron fluid such that $d\Psi\,/\,dt = -\int \boldsymbol{\nabla} \times (\mathbf{E} + \mathbf{v_e} \times \mathbf{B}) \cdot d\mathbf{S} = 0$.

There are then two key signatures of fast reconnection: (1) the quadrupolar Hall magnetic field and (2) the nearly ubiquitous fast reconnection rate. This regime has now been studied extensively numerically [29, 30]. The first measurements of the Hall fields and two fluid effects came from MRX [31] and shortly thereafter from SSX [16]. Additionally, the Hall fields were measured in spacecraft observations in Earth's magnetotail [32]. Details of fast reconnection in the magnetosheath were later expanded on with evidence of distinct ion and electron diffusion regions as well as with measurements of the reconnection rate [33]. While the theory and application of fast reconnection has been incredibly successful, there still remain major questions. One of the most significant open questions is why there seems to be a universal rate of ~ 0.1. While many have provided insight into this question [34], it remains a topic of ongoing research.

Here it is important to mention that a transition to dynamics much faster than SP reconnection can also occur in the collisional regime at large Lundquist number ($S > 10^4$) [35]. This regime is characterized by long resistive current layers that break up into magnetic islands, or plasmoids, separating multiple, smaller reconnecting current sheets and allow for more efficient transfer of magnetic flux from the inflow [36]. The new current sheets remain susceptible to plasmoid development until the local Lundquist number drops below the critical value or the current layer width approaches the ion kinetic scale. More details on plasmoids and this regime are discussed in Chapter 4.

1.3 Kinetic Regime of Magnetic Reconnection

The fast reconnection described in the previous section is applicable any time $S \gg 1$, or when $\eta J/v_A B \ll 1$, and for this reason is often referred to as collisionless reconnection. This follows because the electron-ion collision time obeys $\tau_{ei} \propto T_e^{3/2}/(n\ln(n))$ such that the resistivity is strongly dependent on temperature and only weakly dependent on density, $\eta \propto \ln(n) T_e^{-3/2}$. Many basic plasma, laboratory experiments have low η but because of their relatively high density, the characteristic collision time are often much shorter than most dynamic timescales of interest. Under these conditions, Coulomb collisions can be frequent enough that the electron distribution function remains near-Maxwellian. In contrast, τ_{ei} can be much longer than typical timescales of interest in space plasmas, like the interplanetary solar wind and magnetospheric plasma. For example, the mean free path of electron-ion collisions in the solar wind is comparable to the distance between the Sun and the Earth (~ 1 AU), and collisions are sufficiently infrequent that kinetic effects in the electron dynamics are retained and electron distributions do not relax to near-Maxwellian form. Strongly anisotropic electron distributions have been observed during reconnection in Earth's magnetosphere by the Wind and Cluster spacecraft missions [37, 38] in which the pressure component parallel to the local magnetic field is larger than the perpendicular component, $p_{e\parallel} > p_{e\perp}$. This represents a more strict condition on the collisionality which defines the "kinetic" regime inside the collisionless reconnection regime in which kinetic effects such as pressure anisotropy develop, strongly impacting the reconnection process in ways not accounted for in traditional two fluid reconnection.

The kinetic process that leads to pressure anisotropy in the appropriate conditions has been well described by a theoretical model [39, 40] and has been extensively studied through particle-in-cell (PIC) and fluid simulations [41, 42, 43, 44]. In essence, the parallel energization of inflowing electrons occurs through adiabatic trapping as the magnetic field decreases near the X-line and a parallel potential, $\Phi_\parallel = \int E_\parallel dl$, develops to regulate the electron density in order to maintain quasineutrality in this region, leading to an elongated pressure distribution. This pressure anisotropy, $p_{e\parallel}/p_{e\perp} > 1$, then drives large scale current layers and electron jets and fundamentally alters the partition between ion and electron heating [45]. With little to no guide magnetic field $B_g \sim 0$ (antiparallel reconnection), the pressure anisotropy that develops in the inflow pitch angle mixes as $B \to 0$ leading to isotropization in the reconnection exhaust. However, with a sufficiently large guide field, the electrons remain trapped throughout the diffusion region and the

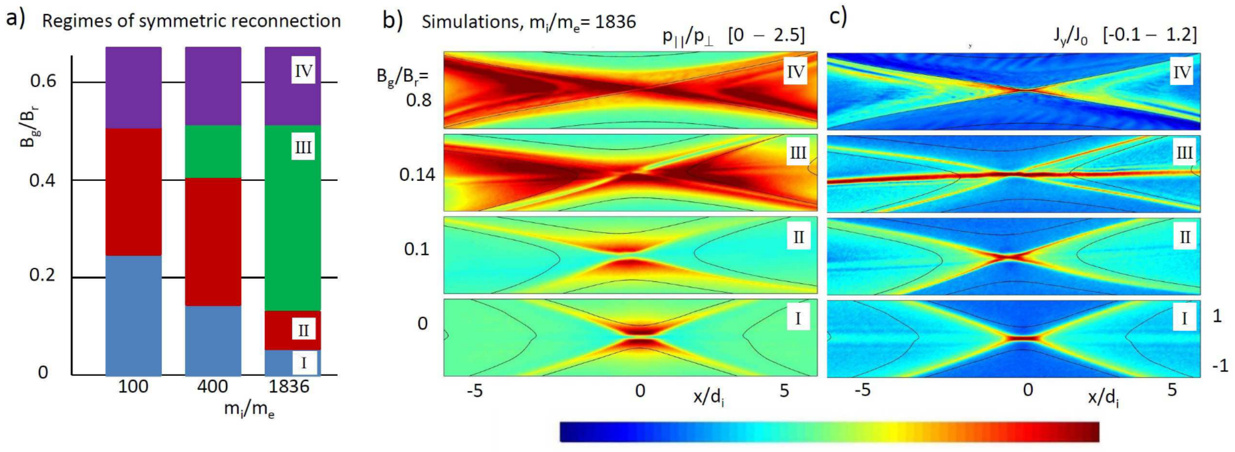

Figure 1.5: (a) Regimes of reconnection as a function of B_g/B_{rec} for three cases of m_i/m_e. Each regime has unique characteristics in the profiles of the pressure anisotropy (b) and current density (c). Figure adapted from Ref. [44].

pressure anisotropy persists into the exhaust, supporting long, embedded current layers extending 10s of d_i from the X-line.

Figure 1.5 summarizes the findings of Ref. [44] where it is shown how the structure of the reconnection region can be divided into four distinct regimes characterized by the strength of the guide field. Obtained from PIC simulations at a realistic mass ratio of $m_i/m_e = 1836$ and varying B_g, Figs. 1.5(b,c) show the pressure anisotropy and out-of-plane current in each regime. Regime 1 represents the antiparallel case discussed above with pressure anisotropy developing in the inflow region. As B_g increases to moderate levels (0.12–0.5 of the reconnection field), a recently discovered Regime 3 arises in which the magnetic moments of the bulk electrons are conserved and no pitch angle mixing occurs in the exhaust, giving rise to the extended (simulation size) current layers supported by the pressure anisotropy. As the guide field increases further, the pressure anisotropy develops but is not strong enough to reach the marginal firehose condition,

$$p_{e\parallel} - p_{e\perp} \lesssim \frac{B^2}{\mu_0}\,, \tag{1.19}$$

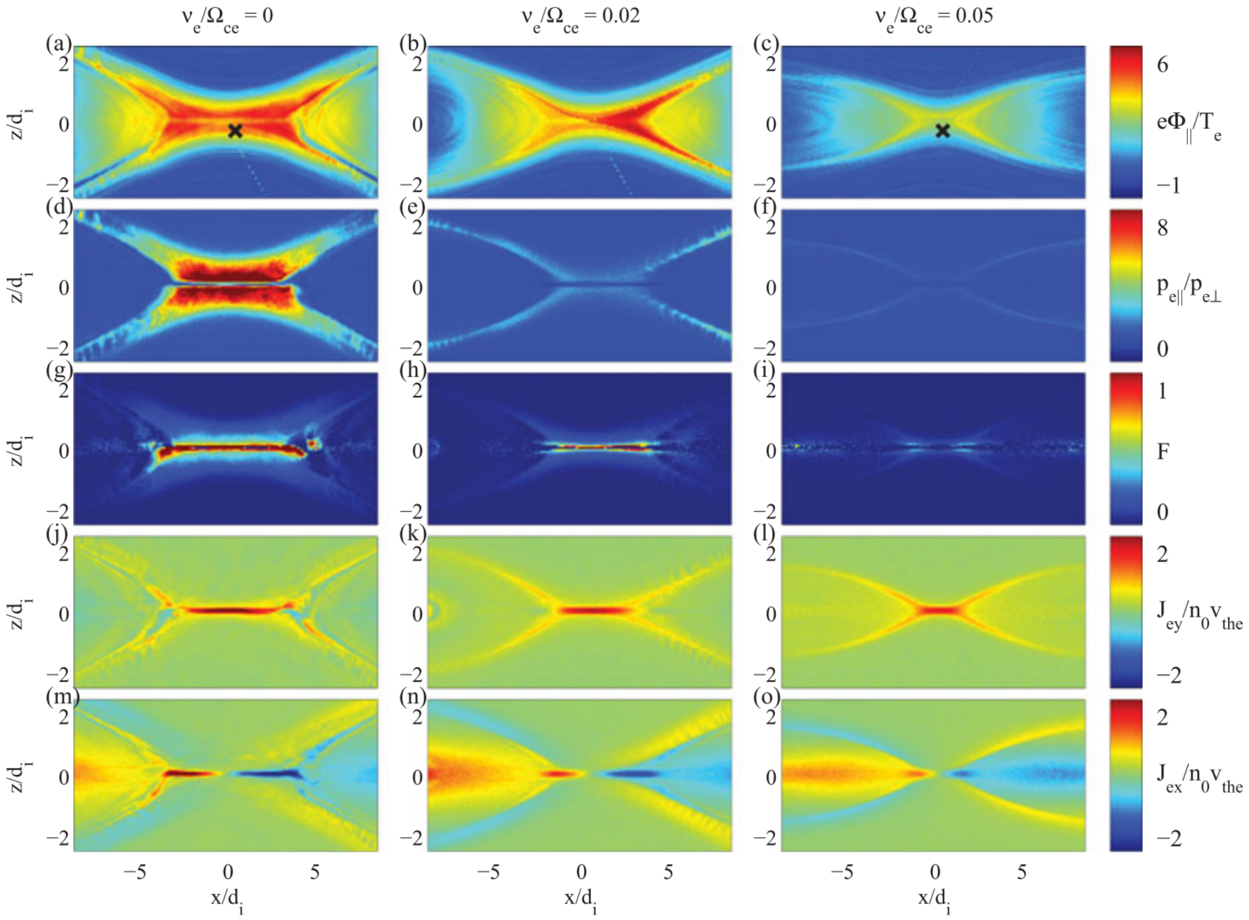

Figure 1.6: (a-c) The trapping potential, (d-f) electron pressure anisotropy, (g-i) firehose condition, (j-l) out-of-plane current density, and (m-o) in-plane current density for three different cases of collisionality. Figure taken from Ref. [46].

required for the long current layers. Additionally, it has also been shown that the level of pressure anisotropy, $p_{e\|}/p_{e\perp}$, is most pronounced at low electron beta,

$$\beta_e = \frac{2\mu_0 p_e}{B^2} \leq 0.02\,. \tag{1.20}$$

A comprehensive study of the collisional effects on so called collisionless reconnection, presented in Ref. [46], shows that pressure anisotropy is highly sensitive to collisions. Adapted from this study, Fig. 1.6 presents results from a series of 2D PIC simulations for antiparallel reconnection at a realistic mass ratio of $m_i/m_e = 1836$. The three cases represent different initial electron collision frequencies of $\nu_e = 0, 0.02$ and $0.05\Omega_{ce}$, where $\Omega_{ce} = eB/m_e$ is the electron cyclotron frequency, in which collisions are negligible for force balance ($\eta J_y/E_y \ll 1$) but present distinctly different reconnection profiles dependent on the level of pressure anisotropy. Considering the fully collisionless case where $\nu_e = 0$, a strong trapping potential and subsequent pressure anisotropy develops in the inflow regions, supporting the extended current layer and electron jets seen in Figs. 1.6(j,m). As ν_e increases, the trapping potential remains, but the scattering from collisions reduces the total pressure anisotropy relative to the fully collisionless case. As $\nu_e/\Omega_{ce} = 0.05$, the pressure anisotropy is almost entirely eliminated and the strong electron jets and elongated current layer are reduced to levels associated with typical two fluid reconnection.

A critical result provided in Ref. [46] is that for the collisionality to be considered sufficiently weak for these kinetic effects to appear then the collision time $1/\nu_e$ must be longer than the typical convection time τ_c of the plasma through the diffusion region. As discussed in Section 1.2.3, the typical inflow speed upstream of the X-line ($\sim 1d_i$ away) is $\sim 0.1v_A$ such that the convective time is $\tau_c \sim d_i/(0.1v_A)$. Provided the following definitions,

$$\begin{aligned} v_A &= \frac{B}{\sqrt{\mu_0 n m_i}} \quad \text{and} \\ d_i &= \sqrt{\frac{m_i}{\mu_0 n e^2}}\,, \end{aligned} \tag{1.21}$$

then the above condition on the collisionality can be written as

$$\nu_e \lesssim \frac{1}{\tau_c} \lesssim \frac{0.1v_A}{d_i} = 0.1\frac{m_e}{m_i}\Omega_{ce}\,. \tag{1.22}$$

Using Eqs. 1.21 in Eq. 1.6 for the Lundquist number, the above condition on the collisionality can be expressed as

$$S = \frac{L}{d_i}\frac{\Omega_{ce}}{\nu_e} \gtrsim 10\frac{m_i}{m_e}\frac{L}{d_i}\,. \tag{1.23}$$

These limits can then be used to define the kinetic regime of collisionless reconnection, delineating from other fast reconnection in which collisions can alter the electron dynamics and eliminate the magnetic structures and currents driven by pressure anisotropy.

1.4 Experimental Facility for the Study of Collisionless Reconnection

As a valuable tool to summarize the discussion in this chapter on magnetic reconnection, the reconnection phase-space diagram developed by Daughton and Roytershteyn [47, 48] is presented in Fig. 1.7. This diagram represents the various regimes for antiparallel reconnection (no guide field) as a function of the Lundquist number, $S = \mu_0 \epsilon L v_A / \eta$, and the relative system size, $\lambda = L/d_i$, where L is the full system size and $\epsilon < 1$ is a factor relating L to the length of the reconnection current layer. As discussed in Section 1.2.3, the transition from collisional to collisionless reconnection occurs when the current layer width approaches the ion kinetic scale, or using Eq. 1.16, when $S = \epsilon^2 \lambda^2$. The condition in Eq. 1.23 adds the kinetic regime, the purple area, to the collisionless reconnection region. Also seen in this diagram are transitions into multiple X-line, or plasmoid, regimes for both collisional and collisionless reconnection and are discussed in more detail in Chapter 4.

Laboratory experiments are essential in the discovery of new physics and the validation of research in plasma theory, simulation, and observation but often lag behind the main progress in these other areas. This is especially true for the kinetic regime of magnetic reconnection and the model for pressure anisotropy which has been verified numerically as well as through spacecraft observation. For experiments to remain relevant in this maturing field of research and help push forward these new frontiers in basic plasma physics, new devices are needed which access the regime of pressure anisotropy and large system size. Thus, a new experimental facility was proposed in order to study this new regime called the Terrestrial Reconnection Experiment (TREX).

The conditions provided in Section 1.3 offer meaningful guidelines for such an experiment to approach the kinetic regime. As such, the optimal experimental parameters depend on many factors and must largely be balanced between each other and other physical limitations. For example, a large relative system size requires high n and large L, low collisionality to allow for $p_{e\|}/p_{e\perp} > 1$ requires low n and high T_e and B, while low electron pressure requires low n and T_e but high B. Additionally, the achievable Lundquist number S for reconnection is dependent on the upstream magnetic field B_{rec} which is related to the applied loop voltage by the allowed reconnection rate

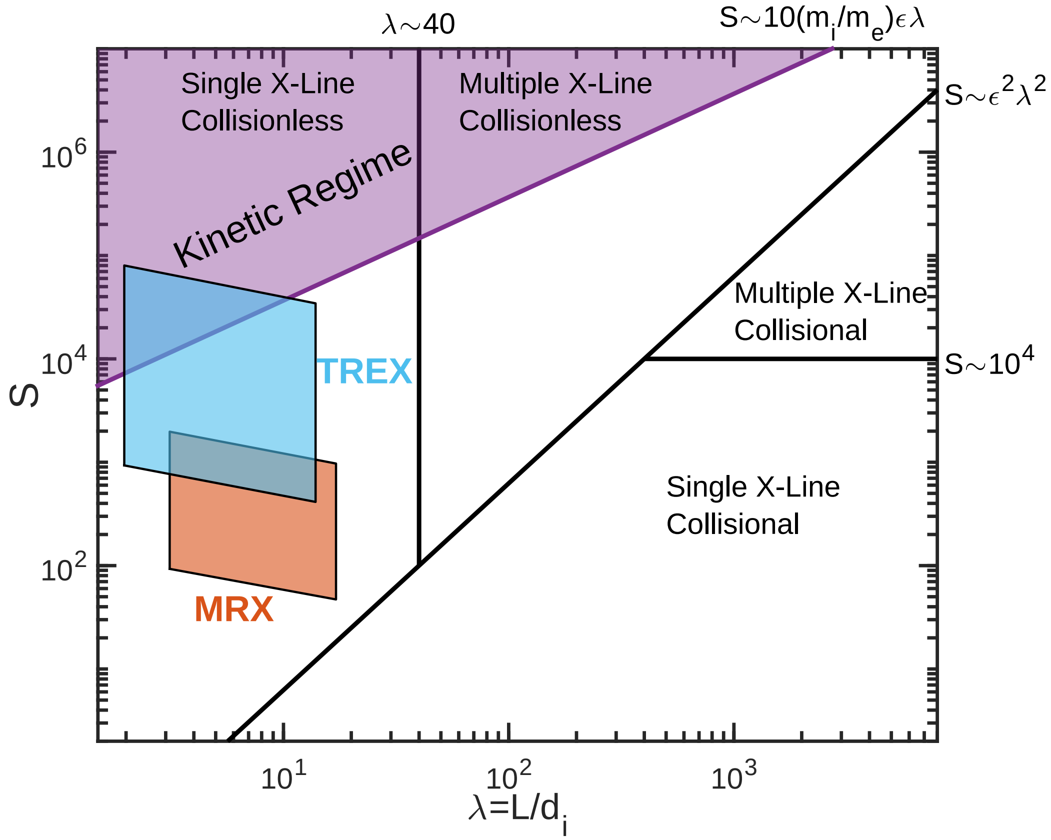

Figure 1.7: Operating regime of TREX for antiparallel reconnection. TREX is specially designed to access the kinetic regime where previous reconnection experiments are unable to operate.

of the system, i.e., $V_{\text{loop}} = 2\pi R E_{\text{rec}}$, where $E_{\text{rec}} \simeq 0.1 v_A B_{\text{rec}}$. This last point is discussed in more detail in Chapter 6. With these considerations, there exists an accessible experimental operating window for the study of the kinetic regime. These parameters are provided in Table 1.1 along with the achieved parameters for two other reconnection devices. Placing these limits into the diagram in Fig. 1.7 shows the ability of TREX to operate well into the kinetic regime where previous experiments cannot reach. It should be noted that with the addition of a guide field, TREX is also suited to the study of embedded current layers driven by pressure anisotropy as well as the transition into plasmoid dominated reconnection that occurs at much larger system size. However, all work performed for this dissertation focuses on the case of antiparallel reconnection, and therefore the discussion of guide field reconnection here is limited.

	$n_e/(\mathrm{m}^{-3})$	$T_e/(\mathrm{eV})$	$B_{\text{rec}}/(\mathrm{T})$	$B_g/(B_{\text{rec}})$	$L/(\mathrm{m})$
TREX	$10^{17} - 10^{19}$	$5 - 30$	$0 - 0.02$	$0 - 2$	$0.8 - 2$
MRX	$10^{19} - 10^{20}$	$5 - 10$	$0.005 - 0.03$	$0 - 3$	0.7
VTF	$10^{17} - 10^{18}$	$8 - 30$	0.01	10	0.3

Table 1.1: Key parameters for various reconnection experiments.

1.5 Thesis Outline

The primary motivating factor in the creation of the TREX facility has been to reach the regime where electron pressure anisotropy alters the dynamics of magnetic reconnection and to study this in the laboratory. As such, a major element of this dissertation has been the design and construction of device hardware in efforts to achieve this end goal. Along the way, multiple iterations of the TREX hardware have been implemented and used for the study of low collisionality reconnection. While this thesis has a large focus on hardware, two independent experimental studies are reported, extending the understanding of driven magnetic reconnection. The following is a brief outline for the remainder of this thesis.

Chapter 2 provides an overview of the facility that TREX operates at and the important components comprising the facility. Chapter 3 then discusses the specific hardware encompassing the first TREX implementation. Early experiments in this configuration proved operation at unprecedented parameters while also observing the spontaneous formation of plasmoids at scales below the ion kinetic scale, a regime where plasmoids are not expected. This study is presented in Chapter 4. Following this work, TREX underwent a major overhaul of the experimental hardware, and Chapter 5 focuses on these upgrades to the facility using the prior configuration as a foundation. A comprehensive study of the effect of the drive system was then performed in order to better understand the operation of the TREX facility. Chapter 6 then reports on these findings, showing how the interplay between shocks and magnetic pileup in the inflow works to keep the normalized rate of magnetic reconnection fixed. The thesis finishes with concluding remarks in Chapter 7.

Chapter 2

The Big Red Ball Facility

The Big Red Ball (BRB) at the University of Wisconsin-Madison was originally built as the Madison Plasma Dynamo Experiment (MPDX) to investigate flow driven MHD instabilities with astrophysically relevant parameters [49]. MPDX was first conceived to study laminar and turbulent dynamo using a ring cusp confinement scheme and a novel method for stirring plasma [50]. This stirring has been demonstrated with various high R_m boundary flows that viscously couple to the bulk, high-β plasma [51]. With the inception of the Wisconsin Plasma Physics Laboratory (WiPPL) [52], a national user facility, the versatility of the MPDX device has since been exploited as a basic plasma facility and renamed the BRB (see Fig. 2.1 for the true meaning of the name). This versatility comes from the largely unmagnetized plasma confinement which makes the BRB especially suited to study a wide range of astrophysical systems and basic plasma processes including ambipolar diffusion across field lines [53], the magneto-rotational instability, collisionless shock formation, and the Parker spiral [54].

This chapter details the experimental facility which underpins the TREX experiments on magnetic reconnection beginning with a description of the vacuum vessel and cusp confinement in Sections 2.1 and 2.2. Section 2.3 provides details of the plasma sources used for the TREX experiments followed by a general overview of probe designs and the control system in Sections 2.4 and 2.5. Finally, emphasis will be given to Section 2.6 which describes the Helmholtz coil developed during this dissertation as an essential contribution to the facility and is now used in many different experiments on the BRB. A full description of the TREX specific experimental configuration is provided in Chapters 3 and 5.

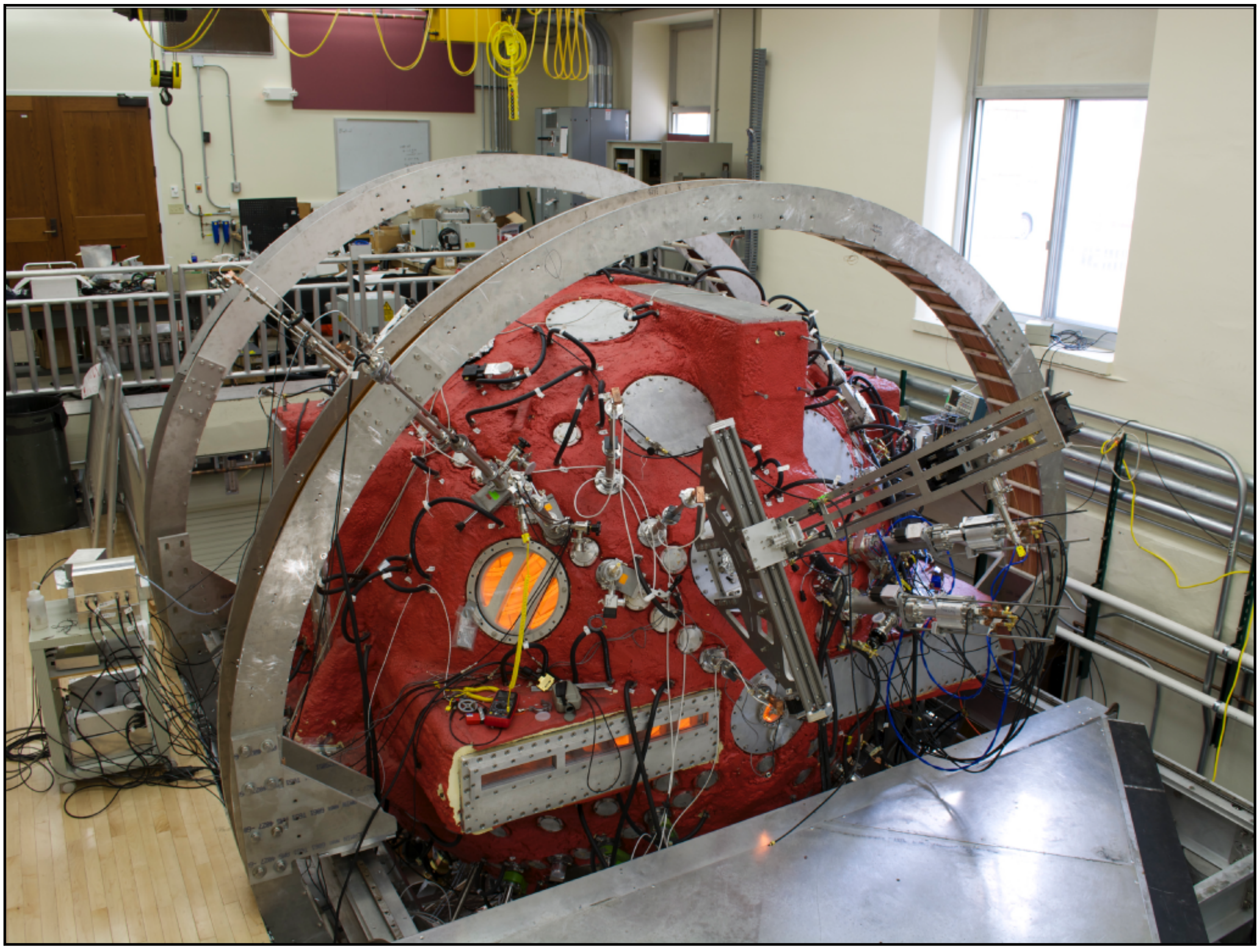

Figure 2.1: A photo of the Big Red Ball at UW-Madison. The device gets its name from the "Badger Red" painted foam covering the outside of the vessel.

2.1 Vacuum Vessel

The BRB is a spherical vacuum vessel made out of cast aluminum that is $\sim$1.5 in. thick with an inside diameter of 3 m. An insulating spray foam covers the vessel exterior mainly to mitigate condensate buildup on the cooled metal surface which would have an adverse affect on sensitive electronics around the vessel. The casting includes channels for water cooling and cutouts for a large number of diagnostic access points. This includes over one hundred eighty-four 3 in. ports and sixteen 16.5 in. flanges at numerous longitude and latitude locations. Additionally, there are twelve rectangular “box ports” oriented vertically and horizontally surrounding the vessel. The wide range of vacuum feedthrough ports, viewports, and custom machined flanges can be seen in Fig. 2.1. The device reaches high vacuum levels by maintaining a base pressure between $5–10 \times 10^{-7}$ Torr. It achieves this through the use of two 2000 L/min turbomolecular pumps, two 1000 L/min turbomolecular pumps, and two 4000 L/min cryogenic pumps.

The vessel is oriented horizontally with its magnetic N pole pointing in the direction of geographical West. The two hemispheres are split at the equator with the N hemisphere resting on heavy duty roller bearings allowing it to slide open. This grants access to the interior of the device for maintenance and for the installation of internal TREX hardware. Additionally, just above the equator, a hole was cut into the ceiling separating the main lab space with a secondary TREX lab space. A crane transfers large hardware between the two labs through a shutter. With enough staff on hand, converting to the TREX configuration—breaking vacuum, installing hardware, and pumping back down—takes as little as a single work day to complete.

2.2 Magnetic Cusp

What makes the BRB vessel unique is its magnetic cusp confinement scheme. Lining the interior surface are more than 3000 SmCo rare earth magnets (3.8 cm×2.5 cm×5.0 cm) with $B \sim 0.3$ T at the surface. These are installed in 36 axisymmetric rings separated by 5°, as shown in Fig. 2.2. Each ring alternates polarity of the magnetic field with adjacent rings, creating a high order multipole magnetic field. Each magnet is protected from the plasma by an alumina tile

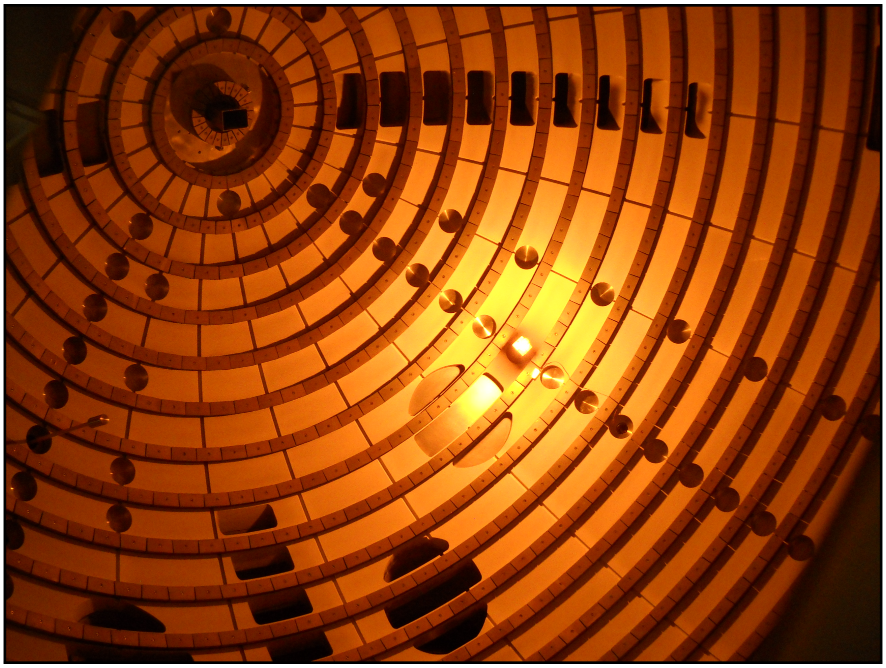

Figure 2.2: A photo of the magnet rings on the S hemisphere of the BRB. The yellow-orange glow comes from the heated LaB_6 emissive cathode.

attached to the plasma facing surface. The vessel wall between rings is also covered in an alumina spray.

Prior work has demonstrated the ability to confine steady state plasmas in the BRB. Example data is provided in Fig. 2.3 for a helium discharge. The cusp field, while very large near the magnets, drops off rapidly from the surface leaving primarily Earth's magnetic field (~ 0.45 G) for $R < 1.35$ m. The high-β plasma in the bulk is largely due to the reduction in surface losses to an area proportional to the cusp loss width of the rings.

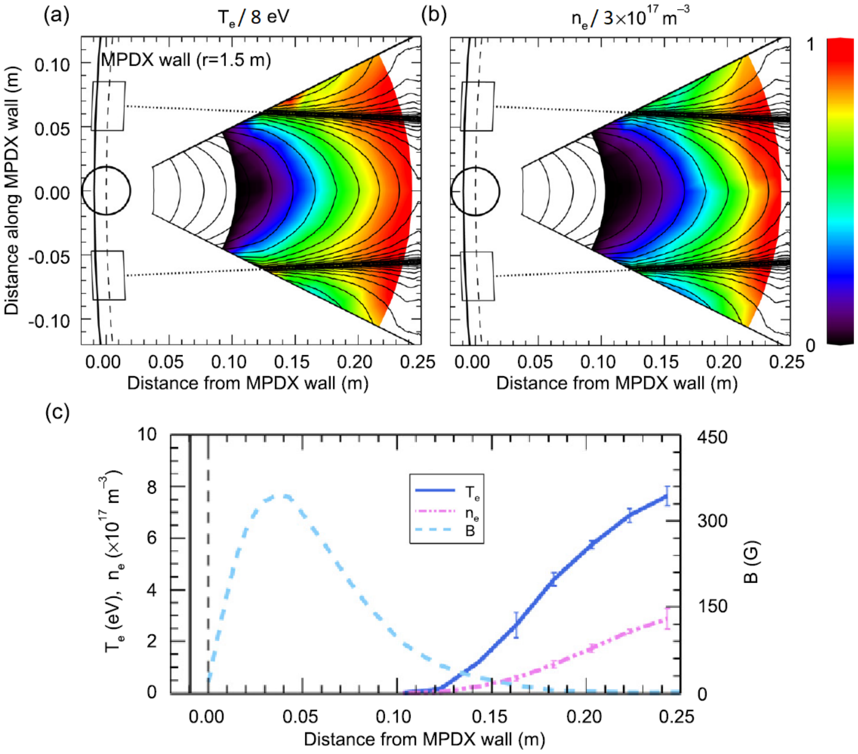

Figure 2.3: 2D measurements of (a) T_e and (b) n_e near the BRB wall. The helium plasma was generated with LaB_6 cathodes. The black lines indicate the cusp magnetic field. (c) T_e, n_e, and B along a radial cut from the profiles. Figure adapted from Ref. [49].

2.3 Plasma Sources

The following section describes only the plasma sources used for the TREX experiments presented in this thesis. The LaB_6 cathodes were used on the experiments presented in Chapter 4 whereas the plasma guns were the plasma source for the experiments presented in Chapter 6. Other plasma sources have been designed and implemented on the BRB but are not covered below.

2.3.1 LaB_6 Cathodes

The emmissive cathodes were originally designed by Dave Weisberg for heating and stirring plasma on the BRB and are covered in great detail in his thesis [55]. The cathodes utilize a lanthanum hexaboride (LaB_6) tip (3 cm$\times$7 cm cylinder) which gets radiatively heated by an internal graphite filament to $\sim$1300 °C. This assembly sits at the end of a shaft that can be inserted to a radius of $R = 1.2$ m. An electrical bias is applied with respect to a separate anode and electrons are thermionically emitted and accelerated to hundreds of eV. These electrons ionize the surrounding gas as well as heat the resulting plasma. LaB_6 is commonly used as a filament for hot cathodes in industry due to its low work function, large current output, and long lifetime.

The LaB_6 cathodes typically utilize a switching power supply to operate in steady state. However, due to difficulties when operating in the TREX configuration with a large Helmholtz field, a separate discharge circuit was implemented which is outlined in Fig. 2.4. A 72 mF bank of electrolytic capacitors charges through a simple step-up transformer and full-bridge rectifier. Once the capacitors reach a target voltage of –400 V, a comparator circuit switches off the charging circuit, leaving the bank charged until triggered through an IGCT (integrated gate-commutated thyristor). An IGCT acts similar to an SCR (silicon controlled rectifier)—in essence, a triggerable diode—except that it can be both turned on and off through its gate control. Triggering the IGCT closes the circuit and biases the LaB_6 cathode with respect to an anode across the machine to generate the plasma for a TREX shot. The IGCT allows for fine control such that after only 100 ms, before the cathode voltage decays away, the circuit is turned off and the capacitor bank is either recharged or dumped through a resistor. An RC snubber is in parallel with the IGCT to limit inductive voltage

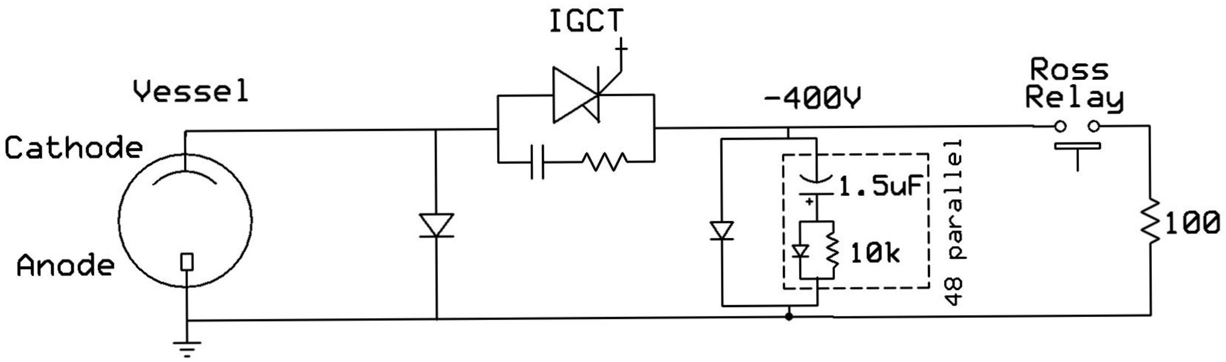

Figure 2.4: A simplified schematic diagram of the LaB_6 cathode discharge circuit used for early TREX experiments.

spikes during turn-off that could lead to catastrophic failure of the IGCT. More schematics of the full charging and discharge circuit can be found in Appendix A.

2.3.2 Plasma Guns

A hexagonal array, pictured in Fig. 2.5(a), consisting of 18 plasma washer guns, pictured in Fig. 2.5(b), was adapted for use on the BRB. These washer guns were originally designed for use on the Madison Symmetric Torus for current injection experiments [56], later implemented as the plasma source for the Rotating Wall Machine and Line-Tied Reconnection Experiments, and are the basis for local helicity injection on the Pegasus experiment [57]. The washer guns pump gas through a small inlet into an arc chamber consisting of a molybdenum cathode and anode separated by alternating molybdenum and boron nitride washers. Biasing the cathode with respect to the anode generates an arc channel along the washers, ionizing the neutral gas in the chamber. The newly generated plasma then expands out of the nozzle and into the vacuum chamber at the relative sound speed.

Each plasma gun is attached to a custom made pulse forming network (PFN) used as a power supply. After an initial voltage spike of $>$500 V which initiates ionization, each PFN maintains a constant current output ($<$5% ripple) of 1 kA and $\sim$100 V. The flange with the array of guns

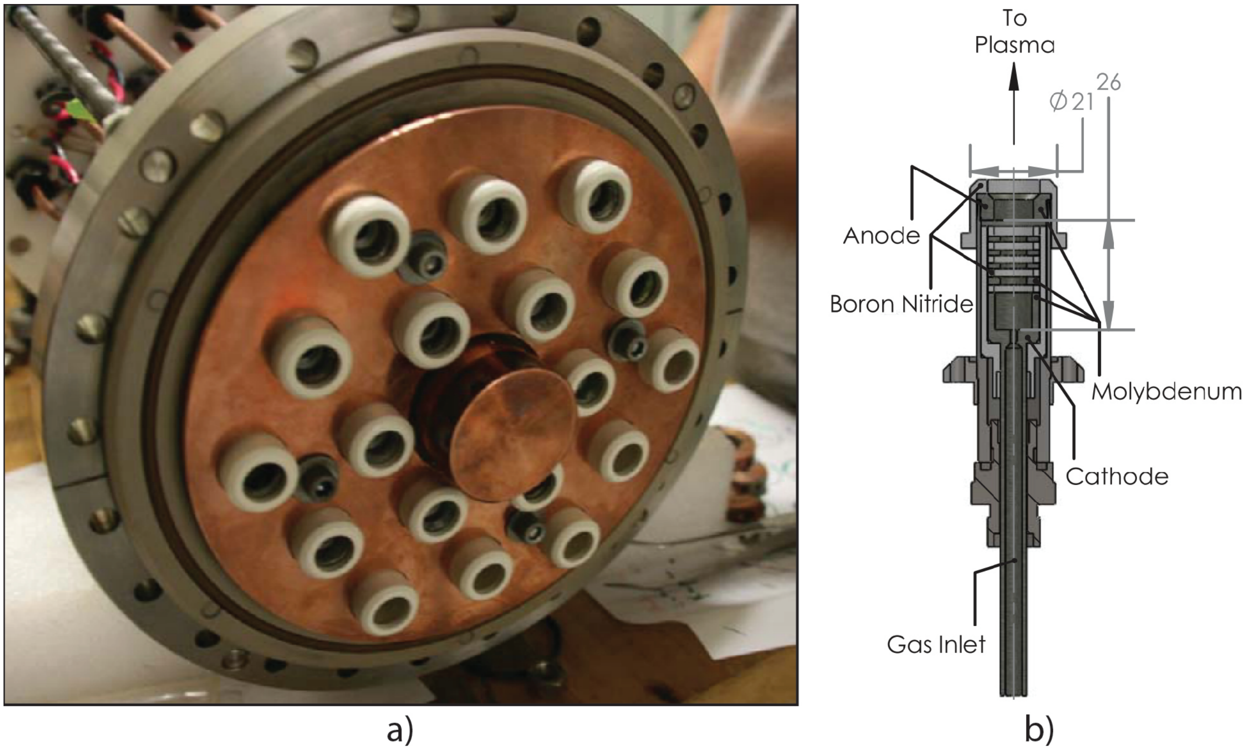

Figure 2.5: (a) A photo of the plasma gun array flange used for TREX experiments. (b) A schematic diagram of a single washer gun used in (b). Both images taken from Ref. [58].

is directly attached to the N pole of the BRB and only operated in this arc mode for the experiments presented. However, these PFNs can also be used to bias the entire plasma gun circuit with respect to an anode elsewhere in the vessel such that a current is carried by the resulting plasma channel. Matt Brookhart's thesis [58] provides a more detailed description of the plasma gun array. The plasma guns have proven to be very robust and remain the primary source for all TREX experiments at this time.

2.4 Probe Design

One of the complications of working on a physically large vessel like the BRB is the requirement of probe access throughout the plasma volume. This section details some of the considerations regarding the probe assemblies used on TREX and ways to control them.

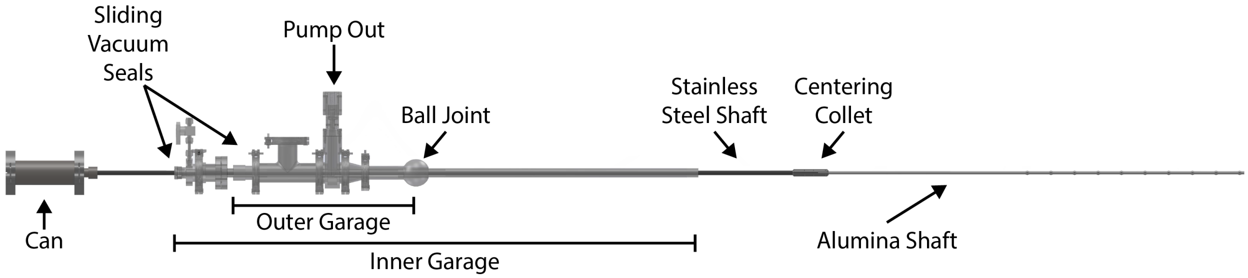

Figure 2.6: A CAD drawing of a general probe assembly used on TREX. The double telescoping design allows for deep access into the vessel.

2.4.1 Telescoping Probes

Typically, probes are installed on the vessel without breaking vacuum. This requires a probe assembly to be fully retractable inside a garage clamped to a gate valve[1]. Coupled with the requirement that probes have access to at least the center of the vessel (or beyond), a double telescoping design is necessary. A general schematic of a complete probe assembly can be seen in Fig. 2.6. The probe shaft consists of an alumina tube mated to a stainless steel shaft to protect internal probes from exposure to plasma. Electrical wiring comes out of a vacuum sealed feedthrough at the can. The probe shaft may slide inside the long internal garage which in turn slides inside an outer garage, kept concentric with centering collets around the shafts. This effectively extends the vacuum outside of the vessel when the probe is fully retracted. The entire assembly may be attached to a standard KF port or a ball and socket vacuum joint that allows for full rotation and articulation up to 30°. These probe assemblies have a tendency to become very long and range between 2–3 m in length.

2.4.2 Linear Stages

During operation, it is critical to know the precise location of probes inside the vessel. To ease this concern, motorized linear stages are often attached to a probe which allow for precise and repeatable control of probe motion. The stage clamps to the outer garage while a carriage clamps

---

[1] Most of the probes used in Chapter 6 forgo the outermost garage. This has the advantage of deeper insertion and probe access in lieu of the ability to install or remove the probe without a full vacuum break.

to the probe shaft and slides along a rail, actuated with a linear screw. The lead screw is geared to a stepper motor, controlled by a Galil motor controller, and the location is read back with an encoder. Commands are sent to the motor controller remotely from the Labview control system.

2.4.3 Sweep Stages

Functionally similar to the linear stages, the sweep stage utilizes a second angular drive transverse to a linear drive, articulating around a ball joint. Figure 2.7 shows an image of this assembly. The stage is aligned such that the probe subtends a single toroidal angle and sweeps out a poloidal plane. The angular extent of the stage is ±30° whereas the linear extent is limited by the length of the attached probe and the lead screw. As with the linear stages, precise transformation into machine coordinates and control of both motions is done remotely.

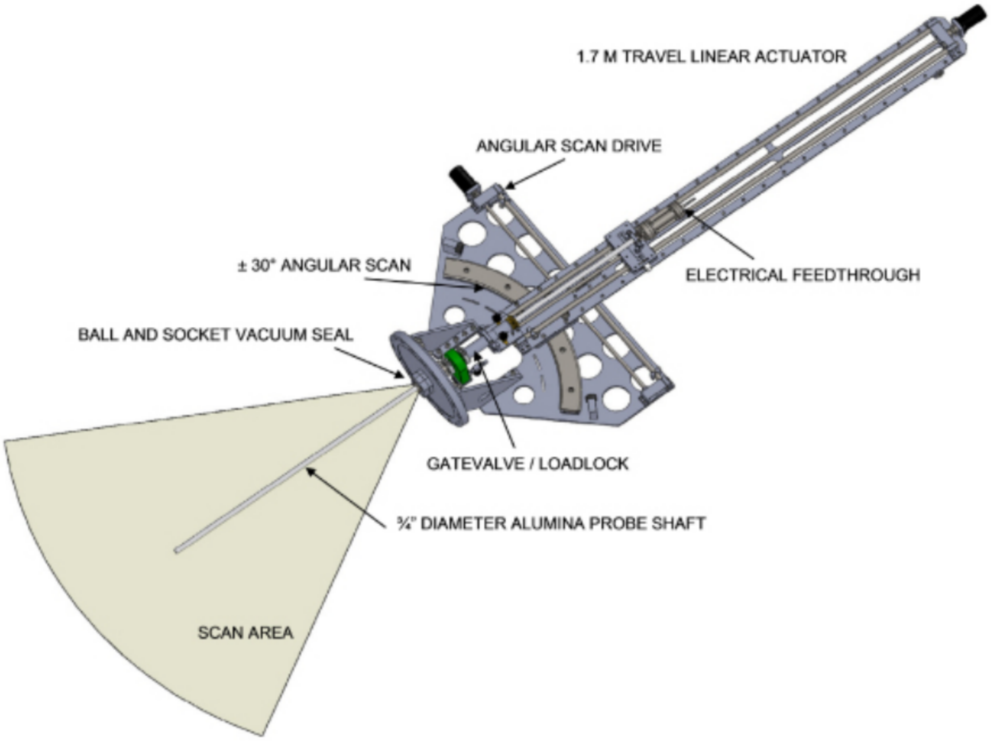

Figure 2.7: A CAD schematic of the sweep stage assembly. Rotation around the ball joint allows for coverage on a 2-dimensional plane inside the vessel. Figure taken from Ref. [55].

2.5 Control System

The control system for the BRB has been developed over time depending on the needs of specific experiments. It is largely based on the original MPDX controls designed by Dave Weisberg, but has since been significantly modified and extended upon by others to adapt the system for more general use. A lot of effort during this dissertation has been made to integrate each new system and component that was designed and built for the TREX experiments. A general description of the control system on the BRB follows in this section.

2.5.1 Labview

The experiment operator interfaces with a single computer in the BRB control room running a systems-design development environment called Labview[2]. Labview, created by National Instruments, is a visual programming language used for data acquisition and instrument control/automation and is highly optimized for parallel and multi-threaded execution. The programs and subroutines created in Labview are known as virtual-instruments, or VIs. These consist of a front panel, the user interface made up of virtual controls and indicators, and a block diagram which defines the function of the front panel objects. Labview is very flexible and is used to run essentially every task in the lab including turning on/off power supplies, sending triggers throughout the lab, and controlling the data acquisition for a given shot.

2.5.2 cRIO

Two National Instruments compactRIO (cRIO) systems are employed as part of the overall control system. A cRIO is a real-time controller that interfaces directly with Labview and supports numerous I/O modules with direct sensor connectivity or other special functionality. Many different modules are used throughout the lab for digitial and analog I/O, thermocouple sensor reading,

---

[2] In the nicest terms, the use of Labview is a necessary evil. It has a low barrier to entry in that non-programmers—like bright-eyed graduate students—can make useful VIs relatively quickly. However, in part because of its versatility, it is difficult for anyone without extensive knowledge of the Labview architecture to do anything well. The addition of some new functionality may disrupt previously working code, and rarely is it obvious what has gone wrong!

RS-232 communications, and external device control. The Helmholtz coil and capacitor banks used for the TREX experiments are controlled through the cRIOs.

2.5.3 Trigger Systems

The BRB control system includes a 24 channel trigger system with 1 ms accuracy used for precise timing of control signals during a single shot. Coming from an FPGA module, each signal output is optically isolated to limit ground loops and noise generation that may affect sensitive measurements. The pulse length is programmable and can be set to rising or lowering outputs. A secondary fast trigger system takes a primary trigger and can output another 32 triggers with 1 µs resolution. This secondary system is primarily used for pulsed power experiments like TREX. Ongoing effort is being made to implement a master clock integrated with a new isolated and fast trigger system to get all control signals and digitizers on a single timebase.

2.5.4 Data Acquisition

Prior to the addition of TREX, the BRB typically ran long duration plasmas (1-3 s) with slow timescale dynamics. As part of the work for this dissertation, a system of higher frequency digitizers was integrated into the BRB data acquisition system to accommodate the short duration, high frequency dynamics expected during magnetic reconnection. The BRB facility now operates with both "slow" and "fast" digitizers for any given shot.

The "slow" digitizers consist of seven D-TACQ Solutions ACQ196 modules for a total of 672 channels with up to 500 kSPS (samples-per-second) of 16-bit, fully differential inputs. The "fast" system uses 12 ICS-645 and 15 ICS-645B configurable digitizer cards for a total of 108 channels of 20 MSPS 12-bit or 864 channels of 2.5 MSPS 16-bit, single ended inputs. These digitizers are typically distributed around the lab and located near specific probes in order to reduce attenuation and parasitic losses associated with longer cables. Additionally, each digitizer rack is grounded directly to the vessel and care is taken to ensure remote connections (ethernet or trigger cables) are isolated to mitigate potential ground loops.

2.5.5 MDSplus

MDSplus is software that allows users to create a database to organize and manage experimental data in a hierarchical structure based around shot numbers. All data from the digitizers after a shot is taken is automatically uploaded to MDSplus and is easily accessed remotely.

2.6 Helmholtz Coil

The BRB originally had plans to install a large scale Helmholtz coil with the ability to generate a 100 G (0.01 T) magnetic field. However, with the increased needs associated with the addition of TREX, the first project undertaken for this dissertation was to design and construct an upgraded Helmholtz coil with nearly triple the field of the original design. This Section will detail the constraints and elements associated with the Helmholtz coil construction and power.

2.6.1 Alpha Power Supplies

The Alphas are three identical constant current power supplies previously chosen for use on the BRB Helmholtz coil that generate a maximum of $I_{Al} = 800$ A at $V_{Al} = 194$ V, continuous duty. Built by Alpha Scientific in the late 70s and early 80s, the Alphas were originally used on the Sustained Spheromak Physics Experiment at Lawrence Livermore National Laboratory and currently reside across from the N hemisphere of the BRB vessel. A large component of the overall Helmholtz coil project was testing the Alphas and ensuring they were operational for use, including integration into the BRB control system. For more detailed information on the Alpha power supplies and control interface, see Appendix B.

2.6.2 Details of the BRB Helmholtz Coil

To start, a Helmholtz coil is a particularly useful electromagnet configuration employed in many experimental contexts because of its simple design and ability to generate a nearly uniform magnetic field over a large volume. A Helmholtz coil consists of two identical coils placed coaxially with a coil separation h equal to the coil radius R_H. In this configuration, the magnetic field nonuniformity at the center of the coils is minimized ($\partial^2 B/\partial Z^2$=0 along the central Z-axis). Using the equation for the on-axis magnetic field of a single loop of current, it is simple to calculate the central magnetic field of a Helmholtz coil configuration

$$B_H = \left(\frac{4}{5}\right)^{3/2} \frac{\mu_0 I_{\text{tot}}}{R_H}\,. \tag{2.1}$$

Here, if N is the number of turns per coil and I is the current through each turn, then $I_{\text{tot}} = NI$. The full off-axis magnetic field can be solved analytically by using the equations for the magnetic vector potential provided in Jackson's *Classical Electrodynamics* textbook which are dependent on the elliptic integrals of first and second kind. This formulation is used for the remaining magnetic field calculations.

Each coil in the final design consists of 88 turns of water cooled copper conductor. The conductor is extruded with a 13 mm × 13 mm square cross-section and a 9 mm hole through the center for the water. The coil assembly cross-section is approximately 23 cm × 7 cm and consists of 16 individual loops of 5.5 turns of a single continuous conductor. Each loop is connected to the high pressure water system in parallel, and because of the half turn in each loop, there is a supply and return on each side of the coil. The conductor is intimately bonded to two layers of Daglas glass/polyester blend insulating material providing 600 V of electrical isolation. The loops are electrically connected in series to the adjacent loop and each coil is then connected to the power supplies. With one Alpha connected to each coil at 800 A, the maximum possible axial field is $B_H = 282$ G at the center of the device.

The Helmholtz coil frame and mounting structure was designed prior to the start of the project and took into account spatial limitations around the BRB vessel. Figure 2.8(a) shows an engineering drawing of the final coil design with measurements from the central axes. The main consequence of the frame is the coils are spread slightly farther than the coil radius. The radius to the center of the conductors is $R_H = 2.03$ m and the axial location of each coil is $Z_H = \pm 1.16\,\mathrm{m} > R_H/2$, making it not a "true" Helmholtz coil. As shown in Fig. 2.8(b) comparing the magnetic fields for both of these cases, the overall affect is not necessarily detrimental. For the case of the BRB Helmholtz coil, the axial field B_Z varies by only $\pm 2\%$ along the axis to the location of coils before

before dropping by only 9% near the wall relative to the center field. This is in contrast to the "true" Helmholtz configuration which drops more rapidly by 5% under the coils and 18% at the wall. In addition, B_Z drops by 24% (compared to 18 %) at the wall along Z=0 in the BRB case.

The copper conductor was purchased from Luvata, based out of Finland, on recommendation from other plasma laboratories. The conductor was then sent to Gebauer & Griller in Austria to be wrapped with insulation prior to shipping to the U.S. In total, each coil is comprised of over 1000 kg of copper. If you were to combine each loop of conductor end-to-end, it would extend over 2.2 km (1.4 mi) and stretch from the BRB laboratory in Sterling Hall to the Wisconsin State Capital building.

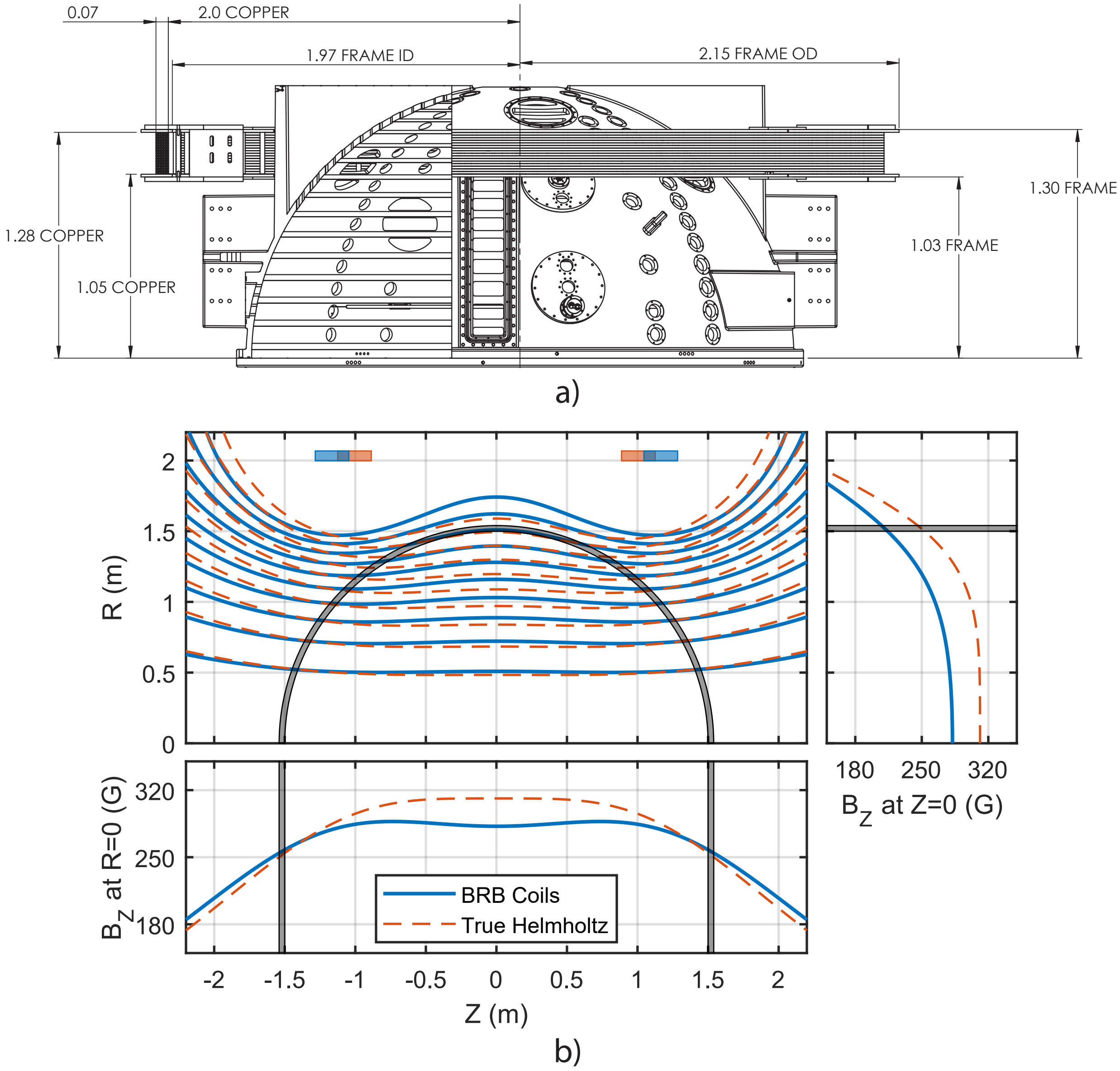

Figure 2.8: (a) An engineering drawing of the final design and spatial extents of the BRB Helmholtz coil with a top-down view of the S hemisphere. (b) A comparison of the magnetic field lines (contours of magnetic flux) for the BRB Helmholtz coil (blue) and a “true” Helmholtz coil (red-dashed). Profiles of the axial field B_Z along $Z = 0$ (right) and $R = 0$ (bottom). The blue and red squares mark the location of the Helmholtz coils while the grey regions indicate the BRB vessel wall.

2.6.3 Design Considerations

The ultimate goal in designing the Helmholtz coil is to maximize the magnetic field given a particular budget. In the end, the conductor size and shape, the insulation material, and total number of turns per coil must be optimized to meet the needs of the lab given the following design constraints: the limited space, the power supply output, the water cooling capacity, the cooling circuit design, water pressure limits, and the total cost. It is nearly impossible to find the single best solution given the sheer number of variables involved, so it helps to set limitations on certain variables.

The first is the choice to use extruded copper instead of extruded aluminum or standard electrical cable[3]. Next is to constrain the desired B_H, which is closely related to the total cost. For the given power, the only way to increase B_H is to add more turns, increasing the cost. Only through effort working with vendors and their available options was it determined that 80–100 turn coils was possible with the provided budget, providing enough B_H for the proposed experiments and potential future uses. Finally, the vendor, Luvata, was chosen to provide the hollow conductor, offering many different shapes and sizes, of which we opted for a square cross-section with a centered hole.

Finding the optimal conductor dimensions comes from considering further engineering restraints of the system. First a specific dimension is chosen from the available options and a total number of turns N_T is picked for now. The maximum number of loops n_l that can fit inside the frame is determined from the side dimension of the conductor. Additionally, the total resistance of the coil is

$$R_c = \frac{l N_T}{\sigma A_c}\,, \tag{2.2}$$

where l is the circumference of a single turn, σ is the electrical conductivity, and A_c is the annular area of the conductor. This must be less than the maximum load impedance of the Alpha $R_{\text{max}} = V_{Al}/I_{Al}$. Because the Alphas are decades old, it is especially important to avoid this limit in order

---

[3] Aluminum is an excellent economic choice for similar magnet systems. Keeping the final magnetic field the same, estimates of the cost for the Helmholtz coil would be $\sim 25\%$ lower than copper. However, this comes at the expense of size and space due to the increased resistivity and necessary increase in cooling flow rate. Additionally, aluminum is more sensitive to bimetallic corrosion which may lead to problems in shared cooling systems like on the BRB.

reduce the stress on the older electrical components, so a reasonable buffer is provided in the resistance limit.

At this time, the number of water cooling loops and turns per loop is not known, but can be constrained by the water cooling system. To counteract the Ohmic heating of the coil, chilled water is pushed through each individual loop providing active cooling. The total heat transferred is related to the mass and change in temperature of the water. For a steady state system, the rate of heat loss is

$$P_c = \rho c_p \Delta T U_{fl} \,, \tag{2.3}$$

where ρ and c_p are the mass density and specific heat capacity of water and U_{fl} is the volumetric flow rate. Here, $U_{fl} = V_{fl} A_{fl}$ given the velocity of the flowing water and the area of the center hole. An important limitation to V_{fl} must also be considered. Laminar flow through a pipe will lead to boundaries layers that limit heat transfer from the inner wall to the water whereas turbulent flow performs better for cooling scenarios. However, turbulent flow (characterized by high fluid Reynolds number, $Re \gtrsim 4000$) leads to increased erosion in soft materials like copper. This presents a limit in the flow velocity which has been empirically determined to be 5–8 m/s for colder water, and therefore limits the total cooling possible in each loop. Additionally, UW–Madison requires a $\Delta T < 17$ °C for their water systems. Given these limits and the number of loops, equating Eq. 2.3 to the Ohmic heating in one loop, $P_R = I_{Al}^2 R_{\text{loop}}$, provides a maximum number of turns per loop n_c.

The final consideration, is the pressure loss through the loop of coil. The loss in static pressure, or head loss, through a pipe is related to the flow velocity and the physical properties of the pipe. Analogous to increasing the voltage in a resistive circuit to increase the current, a larger pressure differential between the supply and return of the water cooling system is required to push more mass through the system. The relationship between the various parameters is empirically given by the Hazen-Williams equation

$$H = \frac{4.52 U_{fl}^{1.85}}{k^{1.85} d^{4.87}} \,, \tag{2.4}$$

where H is the head loss (in psi/ft), k is a roughness factor (≈ 140 for copper), and d is the diameter of the pipe. If each loop is connected in parallel, then this shows that the required pressure drop

Δp through a system is dependent on the length of each loop, A_{fl}, and V_{fl}. Similarly, given a reasonable $\Delta p \approx 50$ psi, the maximum length in each loop can be found, providing the maximum number of turns per loop n_p due to pressure loss through the coil.

The maximum number of turns for the chosen conductor is given by taking $n_l \times n_t$, where $n_t = \min(n_c, n_p)$. If this factor is more than number of turns picked at the beginning of the analysis then the chosen conductor dimensions work but can be further optimized. If less than, then the dimensions must be changed and the analysis completed redone. Through this process, the final dimensions can be determined in such a way as to maximize the number of turns while remaining within the constraints provided by Eqs. 2.2, 2.3, and 2.4.

The following provides an example of the above analysis using the chosen conductor dimensions, 13 mm×13 mm (9 mm). Choosing 80 turns to start, the number of loops that can fit inside the frame is $n_l = 19$. The total resistance of the coil from Eq. 2.2 is $R_c = 0.17\ \Omega$, which is within $R_{\text{max}} = 0.24\ \Omega$. At 5.5 ft/s, the flow rate through each loop is $U_{fl} = 1.69$ gal/min. So from Eq. 2.3, the maximum rate of heat loss is $P_c = 7.58$ kW, or the equivalent cooling for $n_c = 5.6$ turns per loop to balance resistive heating. Finally, with a $\Delta p = 50$ psi and given A_{fl}, the maximum length of each loop from Eq. 2.4 is $L = 250$ ft, the equivalent of $n_p = 5.9$ turns per loop. Choosing $n_t = 5$ turns per loop then implies the total turns possible is 95, greater than the 80 turns chosen, and therefore meets all the requirements of the system. However, either the conductor size or number of turns can be adjusted to better optimize these values. After many iterations, it was found that 16 loops of 5.5 turns of the 13 mm×13 mm (9 mm) copper conductor was a good fit for the BRB Helmholtz coil.

As previously mentioned, B_H is intimately related to the total cost C of the purchased conductor. This can be summed up by considering the cost based on the total mass of copper $C = \rho V c_m$, where V is the total volume and c_m is the cost per unit mass. Because of the relationship between total coil resistance and the cross-sectional area as well as the the total length and the number of turns, the previous expression can be written as

$$C = \rho c_m \frac{l^2 N_T^2}{\sigma R_c}\,. \tag{2.5}$$

This equation provides an estimate of the maximum number of turns possible for a given budget and coil resistance. If the maximum allowed coil resistance R_{max} (like from the Alphas), C,and c_m are known, then the maximum B_H is easily calculated. Eq. 2.5 can be added as a useful design constraint for future magnet systems.

2.6.4 Coil Construction

The conductor was shipped to UW-Madison in early 2014 in 33 separate spools (one extra for good measure). Each spool contained over 65 m of conductor corresponding to one continuous loop of the coil and weighing $\sim$ 78 kg. The major task then turned to constructing the Helmholtz coil set, which included winding the 4 m diameter coils around the already existing vessel structure.

To accomplish this, the engineering staff devised a scheme that allowed a single frame to be rotated in place. Shown in Fig. 2.9, a stand made of aluminum unistrut holds two roller bearings. The coil frame assembly is then removed from its mounting brackets and placed on the stand, able to spin on the bearings. An electric winch is used to control the speed of revolution.

With the copper conductor secured, its gradually unwound as the frame revolves. Throughout the process, one person applies a bead of construction epoxy between adjacent turns while another keeps the turns aligned. With one loop finished, custom clamps hold the copper in place while the epoxy cures. A ring of phenolic sheet is sandwiched between each loop for further electrical and mechanical isolation. With the full coil completed, the frame is reattached to the vessel structure. Hose barbs are brazed onto the ends of the copper and attached to a water supply/return manifold through non-conducting hose. Adjacent loops are brazed together for electrical continuity.

A switch board was designed to interface between the coils and the power supplies. Two 4/0-gauge welding cables connect each coil lead to the output of the switch board. Two more pairs of welding cable connect the input of the switch board to the Alphas. This system facilitates rapid configuration changes to the magnetic field that include changing between one or two Alpha supplies, reversing the direction, or running as a quadrupole field.

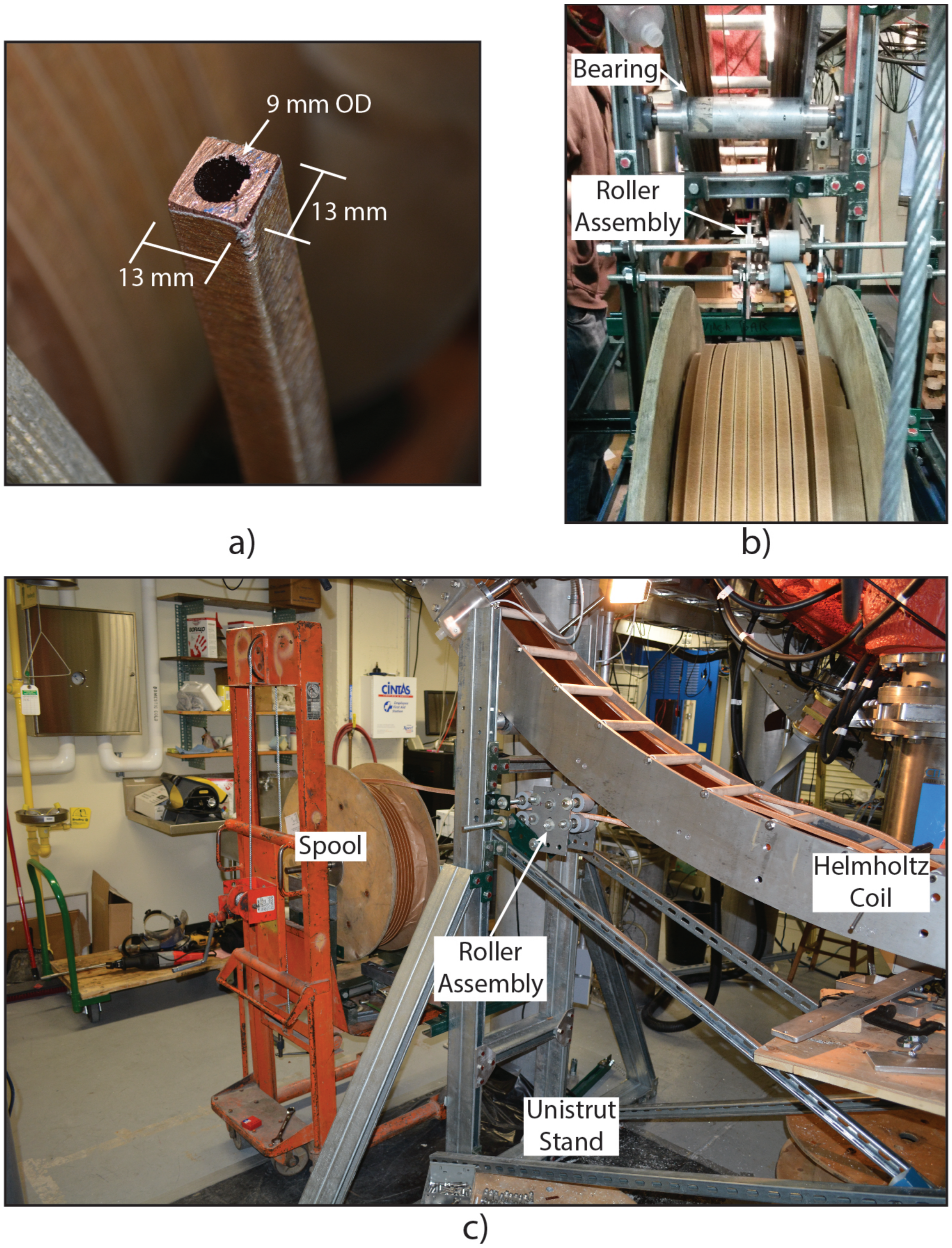

Figure 2.9: (a) Closeup picture of the copper conductor used for the Helmholtz coil wrapped with fiberglass insulation. (b) As the conductor comes off the spool, it runs through a roller assembly that helps straighten and align the copper before winding onto the coil frame. (c) The coil frame sits on an aluminum unistrut stand with two roller bearings that allow the frame to rotate in place. The conductor is unwound from the spool and onto the frame, making up a single loop of the coil assembly.

Chapter 3

The TREX Configuration

This chapter will detail the additional hardware created to implement the TREX configuration on the BRB device. Section 3.1 covers the drive coils and capacitor bank used to force reconnection on the experiment. The diagnostic suite designed specifically for these reconnection experiments is then described in Section 3.2. The components as presented here are used for the experiments covered in Chapter 4 and represent a single phase of the development of TREX that encompasses this dissertation.

3.1 The Reconnection Drive

3.1.1 Coils

The two internal drive coils are the primary components used for the reconnection scheme in the initial implementation of the TREX configuration. A picture of one of these coils is shown in Fig. 3.1 during installation inside the vacuum vessel. The coils were designed to be easily fabricated in-house and use readily available construction material. A single coil actually consists of two separate conductors in a coaxial arrangement that are powered by separate capacitor banks. The outer conductor is a 3/4 in. ID aluminum tube bent into a 90 cm radius circle with parallel leads that extend away from the main arc. Inside this outer conductor is a 3/8 in. ID copper tube, electrically isolated by 1/2 in. teflon tubing surrounding it. To protect the coils from the plasma, the outer conductor is plasma sprayed with alumina insulating material, the same material that lines the inside surface of the BRB. An electrically isolated vacuum feedthrough holds the coils in place with the help of two additional stainless steel spokes attached to the vessel wall. A 3D rendering of the full TREX configuration is provided in Fig. 3.2 with the two drive coils (purple) concentric about the central Z-axis of the device.

Figure 3.1: A single internal drive coil inside the BRB vessel during installation and alignment.

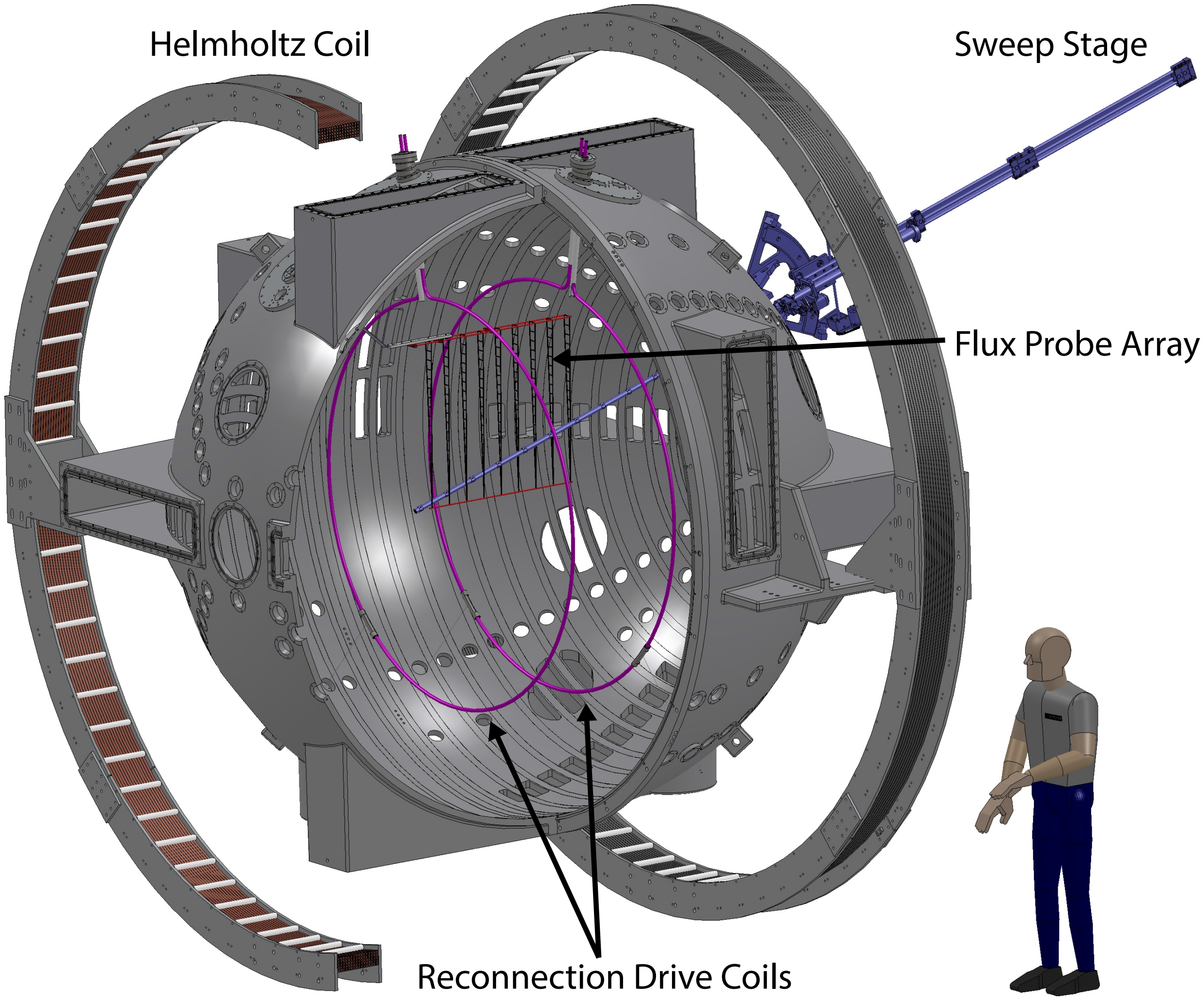

Figure 3.2: A 3D CAD rendering of the TREX experiment with the internal components visible. The reconnection drive coils (purple) are located along the central Z-axis, opposing the Helmholtz field during operation. The 80 cm×80 cm flux probe array (red/black) covers a significant area of interest for the experiment while the sweep stage (blue) is used to position other diagnostics throughout the volume.

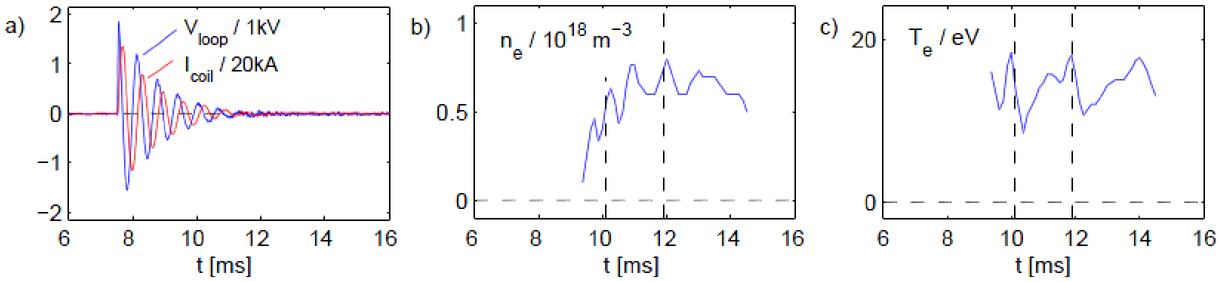

Figure 3.3: A demonstration of the heating drive in early TREX experiments. Pulsing an oscillating current (a) through a coil helps reach the target plasma density (b) and temperature (c).

3.1.2 Double Pulser Circuit

These early experiments utilized the LaB_6 cathodes as the plasma source, but early testing with the necessary Helmholtz field found these to generate plasma largely in a single flux tube connecting to an anode. It was determined that the plasma could be effectively homogenized by oscillating, or ringing, an internal coil. Results from testing a prototype drive coil are shown in Fig. 3.3. Here, the electron density and temperature fluctuate with the current and voltage in the coil. The minimal density at the start of the pulse increases to around 8×10^{17} m^{-3} while the temperature oscillates between 10 and 18 eV, demonstrating the effectiveness of this method for heating and reaching a uniform target plasma.

A similar technique is implemented for these experiments except that the "heating drive," as we call it, is independent of the main "reconnection drive." A schematic of the double pulser circuit built for these experiments is shown in 3.4. The two reconnection drive coils are connected in parallel with a total inductance $L \sim 20$ μH. The heater drive (right) consists of five parallel branches made up of a 100 μF capacitor in series with an ignitron switch. These are connected to the outer conductor of the coils and can be triggered independently for up to five heater pulses, allowed to ring with a damped LC response.

The reconnection drive (left) uses a much larger 1.4 mF capacitor connected through an ignitron to the inner conductor of the coils. This circuit limits the inherent LC ringing to a single positive current pulse with the addition of diodes in line with the inner coils. Additionally, an SCR is

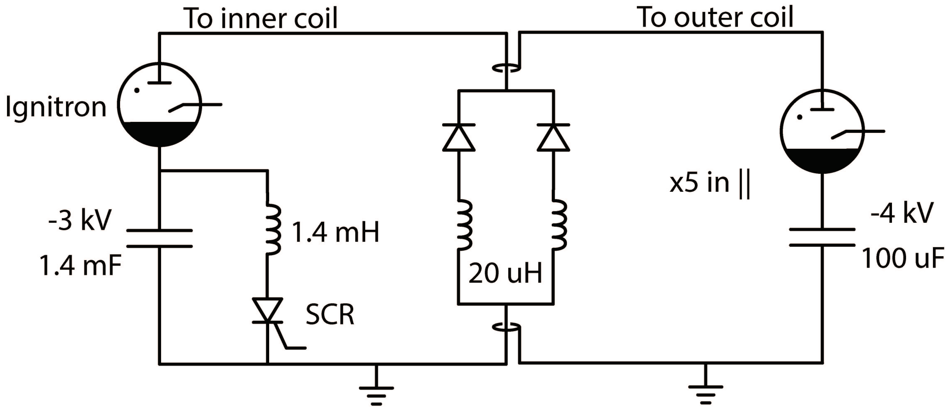

Figure 3.4: A schematic of the double pulser circuit used for heating the plasma (right circuit) independently of primary reconnection drive (left circuit.)

triggered as the capacitor voltage reverses, allowing the current to flow through a separate 1.4 mH inductor. The capacitor bank sits in a room across from the main experiment and is connected to the coils using 6 AWG twisted pair cables for both the heating and reconnection drives.

SCRs are commonly used for high power switching applications like these. However, they can be destroyed at the large values of $dI\,/\,dt$ needed for the loop voltages required here and more robust SCRs become increasingly expensive. Instead, class D ignitron switches are used in the double pulser circuit. An ignitron is a large steel tube containing a graphite anode and a pool of mercury for the cathode. An initial electrical pulse on an electrode ionizes the mercury and the resulting plasma is rapidly accelerated to the anode, allowing very high currents to pass through the ignitron. Ignitrons are rather old technology, but their ability to withstand high voltages ($>$30 kV) and currents ($>$100 kA) makes them extremely robust in this application. This circuit was developed with the help of our senior technician, Paul Nonn, who was essential in constructing the switching circuit (not shown) for the ignitrons. In particular, a much smaller series of capacitors sustains the current inside the ignitron while the voltage reverses in the LC ring and keeps the ignitron from prematurely shutting off.

An example experimental pulse in this configuration is provided in Fig. 3.6. The heater drive capacitors are charged to -4 kV and the main capacitor is charged to -3 kV. At $t = 0$ ms, the

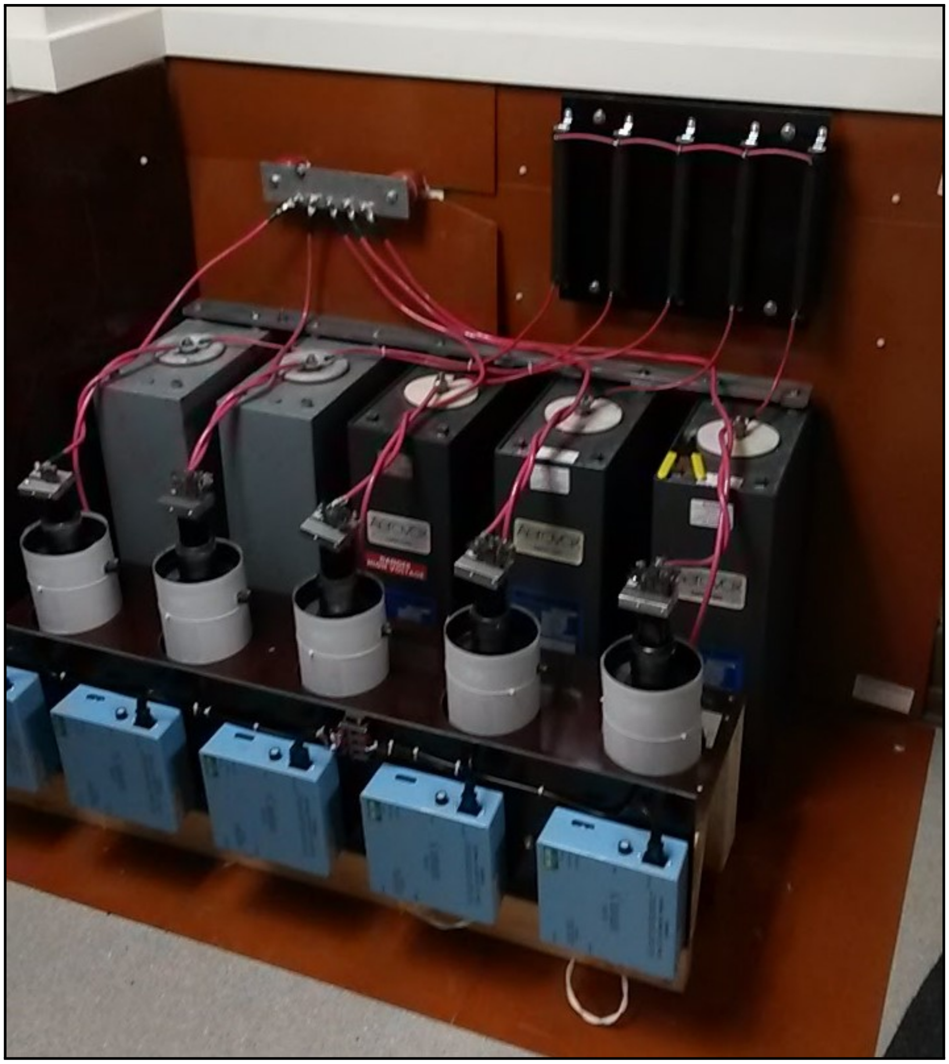

Figure 3.5: A picture of the 5 capacitor heater drive circuit. Each branch consists of a capacitor with its own high voltage ignitron switch. The blue boxes are Northstar IG5F2 drivers for triggering each ignitron.

$\mathrm{LaB_6}$ cathodes are triggered, generating a plasma which is disrupted as the first heater pulses are applied at 8.5 ms, 10 ms, and 11 ms. The interferometer trace, described in Section 3.2.1, shows the corresponding jumps in density associated with the heater pulses. The main reconnection drive, represented by the large, single pulse, is triggered at $t = 12$ ms. The ensuing reconnection event occurs as the initial current ramps up.

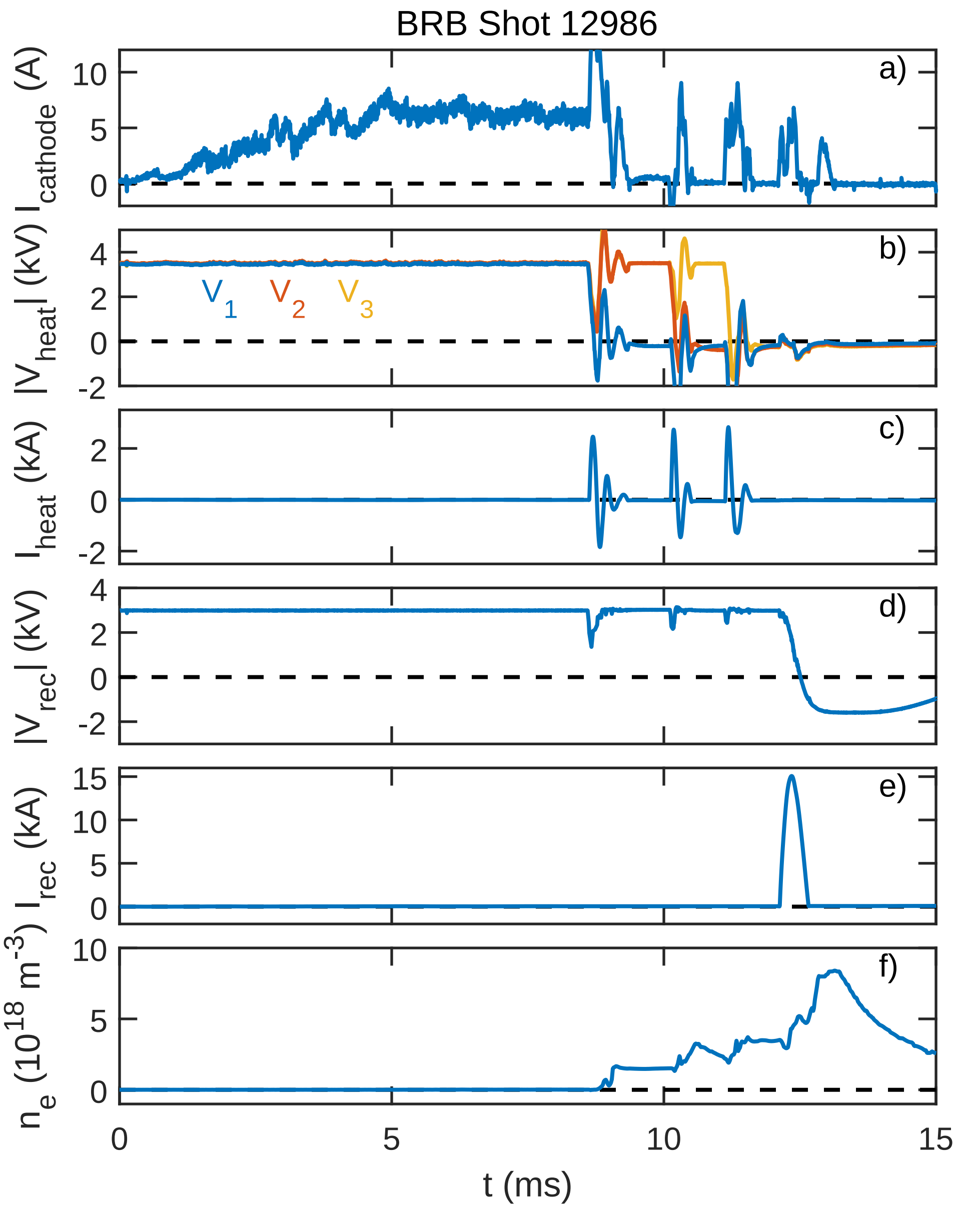

Figure 3.6: Measured traces of cathode current (a), heater drive capacitor voltages (b) and current (c) , reconnection drive voltages (d) and current (f) , and density (f) during a reconnection discharge in the early iteration of the TREX configuration.

3.2 Diagnostics

3.2.1 mm-Wave Interferometer

A line averaged density can be gathered from the use of a mm-wave heterodyne interferometer. This system uses two beams where one is sent through the plasma and back, picking up a phase shift relative to the second beam. The beams pass through mixers which output at an intermediate frequency (IF) typically set to 1-3 MHz and are then sent to an analog phase detector. The relative phase shift between the two beams is proportional to the electron density. On the BRB, a phase shift of 2π corresponds to a line averaged density of $n_{\text{fringe}} \approx 5 \times 10^{17}$ m^{-3}. This constitutes a limit in the rate of density change measurable by the system, i.e., if the density changes by more than n_{fringe} within a single IF period, then the fringe will be missed and lead to a discrete jump in the density trace. This condition is often exceeded during a reconnection pulse, and for this reason the interferometer was strictly used for background density measurements and for the calibration of other electrostatic probes.

3.2.2 $\dot{\mathrm{B}}$ Probe Array

A $\dot{B}$ probe, also known as a Mirnov coil, is one of the simpler plasma diagnostics to implement but also one of the most useful for basic plasma experiments. The probe is created by winding some number of loops N of conductor that enclose a small area A. Placed inside a region with changing magnetic field will induce an electric potential V across the leads proportional to the change in magentic flux through the surface such that

$$V = -\frac{d\Psi_B}{dt} = -NA\frac{dB}{dt}\,. \tag{3.1}$$

The magnetic field perpendicular to the enclosed coil surface can then be found by numerically integrating the measured signal voltage across the leads

$$B(t) = C\int_{t_0}^{t_f} V(t)\,dt\ . \tag{3.2}$$

where $C = -1/NA$ is a constant inverse to the total probe area.

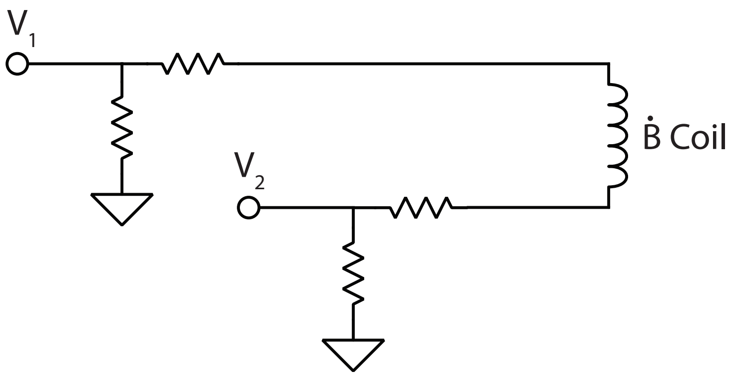

Figure 3.7: Schematic of the technique using two ground referenced digitizer inputs, V_1 and V_2, to take a differential measurement of a single $\dot{B}$ probe.

For use on TREX, a linear array of nine 3-axis $\dot{B}$ probes, spaced 10 cm apart for a total linear coverage of 80 cm, was placed inside a probe assembly similar to the one shown in Fig. 2.6. Each probe is connected to the TREX fast digitizers. Because the fast digitizers are single ended—referenced to the digitizer ground—they are especially susceptible to common mode noise. Two mitigate this, each pair of signal wires is measured through two individual digitizer channels, acting as a differential measurement. If V_1 and V_2 are the measured signals on each lead and CM is the common mode pickup then the total measured signal is

$$V = V_1 - V_2 \propto \left(\frac{\dot{B}}{2} + CM\right) - \left(-\frac{\dot{B}}{2} + CM\right) = \dot{B}\,. \tag{3.3}$$

This scheme is shown in Fig. 3.7 where each lead is measured across a voltage divider. Using this method removes the common mode pickup, leading to a cleaner signal overall.

Calibration of the probe is done by taking careful measurements of the probe area. On TREX, we also have the benefit of knowing that $B \to 0$ at the center of a current layer, or when $\dot{B}$ is at its maximum. Thus, using an actual experimental pulse allows for further refinement of the calibration relative to the large BRB Helmholtz coil.

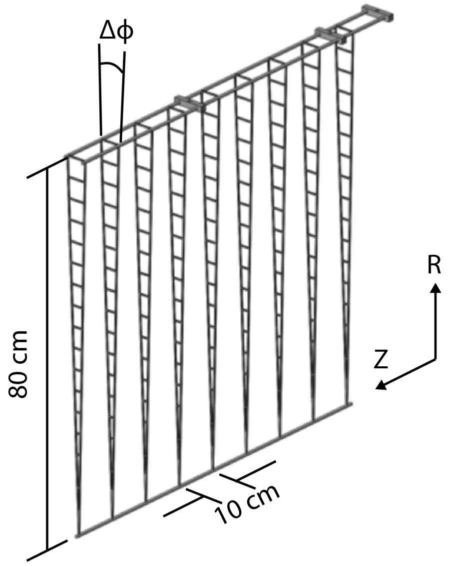

Figure 3.8: A 3D drawing of the flux probe array used on TREX. The width of the probes are proportional to R, making it possible to directly measure the magnetic flux function Ψ.

3.2.3 Flux Probe Array

The primary diagnostic used for this set of TREX experiments is what we call the flux probe array, similar to one used in previous reconnection experiments [59]. This array consists of a grid of magnetic $\dot{B}$ coils aligned in the cylindrical R–ϕ plane and arranged in 16 positions covering 80 cm in R and 9 positions covering 80 cm in Z. See Fig. 3.8 for a 3D rendering of the flux probe array as well as Fig. 3.2 for its placement in the device. Each probe subtends a small toroidal angle $\Delta\phi$ such that the width is proportional to R. Because of this symmetry, each loop measures a small portion of the change in magnetic flux

$$\Delta\dot{\Psi} = \dot{\Psi}(R_2, Z_1) - \dot{\Psi}(R_1, Z_1) = \int_{R_1}^{R_2} R'\dot{B}_Z(R', Z)\, dR' \ . \tag{3.4}$$

Integrating in time, the magnetic flux function is found exactly at each probe location such that

$$\Psi(R, Z) = \int_0^R R' B_Z(R', Z)\, dR' \ , \tag{3.5}$$

where $\Psi = RA_\phi$ is the definition for the poloidal flux function commonly used in axisymmetric devices. The radial integration is accomplished directly as the measurement of magnetic flux is continuous from $R = 0$ cm where $\Psi = 0$ to the R-location of each probe.

The magnetic flux function holds a lot of useful magnetic information. For example, by definition

$$\begin{aligned} B_R &= -\frac{1}{R}\frac{\partial \Psi}{\partial Z} \\ B_Z &= \ \ \frac{1}{R}\frac{\partial \Psi}{\partial R} \\ J_\phi &= -\frac{\nabla^2 A_\phi}{\mu_0} \,. \end{aligned} \tag{3.6}$$

From this, we see that $\mathbf{B} \cdot \boldsymbol{\nabla}\Psi = 0$, meaning Ψ is constant along poloidal fields lines $\mathbf{B_P} = \mathbf{B_R} + \mathbf{B_Z}$. Thus, measuring and plotting contours of constant Ψ represents the magnetic field lines in the R–Z plane.

Additionally, Ψ represents the total magnetic flux $\Psi_{\text{tot}} = 2\pi\Psi$ passing through a circle of radius R centered on the Z-axis. From Faraday's law, a change in the magnetic flux through the surface will induce an electric field (and loop voltage) around the surface. Thus, the toroidal electric field can be determined by the relation

$$E_\phi = -\frac{\dot{\Psi}_{\text{tot}}}{2\pi R} = -\frac{\dot{\Psi}}{R} \,. \tag{3.7}$$

Calculating E_ϕ at the X-line during reconnection provides a measurement of the amount of reconnected flux through the diffusion region given as E_{rec}.

Similar to Fig. 3.7, each loop of the flux probe array is measured differentially with two separate fast digitizer channels. With 144 individual loops, this totals 288 channels but is more efficient than what would be required to get the same spatial coverage and resolution with $\dot{B}$ arrays. Most of the magnetic details, like $\mathbf{B}$, $\mathbf{J}$, and E_ϕ, can be directly computed for a single shot over the entire 80 cm×80 cm array area.

3.2.4 $\mathrm{T_e}$ Probe

A Langmuir probe is another common plasma diagnostic. In essence, placing a small electrode at a potential V in a plasma with potential V_p will draw some amount of current dependent on the potential difference and the physical properties of the surrounding plasma. Analyzing this current through what's known as an I-V characteristic can help determine certain plasma parameters like the density n_e or the electron temperature T_e. Assuming that the plasma is Maxwellian, the Debye length is much smaller than the probe size, and where $T_i < T_e$, the total current out of the probe for $V < V_p$ is given as

$$I(V) = neA_p\left(\frac{T_e}{m_i}\right)^{1/2}\left[\left(\frac{m_i}{2\pi m_e}\right)^{1/2}\exp\left(\frac{e(V-V_p)}{T_e}\right) - \exp\left(-\frac{1}{2}\right)\right], \tag{3.8}$$

where A_p is the effective probe area. Here we use the convention that *electron* collection into the probe will result in a *positive* current. The derivation of this equation and more details about Langmuir probes can be found in many texts, including Refs. [60] and [61].

The first term in Eq. 3.8 is the electron current term in which only electrons with velocities that exceed the potential boundary, $v_e > \sqrt{2e(V_p - V)/m_e}$, will be collected. The electron flux to the probe is then just the flux due to thermal streaming of electrons reduced by the Boltzmann factor

$$\Gamma_e = \frac{1}{4}n\bar{v}_e \exp\left(\frac{e(V-V_p)}{T_e}\right), \tag{3.9}$$

where $\bar{v}_e = \sqrt{8T_e/\pi m_e}$ is the mean velocity for a Maxwellian distribution. For the ions, the potential drop from the probe to the plasma is found to occur over a small "sheath" region that's $\mathcal{O}(\lambda_D)$ where $\lambda_D = \sqrt{\epsilon_0 T_e/ne^2}$ is the electron Debye length. Far from the probe, the plasma satisfies quasineutrality such that $n_e \sim n_i \sim n$. The Bohm sheath criterion states that the density in the sheath is $n_s = \exp(-1/2)n$ and that the ions are accelerated by a non-negligible potential, in what's known as the pre-sheath, to the sound speed $c_s = \sqrt{T_e/m_i}$ at the sheath boundary. The ion flux to the probe is then given by

$$\Gamma_i = nc_s \exp\left(-\frac{1}{2}\right), \tag{3.10}$$

leading to the second term in Eq. 3.8. This is largely independent of the probe potential such that for a negative enough V in which most of the electrons are repelled, the current to the probe is given by

$$I_{is} \approx 0.61neA_pc_s\,, \tag{3.11}$$

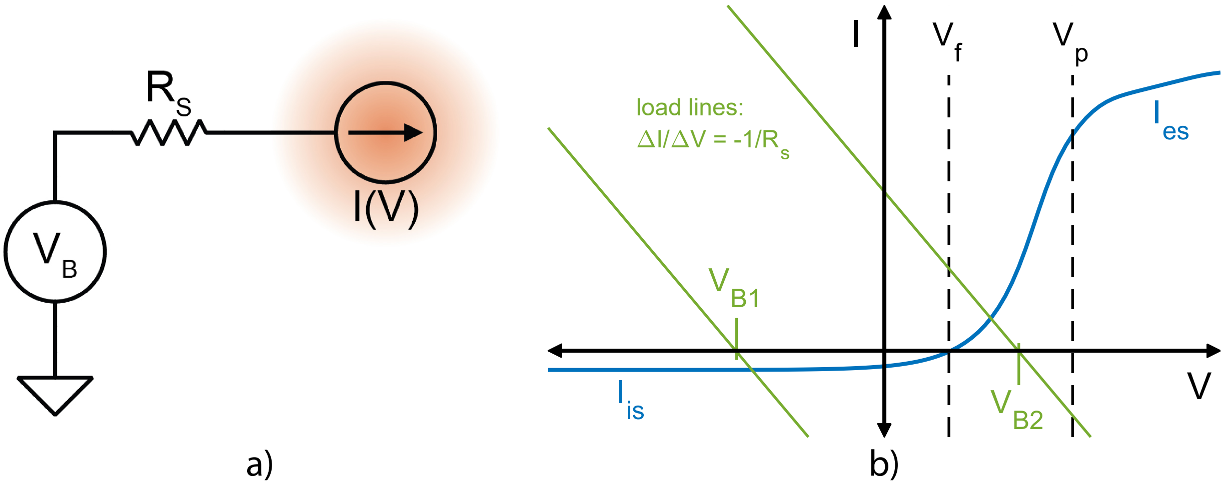

Figure 3.9: (a) A Langmuir probe is connected to a bias voltage through a sense resistor. (b) An example plasma I-V characteristic with locations of ion and electron saturation regions and plasma and floating potentials indicated. Provided a bias voltage, the probe current and voltage are given by the intersection of the load lines with the I-V curve.

also known as the ion saturation current. The derivation of Eq. 3.11 is specific to collisionless pre-sheaths, so the exact value of the coefficient in the Bohm criterion must be determined for collisional and magnetic effects. However, the differences typically aren't significant such that the coefficient in Eq. 3.10 is simply taken as $1/2$ with the recognition that the analysis is within some acceptable margin for error. In addition, an electron saturation current I_{es} region occurs when $V > V_p$, but the exact details of the current depend heavily on the plasma as well as the size and shape of the electrode. Generally speaking, Langmuir probe analysis is primarily limited to when Eq. 3.8 is valid.

A simplified Langmuir probe circuit is shown in Fig. 3.9(a) where an electrode is connected to a bias voltage V_B through a sense resistor R_S. The plasma itself will be described by some characteristic I-V curve (shown in Fig. 3.9(b)) that follows Eq. 3.8 for $V < V_p$. Inserting the probe tip into the plasma will draw a current through R_S such that $V \neq V_B$. The actual I and V measured by the probe is given by the point in which the circuit load line, with a slope of $-1/R_S$, intersects the true I-V curve. It follows that measuring the plasma at numerous V_B allows the full

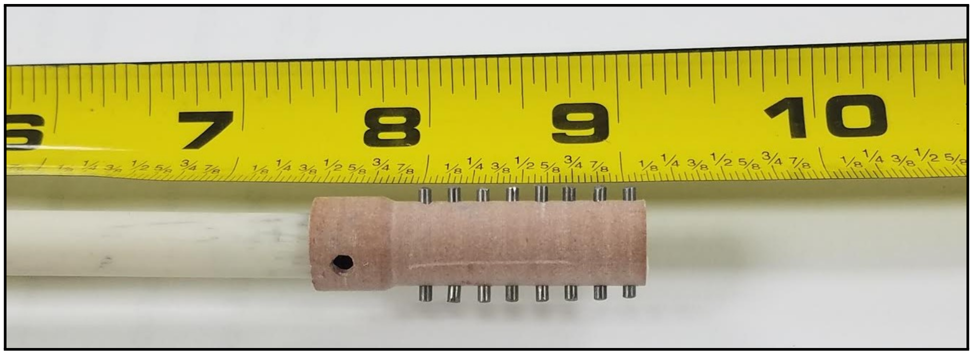

Figure 3.10: A photo of the T_e probe tip in which a full I-V characteristic can be captured at a single time point.

I-V characteristic to be sampled and the plasma properties to be ascertained by numerically fitting a curve to the measurement. For example, T_e can be determined from the slope of the exponential while n_e can be calculated from Eq. 3.11 for the ion saturation current. With a single Langmuir tip, a full characteristic can be sampled by sweeping V_B over a large range. However, for quickly varying plasmas like those observed during a TREX discharge, it can be difficult to attain a sweep frequency high enough to capture all the physics. In order to combat this limitation, we use a novel Langmuir probe design that we call the T_e probe.

The T_e probe consists of an assembly at the end of an alumina shaft with 16 individual Langmuir probe tips. A picture is provided in Fig. 3.10. The body is made out of alumina silicate (Lava) which turns into a hard ceramic after firing in a furnace. The 2 mm electrodes are cut from 1.5 mm molybdenum rod and arranged 3.5 mm apart with 8 tips per side. Thin enameled magnet wire is spot welded to each electrode and passed through a custom vacuum flange at the other end of the probe shaft. A cable then passes the connections to a rack housing the measurement electronics and dedicated digitizer.

Each probe tip has an independent measurement circuit shown in Fig. 3.11. Two power supplies provide a positive and negative voltage, V_+ and V_-, relative to the experiment ground, that feed into a 16 stage voltage divider. Taps at each stage provide 16 bias voltages V_1 to V_{16} ranging between V_+ and V_- that feed into 16 independent probe bias circuits similar to Fig. 3.9(a). Focusing on bias/tip 1, the voltage measurement V_{D1} at the digitizer with input impedance R_D follows a high

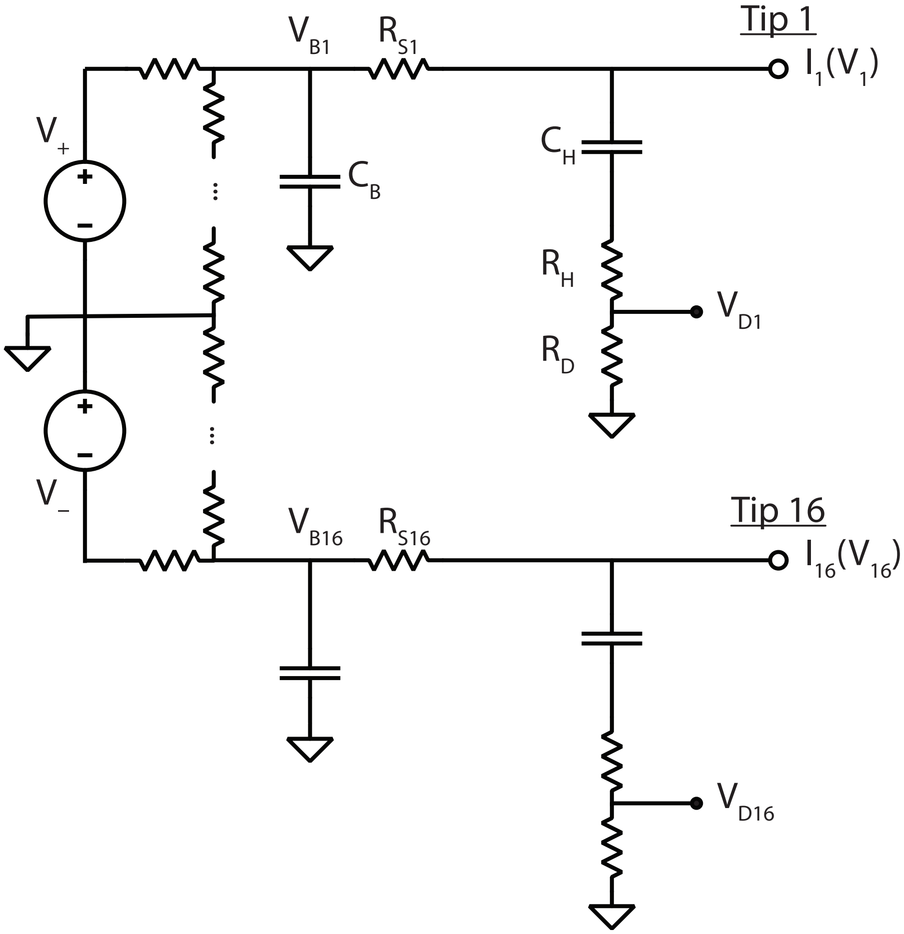

Figure 3.11: Circuit diagram of 16 tip probe electronics.

pass filter with $C_H = 10$ µF and $R_H > 10$ kΩ such that $R_H C_H > 100$ ms. This is long enough to decouple the typically large DC bias voltage while still passing all the faster time varying voltages through during a shot. Thus, the voltage drop across R_{S1} is given by $\Delta V_{S1} = V_{D1}(R_H + R_D)/R_D$ such that the probe current and voltage are

$$I_1 = \frac{\Delta V_{S1}}{R_{S1}} \tag{3.12}$$

$$V_1 = V_{B1} + \Delta V_{S1}\,. \tag{3.13}$$

This same procedure is done for all the tips and applied biases. To supplement the current needs during a shot, a large 1.5 mF electrolytic capacitor C_B sits across each bias voltage. This serves as a source/sink for the rapidly changing probe current and effectively keeps the bias voltage constant during a shot. With this configuration of Langmuir probes, the I-V curve is sampled at 16 different voltages at the full digitizer sampling rate (5-10 MHz). With the appropriate range of biases (as large as ± 150 V), the resistors can be chosen to optimize the sensitivity to and range of measurable parameters. Additionally, at the center of the Lava body is a 3 axis $\dot{B}$ coil used to measure the local magnetic field at the exact location of the probe tip. This provides timing of the T_e probe signal relative to other diagnostics on the experiment by directly measuring the passing reconnection current layer.

Chapter 4

Demonstration of the Collisionless Plasmoid Instability below the Ion Kinetic Scale

This chapter reports on the formation of spontaneous magnetic islands observed in driven, anti-parallel reconnection on TREX. These experiments occur in a low collisional regime and at small relative system size. The experimental evidence provided shows that the plasmoid instability is active at the electron scale inside the ion diffusion region and are not predicted by extended MHD or fully collisionless simulations. Olson *et al*, PRL (2016) [62] is a shorter, published version of the material presented in this chapter. Reuse of figures and text herein is granted by APS Publishing.

4.1 Background

Resistive fluid models (Resistive MHD) show that as the resistivity of the plasma is decreased to a sufficiently low value then reconnection will transition from a slow regime characterized by Sweet-Parker reconnection [3, 4] into a much faster regime characterized by the formation of magnetic islands [22], also called plasmoids. Based on work using primarily 2D fluid models, it has been theorized that the island instability is responsible for the onset of solar flares [6]. Furthermore, subsequent coalescence of magnetic islands may provide an effective mechanism for generation of superthermal electrons [63]. From theory, it is expected that the magnetic island instability becomes effective when reconnection current layers become much larger than length scales associated with the ion dynamics. In contrast, we provide direct experimental evidence that the magnetic island instability is active when the current layer is at length scales associated with the electrons.

The plasma regimes where plasmoids (or multiple X-line reconnection) are expected can be laid out using a phase diagram developed by Daughton and Roytershteyn [47] as a function of the Lundquist number S and the normalized system size $\lambda = L/min(d_i, \rho_s)$, where $S = \mu_0 L_{\mathrm{CS}} v_A/\eta$, L_{CS} is the size of the current sheet, v_A is the Alfvén speed evaluated using the reconnection magnetic field, and η is the plasma resistivity. Here, λ is relative to the characteristic ion dynamics length scale, the smaller of the ion skin depth, $d_i = c/\omega_{pi}$, for antiparallel reconnection or the ion sound Larmor radius, $\rho_s = (m_i(T_i + T_e))^{1/2}/eB$, for guide field reconnection. Figure 4.1 displays this phase diagram, summarizing the current theoretical and numerical understanding of reconnection dynamics.

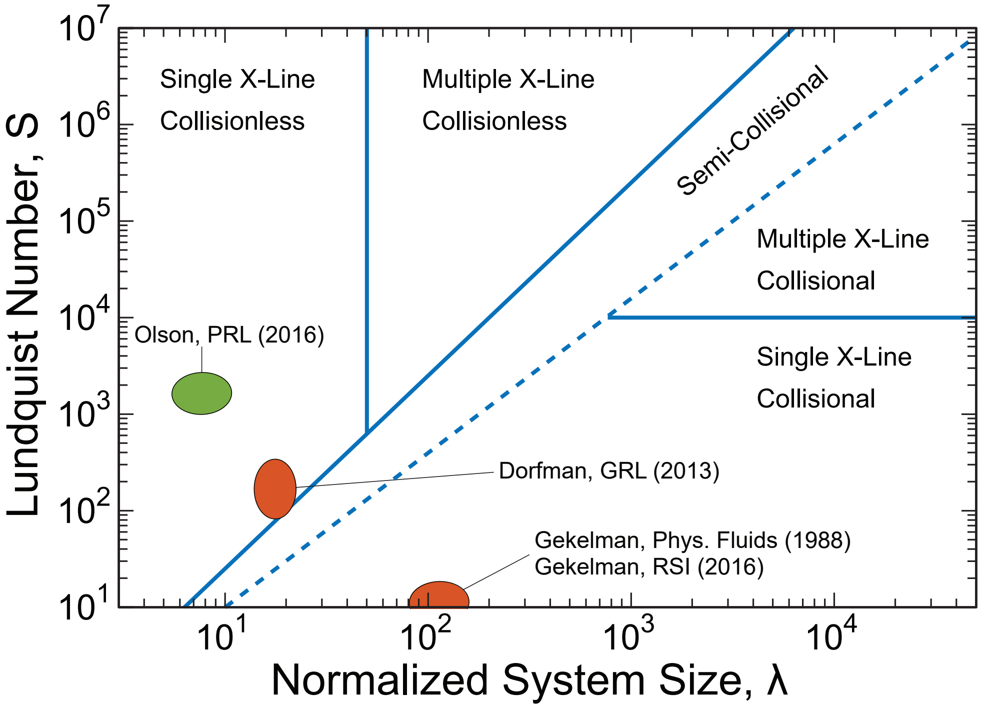

Figure 4.1: Theoretical phase diagram indicating different regimes of reconnection where multiple X-lines separated by plasmoids are expected for both collisional and collisionless reconnection as a function of the Lundquist number and the normalized system size. Other noteable results from tearing experiments are marked with red ovals. The results presented here fall into the collisionless regime where multiple X-lines are not expected from theory.

Collisional reconnection becomes susceptible to magnetic island formation above a critical Lundquist number $S_{\text{crit}} = 10^4$ [35], marked by the horizontal line. As the collisionality decreases and the Sweet-Parker current layer width approaches the appropriate ion kinetic scale [64, 12] a transition to collisionless reconnection occurs, dominated by kinetic effects. This regime is indicated above the solid diagonal line [48]. Though there is no analytic theory, large scale PIC simulations indicate the presence of multiple X-lines above a critical system size $\lambda_{\text{crit}} \sim 40$, the vertical line, during collisionless magnetic reconnection [65, 66].

The existence of magnetic islands is well documented through *in situ* observations [67, 68, 69] under fully collisionless conditions in Earth's magnetotail and can also be observed during solar flare events [70, 71]. Transient reconnection can also lead to small scale magnetic substructures at secondary reconnection sites many d_i from the central X-line [72, 73]. In laboratory experiments, direct observation of secondary magnetic islands has been limited due to the inability to reach the critical parameters predicted by theory. The recent inclusion of a semi-collisional region [74] likely accounts for some of the islands observed in the Magnetic Reconnection Experiment (MRX) [75] and in more recent pulsed power reconnection experiments [76]. Additionally, studies of electron layer tearing have been done on linear experimental devices at large guide field and small reconnection magnetic field values, placing these experiments in a low-S and high-λ regime [77, 78]. In contrast, the magnetic islands discussed here are sufficiently collisionless and develop at such small normalized current layer length scales that their occurrence is unexpected based on theory.

4.2 Experimental Setup

These experiments utilize the hardware described in the Chapter 3. A poloidal cross section of the vessel is shown in Fig. 4.2 in which the defined R-Z plane, with the positive toroidal direction pointing out of the plane, is used for all future plots. For the presented experiments, Helium plasmas are initiated by biasing LaB_6 electrodes at the edge of the vessel (not shown) followed by three "heating" pulses as described in Section 3.1 to reach the target plasma. The basic configuration uses a steady, axial magnetic field from an external Helmholtz coil with no applied guide field in

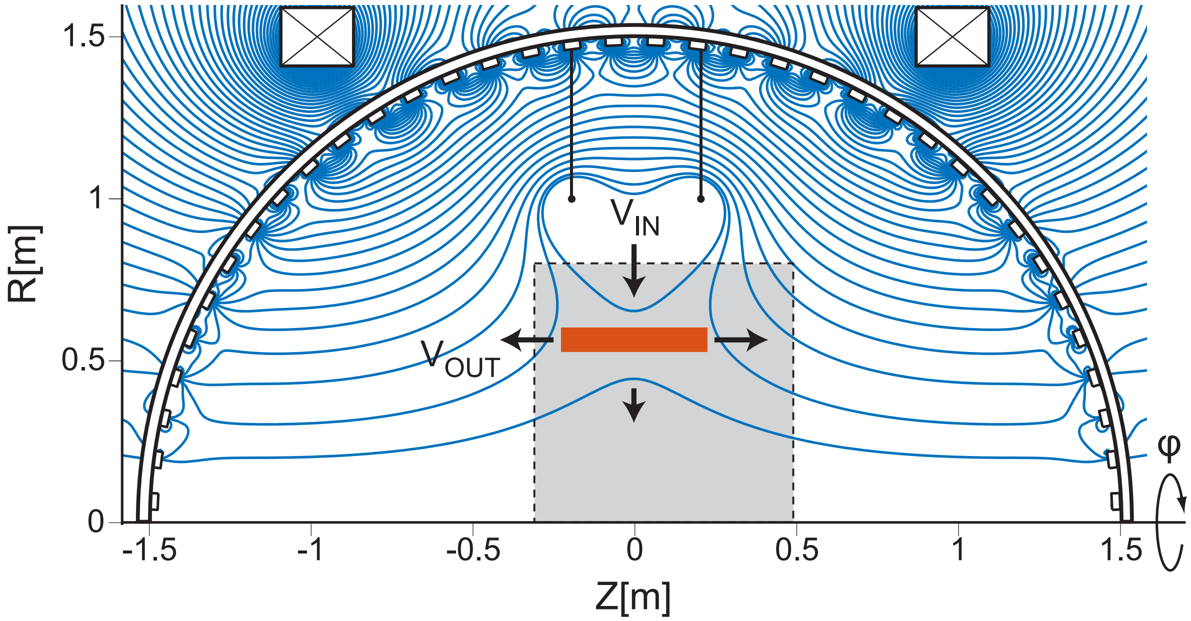

Figure 4.2: To drive reconnection, the internal coils are pulsed opposite the steady state field provided by the external Helmholtz coil (not to scale). The resulting vacuum magnetic field (blue) is overlaid with an illustration of the plasma inflows and outflows as the reconnection current layer (orange) propagates toward the center of the vessel. The shaded grey box indicates the areal coverage of the array of 144 magnetic flux probes.

the toroidal direction. In addition, two 1.8 m diameter coils at $Z = \pm 0.2$ m are installed inside the vacuum vessel and pulsed opposite the background axial field. During the initial phase of coil energization, new magnetic flux surfaces expand rapidly away from the coils, pushing against the Helmholtz field and forming the reconnection current sheet at the resulting magnetic null. As the current in the internal coils is rapidly increased, the reconnection layer migrates toward the center of the device. The resulting vacuum field is sketched in Fig. 4.2. The setup is nominally 2D due to the axisymmetry of the device about the Z-axis, but 3D effects can develop freely during the reconnection process, as in any experiment. The facility allows for experimentation with plasmas in a parameter regime where collisions do not influence the momentum balance between the electrons and ions.

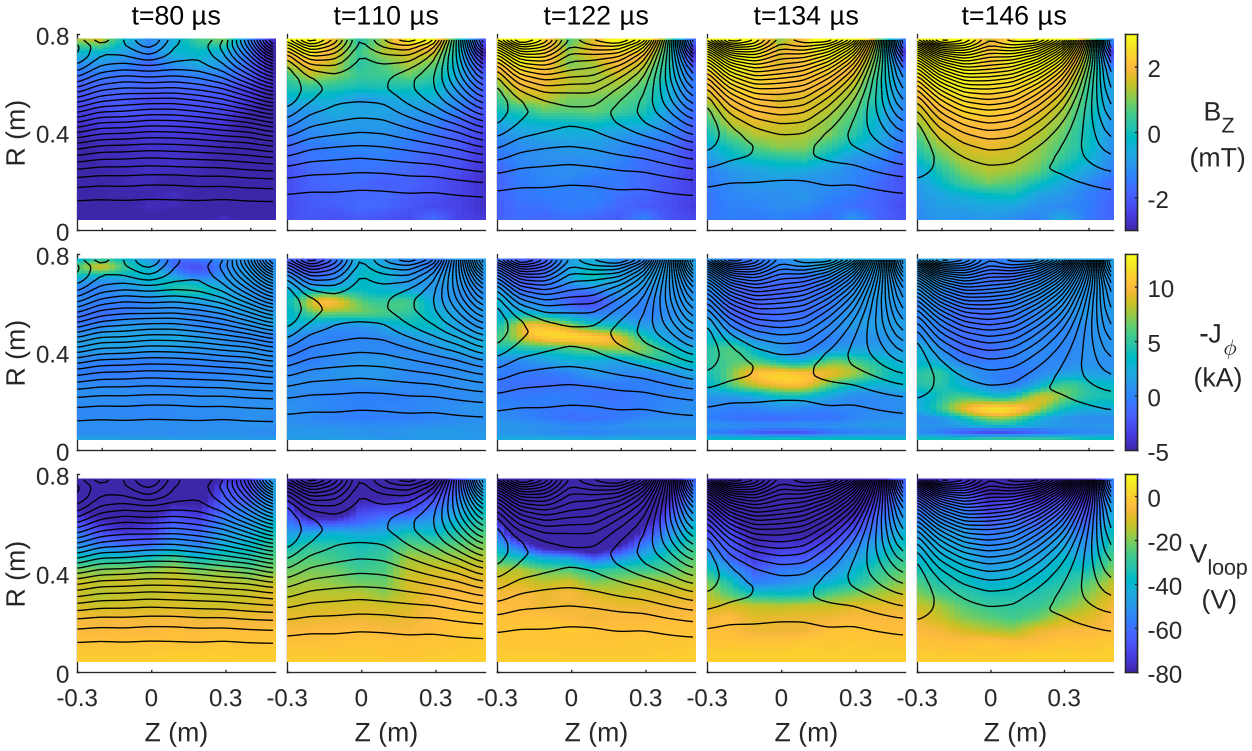

Figure 4.3: Profiles of B_Z, $-J_\phi$, and V_{loop} taken from the flux probe array at different times during an experimental pulse showing the transit of the reconnection current layer. The black lines are evenly spaced contours of constant Ψ representing the poloidal magnetic field lines and relative field strength.

In addition to the flux probe array, the linear array of 3-axis $\dot{B}$ probes measures magnetic signals in a separate toroidal plane, offset by 15°. This array is positioned parallel to the Z-axis at $R = 0.4$ m with the same span in Z as the flux probe array and is oriented such that the probe axes are aligned with the experiment axes. For these experiments, the T_e probe is located at $R = 0.4$ m and $Z = 0.0$ m with the tip biases ranging between ± 120 V. Values for the plasma density and temperature at the location of the T_e probe are then inferred from the full I-Vcharacteristic for each time sample. All the diagnostics are measured at the digitization frequency of 2 MHz.

An example experimental pulse is shown in Fig. 4.3 with profiles of B_Z, J_ϕ, and V_{loop} at different times during the pulse based on the measurement of Ψ, taken from the flux probe array covering $R = 0$–0.8 m and $Z = -0.3$–0.5 m. These key profiles characterizing the reconnection process are readily computed using Eqs. 3.6. The applied Helmholtz field is in the $-Z$ direction with a strength of $B_H = 5$ mT. The reconnection pulse occurs at $t = 0$ µs with the coil in the $+\phi$ direction, producing an expanding bubble of positive B_Z seen in the top row. The second row shows the current layer form below the coils between t =80–90 µs in the $-\phi$ direction to counteract this change in flux and proceed at a roughly constant layer velocity of $v_{\text{layer}} = 4$ km/s. These profiles highlight the dynamics of the current layer during a reconnection event whereas the analysis in the following section will focus the analysis at a single radial location. Note that the negative of J_ϕ is shown in this figure and throughout this chapter for clarity.

4.3 Low Collisional Reconnection Regime

For the event presented in Fig. 4.4, the reconnection current layer is observed at $R = 0.4$ m at $t \approx 145$ µs. The in-plane magnetic field B_Z and out-of-plane current density J_ϕ shown in 4.4(a-b) are calculated from the flux probe array. The contours of Ψ provide the instantaneous geometry of the in-plane magnetic field lines. The current layer and magnetic null separates the two inflow regions of oppositely directed magnetic fields. Here we note how the TREX configuration allows for long current layers to form without the reconnection exhausts being obstructed by downstream obstacles and associated pressure build-up influencing the reconnection rate [23].

The quadrupolar Hall magnetic fields, transverse to the reconnecting plane, are clearly present in Fig. 4.4(c) and serve as a signature of two-fluid reconnection [79]. They are generated by the Hall currents resulting when the ion and electron fluids decouple inside the ion diffusion region, which has a characteristic width of an ion skin depth. The Hall fields have been observed *in situ* by spacecraft [80] and previous laboratory experiments in MRX [31]. Here, a technique known as the “jogging” method is applied. This method is an extension of Taylor’s hypothesis relating the temporal and spatial characteristics of turbulent eddies and is commonly used in spacecraft analysis as well as prior experiments [81]. If the spatial structure of some quantity—like magnetic field or density—has little intrinsic variation as it moves past a single location in space, then the total temporal change will be caused by the uniform movement of an unchanging spatial pattern

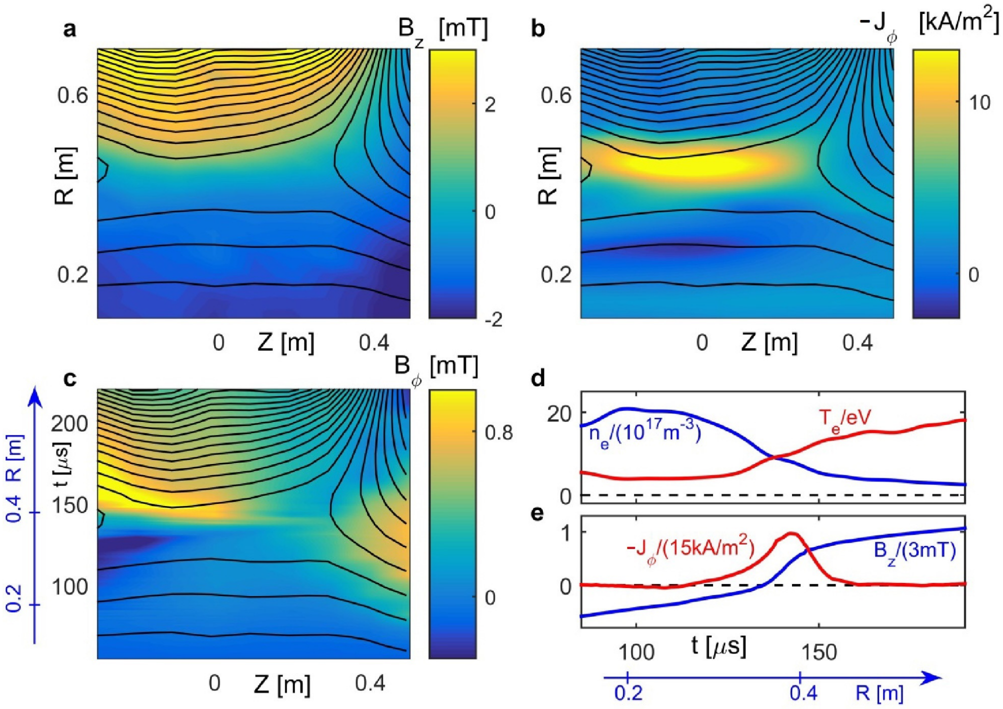

Figure 4.4: Profiles of (a) the reconnecting magnetic field B_Z and (b) the out-of-plane current density $-J_\phi$ measured by the flux array The contour lines of constant Ψ show the in-plane projection of magnetic field lines. (c) The out-of-plane Hall magnetic field B_ϕ measured by the linear magnetic array. (d) Profiles of the electron density and temperature measured by the T_e probe. The temporal axis in (c) and (d) is converted to a spatial axis knowing the velocity of the current layer, $v_{\text{layer}} \sim -4$ km/s, as it flows past each probe. (e) Profiles at $Z = 0$ m of J_ϕ and B_Z inferred from (a) and (b).

passing that location. As seen in Fig. 4.3, the structure of the current layer and magnetic field lines is roughly constant as it traverses through the experiment. Therefore, the temporal signals from the $\dot{B}$ probe array can be converted into a spatial profile where $\partial R \approx v_{\text{layer}}\partial t$, taking advantage of the increased temporal resolution of the diagnostic.

Similar to configurations in the solar wind [82] and in the dayside magnetopause [83], the reconnection layer in TREX plasmas exhibits strong asymmetries in kinetic profiles across the current sheet. Using the T_e probe described earlier, time profiles of number density n_e and electron temperature T_e were obtained as displayed in Fig. 4.4(d). In addition, the profiles of B_Z and J_ϕ in Fig. 4.4(e) were inferred from the flux array data at the location of the T_e probe. Together, these profiles show asymmetric reconnection with an enhanced plasma density $n_1 \approx 2 \times 10^{18}$ m^{-3} on the low-field side of the reconnection layer, $B_{Z1} \approx -1.5$ mT, compared to $n_2 \approx 4 \times 10^{17}$ m^{-3} on the high-field side, $B_{Z2} \approx 3$ mT. We note that the asymmetries in the profile of B_ϕ in Fig. 4.4(c) are consistent with the expectations for asymmetric reconnection [84] where the Hall fields are most pronounced on the side of the current layer with the largest B_Z.

As described before, the out-of-plane inductive electric field E_ϕ is also easily computed from the magnetic flux function. The value of E_ϕ at the X-point (magnetic null) is taken as the reconnection electric field E_{rec} and characterizes the fast reconnection rate on TREX. In the absence of magnetic island dynamics, the observed reconnection electric field is approximately $E_{\text{rec}} \approx 15$ V/m with a current density of $J_\phi \approx 15$ kA/m^2. Following the formalism of previous experimental investigations, we may then infer an effective resistivity

$$\eta^* = \frac{E_{\text{rec}}}{J_\phi} \approx 10^{-3}\ \Omega\text{m}\,. \tag{4.1}$$

In comparison, for the observed electron temperature of $T_e \approx 10$ eV within the current layer, the transverse Spitzer resistivity is $\eta_{\text{sp}} \approx 8.8 \times 10^{-6}$ Ωm. Thus, the ratio of the effective resistivity to the Spitzer value,

$$\frac{\eta^*}{\eta_{\text{sp}}} \sim 10^2\,, \tag{4.2}$$

is larger by about a factor 10 compared to those observed in MRX [64]. We also note the reconnection electric field is well above the Dreicer limit

$$E_D = \frac{\nu_{ei}\sqrt{m_e T_e}}{e} \approx 2.5\ \text{V/m}\,, \tag{4.3}$$

where the electron acceleration outweighs the collisional drag.

The reconnection geometry can be characterized by a set of dimensionless parameters appropriate to asymmetric reconnection [85]. We use the electron density $n_e \sim 10^{18}$ m^{-3} observed in the center of the current layer to evaluate the typical electron and ion skin depths, $d_e \approx 0.006$ m and $d_i \approx 0.54$ m. Thus, the size of the experiment is about $L_{exp} \approx 5d_i$, while the half length of the current layer is $L_j \approx 0.7d_i$. Normalized to the electron length, we note that $L_j/d_e \approx 90$ is similar to that observed in kinetic simulations. Meanwhile, the observed normalized half width of the current layer $\delta_j/d_e \approx 8$ is wider than what is observed in kinetic simulations, but similar to other reconnection experiments [86]. To evaluate the relevant Alfvén speed for the asymmetric configuration we follow the convention of Ref. [85] which defines a hybrid-Alfvén velocity

$$v_{\text{Ah}} = \left(\frac{1}{\mu_0 m_1} \frac{B_1 B_2 (B_1 + B_2)}{n_1 B_2 + n_2 B_1} \right)^{1/2} \approx 20 \text{ km/s} \tag{4.4}$$

that utilizes both upstream density and magnetic field values. We may then calculate the Lundquist number $S = 2L_j \mu_0 v_{\text{Ah}} / \eta_{\text{sp}} \sim 10^3$ where $2L_j \approx 0.7$ m is used for the length of the current layer. Furthermore, the typical E_{rec} is larger than the expected reconnection electric field provided in Ref. [85],

$$E_{\text{CS}} = \frac{\delta_j}{L_j} \frac{2B_1 B_2}{B_1 + B_2} v_{\text{Ah}} \approx 6 \text{ V/m} \tag{4.5}$$

such that $E_{\text{rec}}/E_{\text{CS}} \sim 3$. The phase diagram in Fig. 4.1 is updated with the measured values from these experiments and, with the preceding analysis, confirms that TREX operates deep in the collisionless reconnection regime.

4.4 Spontaneous Formation of Plasmoids

Of particular interest from this set of experiments is the spontaneous formation and ejection of often multiple magnetic islands, or plasmoids, from within a single reconnection layer. As an example, Fig. 4.5 provides snapshots of the plasma current density overlaid with contours of constant Ψ during a particularly dynamic plasmoid event. Initially, the reconnection current layer is formed as in Fig. 4.4(b). Figures 4.5(a-b) then show reconnection transition to two X-points within the current sheet (along the $B_Z = 0$ dashed line) with an O-point between them growing to form the first plasmoid. The closed contour observed in Fig. 4.5(c) representing the magnetic island is $\sim 0.1d_i$ wide. As the plasmoid grows, the layer transit stagnates until the plasmoid is ejected due to the magnetic tension, corresponding to a sharp decline in the current density. The current layer recovers and then continues to reconnect as usual until a second plasmoid is formed and subsequently ejected. With $S \sim 1000$ and $L_j/d_i \sim 1$, it is expected that the experiment will

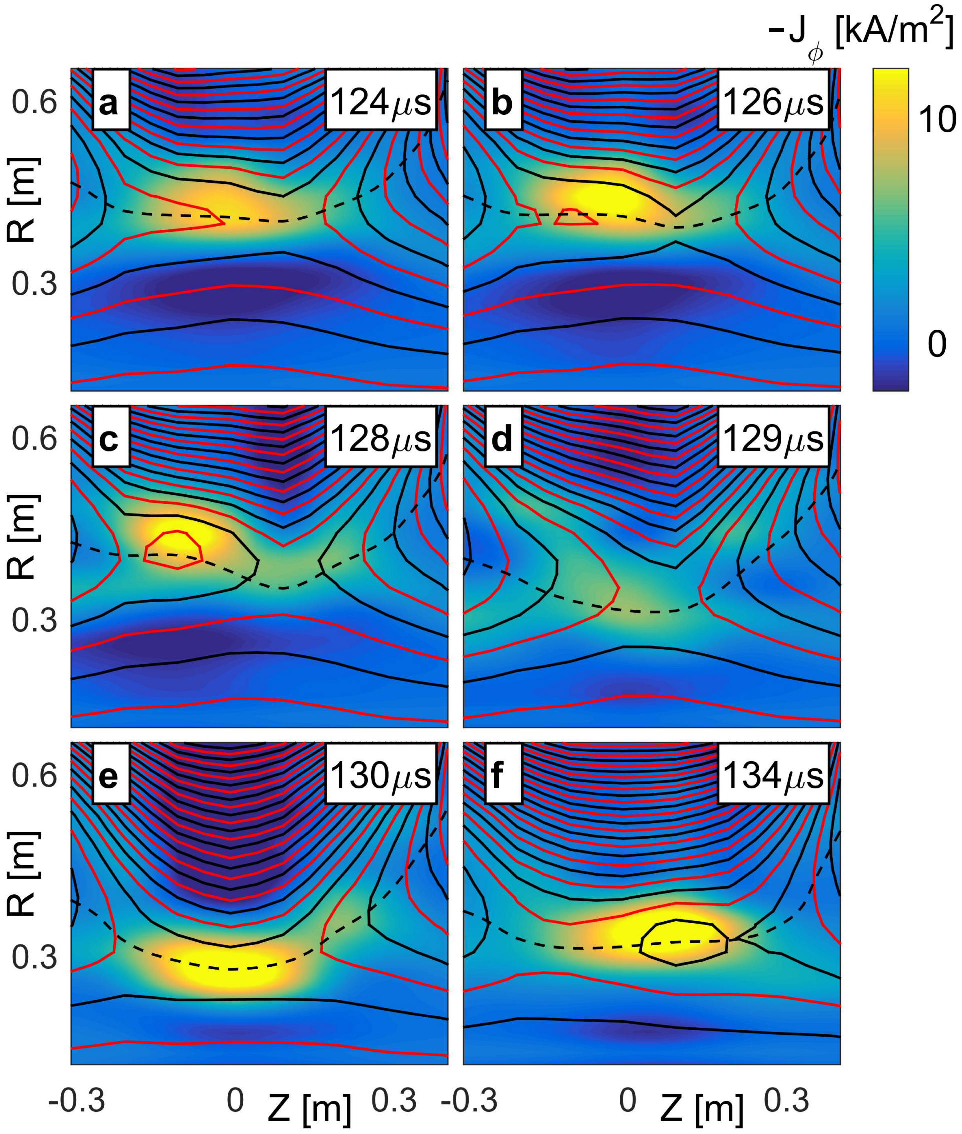

Figure 4.5: Measured 2D profiles of the out-of-plane current density J_ϕ and magnetic flux contours, $\Psi =$ constant. The occurrence of separate plasmoids are clearly visible for $t = 128$ μs and $t = 134$ μs. The dashed lines indicate the midplane where $B_Z = 0$. Here 1 μs $\cdot f_{ce} \sim 50$, where the electron gyrofrequency f_{ce} is evaluated with the average reconnection magnetic field.

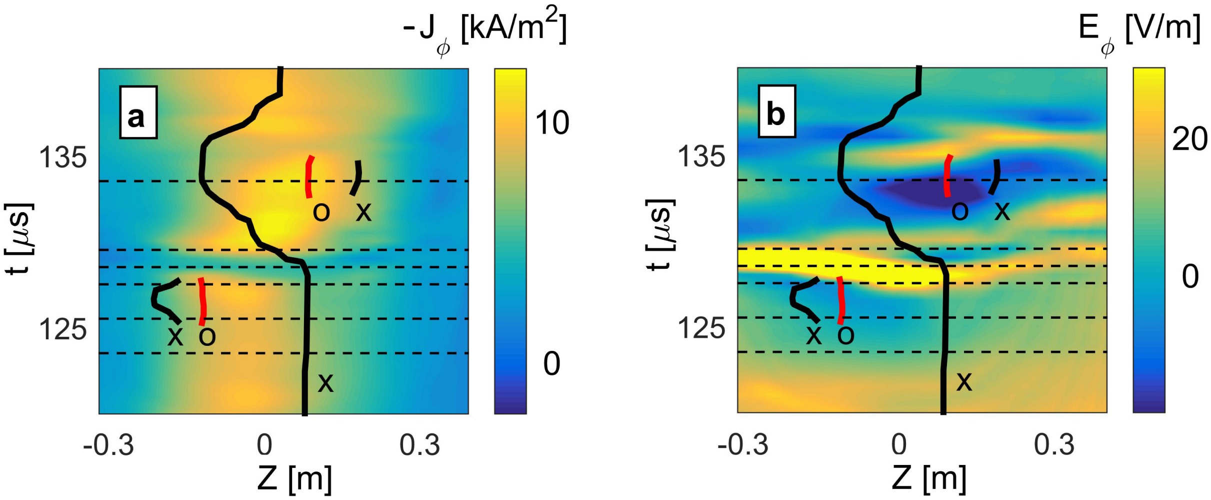

Figure 4.6: Time evolution of (a) J_ϕ and (b) the inductive electric field E_ϕ evaluated at the midplane as a function of Z and t. The dashed lines correspond to the midplanes from each frame of Fig. 4.5. The O and X-points are marked with red and black lines, respectively.

fall deeply into a regime of single X-line, collisionless reconnection, and yet the plasmoids are clearly present.

The observed island behavior shows explosive and dynamic modifications to the reconnection process. To provide an overview of how the island influences the reconnection process, Fig. 4.6 shows J_ϕ and E_ϕ evaluated on the evolving midplane. The locations of X-points along the midplane are shown as the solid black lines, while locations of O-points are marked as the solid red lines. The formation and ejection of magnetic islands are responsible for the strong variations in these profiles. First, as the islands grow and their currents increase, E_ϕ is reduced. Then, as the islands are ejected, large spikes in E_ϕ are observed. In fact, at $t = 128$ µs when the island is ejected and the current in the layer declines, the inductive E_ϕ spikes from 10 V/m to 50 V/m (saturating the applied color scale). The same pattern is observed again as the second island forms at later time. This dynamic nature when plasmoids are present is a key signature observed during all plasmoid events on TREX. Similar modification to the reconnection rate due to island dynamics has been observed in simulations [65] as well as previous experiments [75] and demonstrates their importance to the overall dynamics of the reconnection process. To standardize the analysis

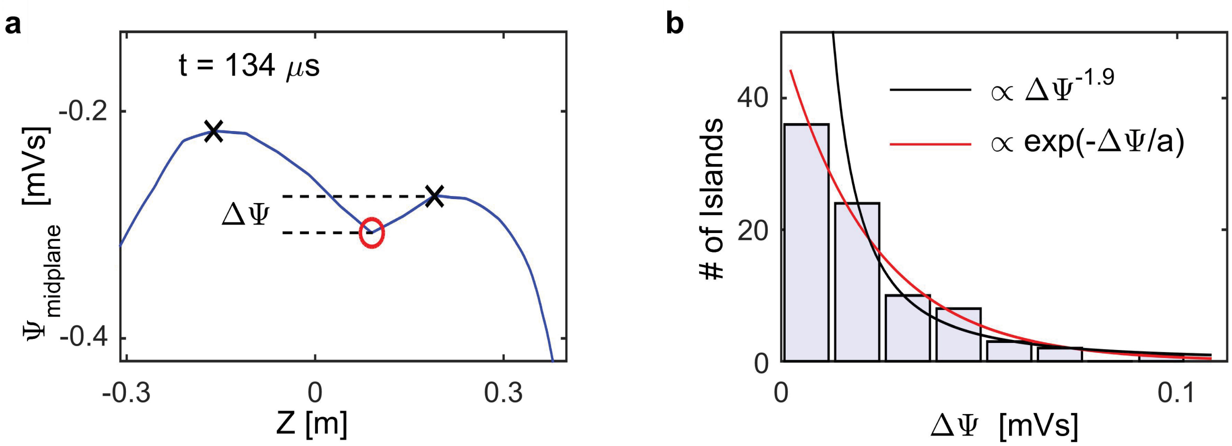

Figure 4.7: (a) Magnetic flux Ψ observed at the midplane for $t = 134$ µs. The X-points are located as local maxima, while O-points coincide with the local minimum. $\Delta\Psi$ provides a measure for the size of the islands. (b) Statistical study of the size of magnetic islands. Islands from 85 discharges are binned according to their size measured by $\Delta\Psi$ of panel (a). The data is consistent with both exponential and power-law dependencies for the island occurrence rate as a function of the island size.

over multiple discharges, the plasma parameters observed along the current layers are characterized, where $B_Z = 0$, for each time point. To illustrate this, Fig. 4.7(a) displays Ψ evaluated as a function of Z along the midplane observed at $t = 134$ µs. The two X-points observed in Fig. 4.5(f) are identified as the local maxima of the curve in Fig. 4.7(a). The center of the island is characterized by the local minimum in Fig. 4.7(b) (marked by the red "O"). The difference in the flux $\Delta\Psi$ between the O-point of an island and the nearest X-point provides a measure for the size of the island.

This experimental run consisted of 85 similar discharges with one or more magnetic islands observed in 42 of the discharges with a total of 81 islands counted overall. Using the technique described, smaller islands that may not be as obvious as those presented in Fig. 4.5 can still be accounted for. Figure 4.7(b) plots a histogram of the number of islands binned by $\Delta\Psi$. To investigate the statistical properties of the magnetic island occurrence, the size of the islands are analyzed for this ensemble of discharges. As indicated by the solid red line, the distribution of island sizes are well characterized by an exponential fit. However, due to the finite spatial resolution of the flux probe array, it is reasonable to expect that the smallest islands are not counted and therefore underrepresented. The solid black line then shows good agreement with a power law fit $\propto \Psi^{-1.9}$ if the first data point is excluded. It should be noted that this power law is very close to the flux distribution function predicted for the hierarchical plasmoid chains using extended MHD theory where $f(\Psi) \propto \Psi^{-2}$ [87]. However, this classic plasmoid instability is only expected for $S > 10^4$ and current layers $L_j \gg d_1$.

To summarize the results, the TREX plasmas are shown to operate in a low collisional regime for the experiments presented here. In this regime, electron scale magnetic islands are observed to be produced for current layers around one ion skin depth long, conflicting with the current understanding of plasmoid dynamics. Because magnetic islands are a fundamental ingredient in models for electron energization and increased reconnection dynamics, their high occurrence rate at these small scales suggest that magnetic islands may be seeded within larger systems, such as solar flares, much more effectively than suggested by present theoretical models.

Chapter 5

Upgrades to the TREX Hardware

While still a successful campaign, the earliest TREX experiments ended unceremoniously with the failure of certain internal components after extended exposure to the plasma. In particular, the outer insulation material (plasma-sprayed alumina coating) of the internal drive coils became permeable to the plasma over time, exposing the outer aluminum conductor and shorting out the plasma during a pulse. A picture of the aftermath post-removal of the coils is shown in Fig. 5.1 with the exposed metallic spots indicators of localized hot spots resulting in sputtering of the aluminum material below the insulating alumina. A thorough study of exactly how the alumina failed was not performed, but discussion with other plasma research groups found that the plasma spraying process does not create a solid surface, rather a microscopically porous one. With application of the heater current drive to the outer conductor, the large voltages can be shorted through the plasma, leading to arcing and hot spots that, once created, degrade over time. This failure began only after many TREX discharges and continuing experimentation following the completion of the campaign in Chapter 4. It is not thought to have had an effect on these prior results.

With the need for a new internal coil design came the opportunity to address other detriments that became apparent in the original experiment design. Namely, it was clear that the realized loop voltage at the coils was too low to achieve the necessary parameter regime for electron pressure anisotropy to develop. Thus, a significant redesign of the reconnection drive system, including the coils, transmission line, and capacitor bank was undertaken and constitutes a major component of the work for this dissertation. Details on the updated design to the drive system are discussed in Section 5.1. Additionally, Section 5.2 covers the new diagnostic suite that was designed and constructed to accommodate the faster time dynamics associated with the increased drive and to

Figure 5.1: An image of the alumina insulating material after the experimental campaign from Chapters 3 and 4. A support clamp held the coil where the alumina is brightest in color with the lighter discoloration coming from general plasma exposure. The metallic spots are sputtered aluminum, surrounded by what appears to be burnt alumina.

cover a larger area of the experimental apparatus. This chapter closely mirrors that of Chapter 3 but with significant improvements to each component noted below. These changes to the TREX configuration are used for the remainder of this dissertation and continue to be the foundation of current TREX research.

5.1 Reconnection Drive

5.1.1 Drive Circuit

A circuit diagram of the new reconnection drive system is shown in Fig. 5.2. The system consists of three primary components: the internal coils, the transmission line, and the capacitor bank, each of which are described in further detail below. The capacitors are configurable between 1 to 2 mF at up to 8 kV and are switched using a class D ignitron. The system is based off a standard RLC circuit with an underdamped response. However, with the addition of a flyback diode (up to 20 kV reverse voltage and 50 kA forward current), the current does not reverse through the coils

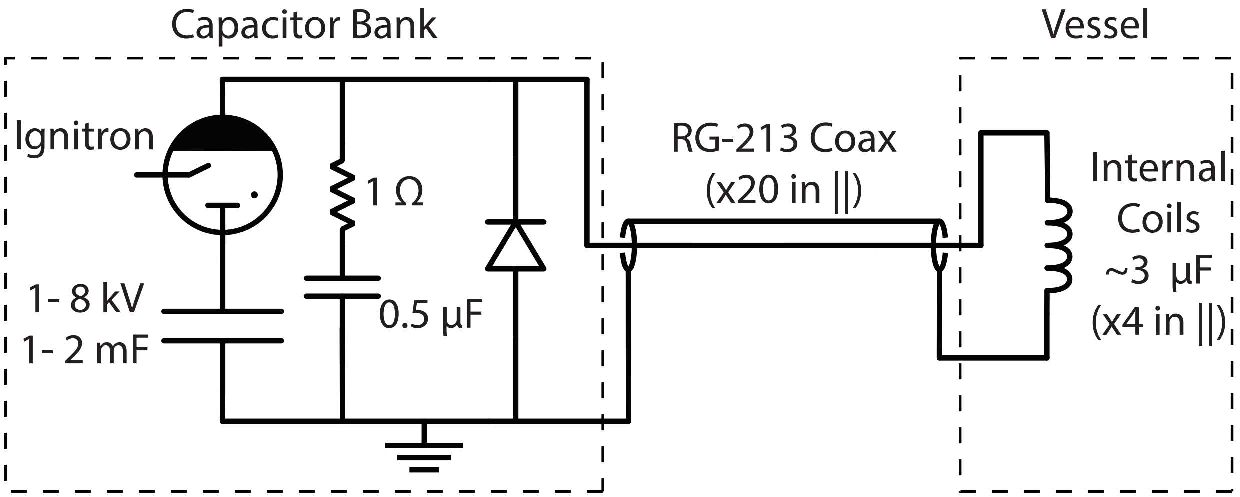

Figure 5.2: A schematic diagram of the reconnection drive circuit used on TREX. A flyback diode across the load keeps the current from reversing through the ignitron switch. A small snubber (resistor and capacitor) is used to limit the noise generated from the ignitron.

but rather decays away at some characteristic L/R timescale after the current pulse reaches its peak and the voltage across the capacitors reverses. In addition, an RC snubber across the load is used to help mitigate the switching noise caused by the ignitron. For the experiments presented, the capacitor bank is configured at 1 mF. A voltage and current pulse can be seen later in Fig. 6.2(c,d) showing the general behavior during an 8 kV discharge with a peak current through each coil of ~ 35 kA. Oscillations during the decay stage is thought to be caused by interaction with the snubber but does not interfere with the reconnection event. See Appendix C for more details on the charging and control schematics for the drive circuit.

5.1.2 New Coil Design and Construction

Creating a more robust reconnection drive coil was a primary goal for this redesign. The coils need to withstand exposure to the plasma and be rigid enough to handle the magnetic forces present when pulsed with large currents. To this end, the conductor was replaced with hard drawn copper pipe (0.675 in. OD, 1/8 in. wall thickness) which is much heavier and more rigid than the aluminum tubing used for the old coils. Rigid PTFE (Teflon) tubing (1 in. OD, 5/32 in. wall

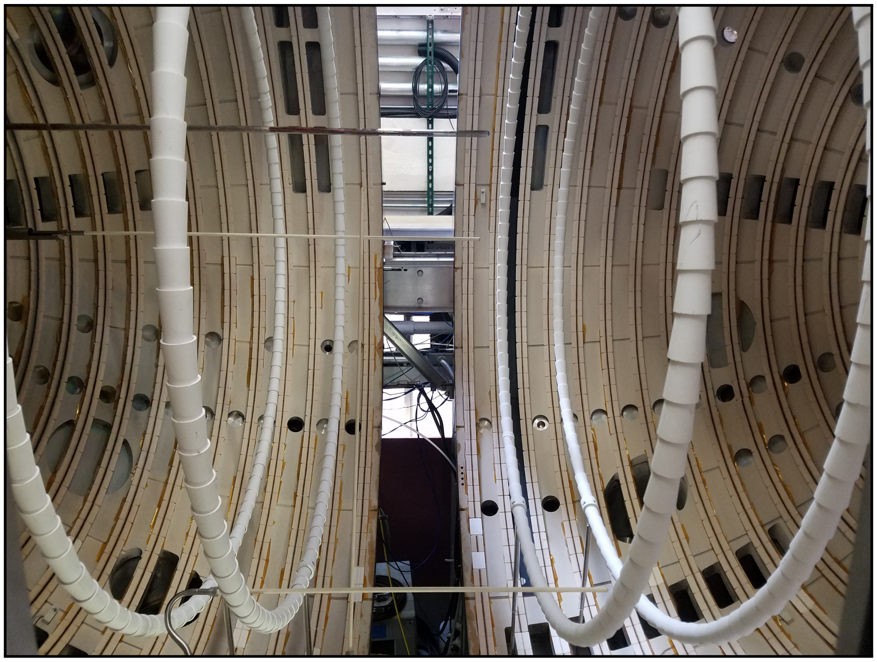

Figure 5.3: A picture after installing the TREX hardware into the BRB. The four reconnection drive coils are surrounded by ~ 90 alumina cones to protect the teflon insulation from the plasma.

thickness) surrounds the copper conductor for electrical isolation. PTFE is an extremely good insulator and tubing of this thickness easily surpasses the 35 kV limit of the hi-pot testers on hand. While PTFE also has very low outgassing in vacuum and performs well even in low temperature plasma conditions, leaving this much surface area exposed to the plasma is not ideal. To combat this, ~ 90 open-ended cones made of alumina cover the PTFE, interlocking around the entire circumference of the 92 cm radius coil. A machined aluminum clamp holds the coils in place at the bend for the leads. A picture of the four coils installed in the BRB during a TREX changeover is shown in Fig. 5.3. The coils rest on stainless steel rods (surrounded by quartz glass tube) and are held in place at the vacuum feedthrough.

The design of these coils is relatively simple and in principle, the construction is, as well, with the only constraint being the size and shape of the materials. The process for constructing one of the coils is outlined in Fig. 5.4. The copper pipe is only available in limited lengths, so two straight pipes are formed into half-circles using a tube bender, ensuring that one end is kept straight for

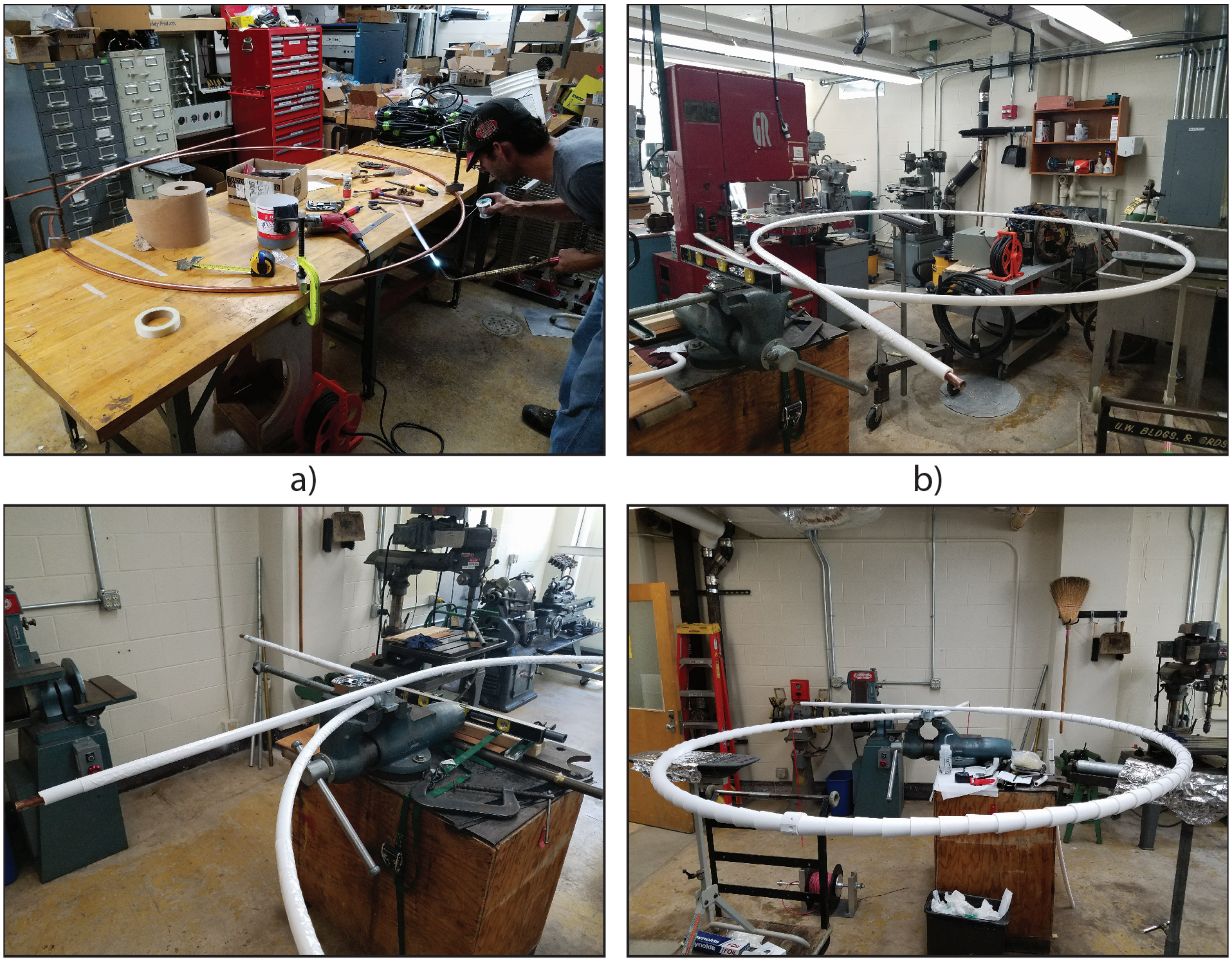

a) b) c) d)

Figure 5.4: Pictures of the construction of the reconnection drive coils. The images show different stages of the process: (a) brazing two bent copper conductors into one loop, (b) installing the teflon tubing for electrical insulation, (c) bending one of the leads, (d) installing the alumina cones for plasma shielding.

the electrical and vacuum leads. The two halves are then brazed together to form a complete coil as shown in Fig. 5.4(a). After installing the PTFE tubing over the copper conductor (Fig. 5.4(b)), the first lead can be bent to its final angle (Fig. 5.4(c)). Note that unlike the old coil design, the leads are not normal to the circular coil since the boxports in which the leads exit the vessel are not aligned with the central axis. Finally, Fig. 5.4(d) shows the installation of the interlocking cones surrounding the PTFE tubing prior to bending the second lead and clamping the assembly in place. This process was done for all four coils with very good repeatability.

5.1.3 Transmission Line

As mentioned previously, the main constraint to the original reconnection drive circuit discussed in Section 3.1 was the limitation of the realized loop voltage at the coil leads. This was largely in part due to the use of twisted pair cable for the transmission line from the capacitor bank to the coils. Given the interwire spacing s and wire diameter d, the inductance per unit length for twisted pair cable is

$$l_{twisted} = \frac{\mu_0}{\pi} \ln\left(\frac{2s}{d}\right) . \tag{5.1}$$

Consequently, over the length of ~ 50 ft, the total inductance of the cable is $L_{twisted} \approx 14$ μH where $s \approx 19$ mm and $d \approx 4$ mm are used for the cable dimensions. Thus, the twisted pair cable accounts for $\sim 75\%$ of the total inductance of the circuit, $L_{tot} \approx 20$ μH, and therefore represents a significant loss in voltage between the capacitors and the coils, not accounting for other losses internal to the capacitor bank or through the parallel leads of the drive coils themselves. To reduce the inductive losses of the transmission line, the twisted pair cable was replaced with 20 RG-213 coaxial cables in parallel. The nominal inductance per unit length of this cable is $l_{coax} = 77$ nH/ft, which gives a total inductance of $L_{coax} \approx 0.2$ μH over the 50 ft long cable bundle.

5.1.4 Capacitor Bank

The newly designed capacitor bank also addresses the voltage limitations of the old design. A picture of the capacitor bank fully assembled is shown in Fig. 5.5(a) with the transmission line cables traveling up through a pipe connecting the main lab space to the capacitor room and to the coils in the vessel. The assembly is enclosed in an insulating box made of phenolic and acrylic sheets for safety. To better understand the design and functionality, Fig. 5.5(c) shows an exploded view of the assembly from a 3D cad model. Two sets of three 330 µF capacitors sit on either side of the central ignitron. The ground terminals are connected through a 3/8 in. plate of aluminum with passthroughs for the high voltage connections large enough to keep an insulating air gap. A similar aluminum plate sits atop the the ground plate, securely clamped to each capacitor's high voltage terminal through a small aluminum spacer. The ground and high voltage plates are kept isolated by two sheets of thin insulating DMD paper (fibrous polyester paper with excellent dielectric properties).

The high voltage plane attaches directly to the anode of the ignitron where positive current flows through the ignitron to its outside body (cathode) where it is then distributed to the internal conductors of the 20 coaxial cables and out to the drive coils. The outer shield of the cables, the return path for the current, then attaches to the ground plane with two aluminum clamps that additionally hold the two sets of capacitors in place. A closer look at the cable and ignitron connections can be seen in Fig. 5.5(b), passing through the high voltage and ground planes. The proximity of the two planes limits the magnetized volume between them, minimizing the inductance in this configuration. Keeping the coaxial structure of the ignitron and transmission line also helps reduce inductive losses.

A special design element of this capacitor bank is the ability to easily disconnect up to three capacitors and therefore tune the capacitance of the drive circuit within the allowed range. This is accomplished by removing the spacer that links the top plate to the high voltage terminal and replacing it with a machined plastic cap, ensuring the capacitor remains isolated from the rest of the bank.

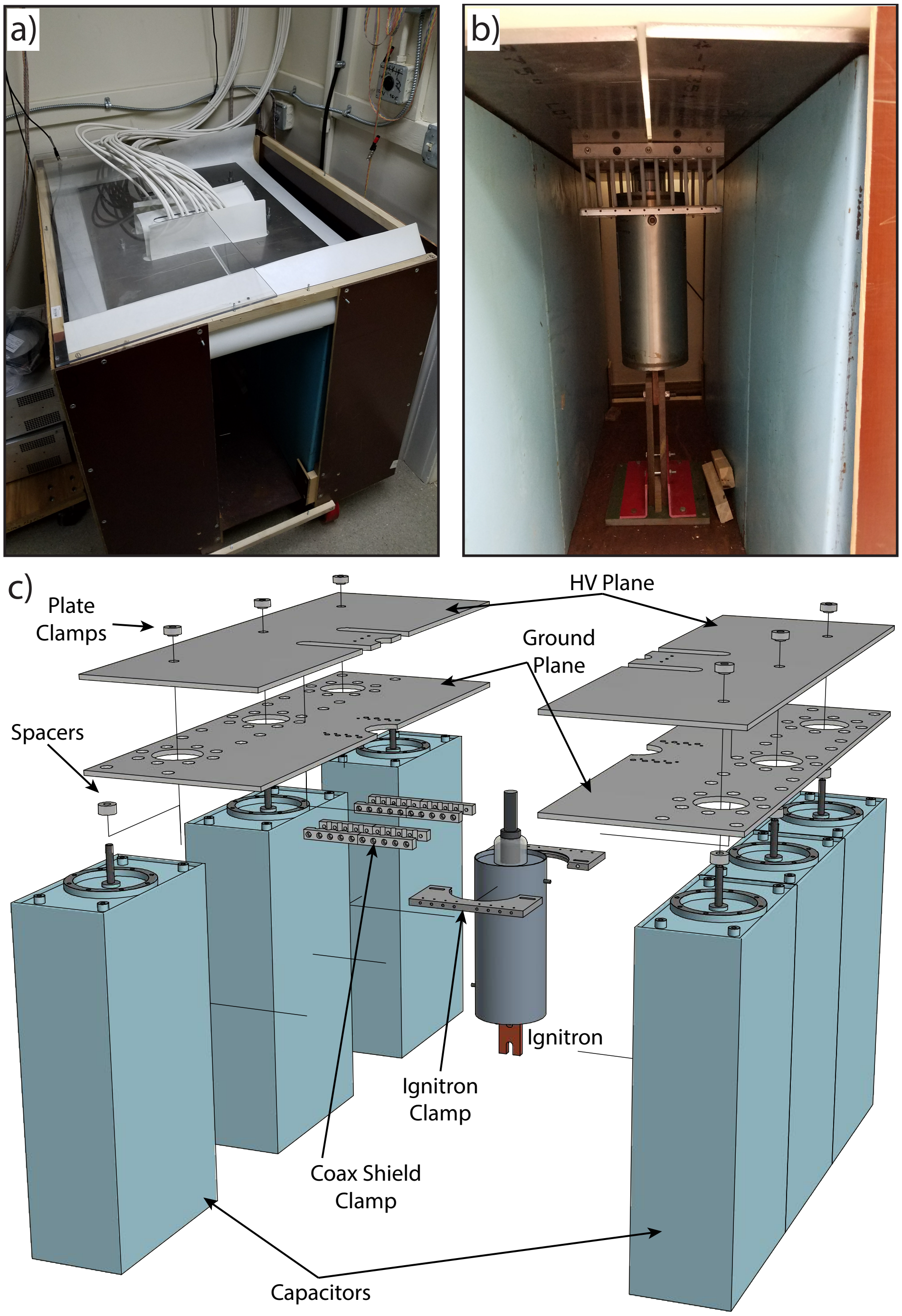

Figure 5.5: (a) Exploded view of the reconnection drive capacitor bank assembly (from 3D cad model). (b) Image of the capacitor bank *in situ*. (c) Image of the high voltage ignitron used to switch the large currents for driving reconnection.

5.2 Diagnostics

5.2.1 $\dot{\mathrm{B}}$ Probe Arrays

The $\dot{B}$ probes described here are functionally similar to those in Section 3.2.2 but optimized for use with the upgraded TREX hardware. Each probe consists of 3 orthogonal coils. However, each coil is made up of two oppositely directed coil windings measured independently. This is similar to the setup shown in Fig. 3.7 in which the differential signals are combined and the common mode noise is subtracted away. Unlike before, each coil is terminated with a 100 Ω resistor next to the probe reducing the effect of the internal capacitance of the windings such that the probe response is dominated by the coil inductance and parallel resistor. With twisted pair cables (which the remaining coil leads consist of) having a nominal impedance of $\sim 100\ \Omega$ typically, then the resistor size is also impedance matched to reduce transmission line effects.

The coils are made of 0.003 in. enameled magnetic wire (purchased pre-twisted) and wound around a custom designed 3D printed form with grooves for the wires. A picture of the hand wound probes is shown in Fig. 5.6 during assembly of one of the probe arrays. The forms are cylindrically shaped (3.5 mm diameter and 17 mm long) such that the coil along the probe axis (local z direction) is smaller than the two transverse coils (local x and y directions) but are wound with different number of turns to make the effective probe area comparable. The probe forms also interface directly with 3D printed spacers to achieve a consistent length between the probes in an

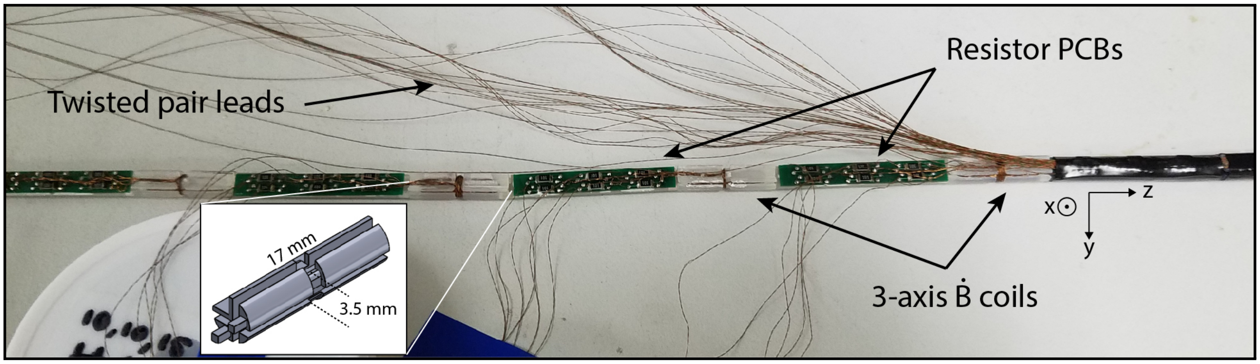

Figure 5.6: Image during assembly of one of the 3-axis $\dot{B}$ probe arrays. Each coil winding is terminated by an SMD resistor on the green printed circuit boards between the individual probes.

array. Printed circuit boards with surface mount resistors are epoxied directly to the spacers with convenient pads to directly solder the incoming coil wires and outgoing twisted pair leads.

In general, the signal output of a $\dot{B}$ coil acts as a high-pass filter in which $V_{\text{probe}} \propto \dot{B}$ is only true for signals slower than the natural L/R timescale of the circuit. Above this limit and the probe response becomes independent of frequency. Given the sampling frequency of the TREX digitizers, the number of turns for each probe is optimized such that the frequency rollover of the probe is above the digitization Nyquist frequency F_N and the measured signal is given by Eq. 3.1 over the full range of sampling frequencies. Because the TREX digitizers progressively lose usable channels with increased sampling frequency, there are two sets of $\dot{B}$ probes used in these arrays: fast and slow probes; the only difference being the number of turns in each coil. The fast probes consist of 3 turns in the x and y directions and 5 turns in z and are digitized at 10 MHz whereas the slow probes have 10 and 15 turns and are digitized at 2 MHz to allow for more probes to be used in an array.

Using a small single turn Helmholtz coil connected to a function generator to drive a rapidly varying magnetic field and measuring the output of a probe through an oscilloscope can be used to determine the exact frequency response of the probes. An example is shown in Fig. 5.7(a) for a 3/5 turn fast $\dot{B}$ probe. Here, the output gain of the probe is proportional to $\dot{B}$, as indicated by the straight line in the log-log scale, and remains until the frequency exceeds the 5 MHz Nyquist limit of the digitizers. For many of the probes in an array, the leads are 3 m in length inside the probe shaft plus the length that goes from the probe to the digitizer. These leads have a large parallel capacitance which then resonates with the coil inductance at ~ 10 MHz, resulting in an increase in the impedance and a sharp decline in the voltage output, apparent in both probe directions. Figure 5.7(b) expands on this detail by comparing the same 5 turn coil response with different external cable lengths. As the length, and therefore capacitance, is increased from 1 m to 2 m, the resonant frequency drops, showing the importance of keeping the digitizers as close to probes as possible to minimize the total cable length.

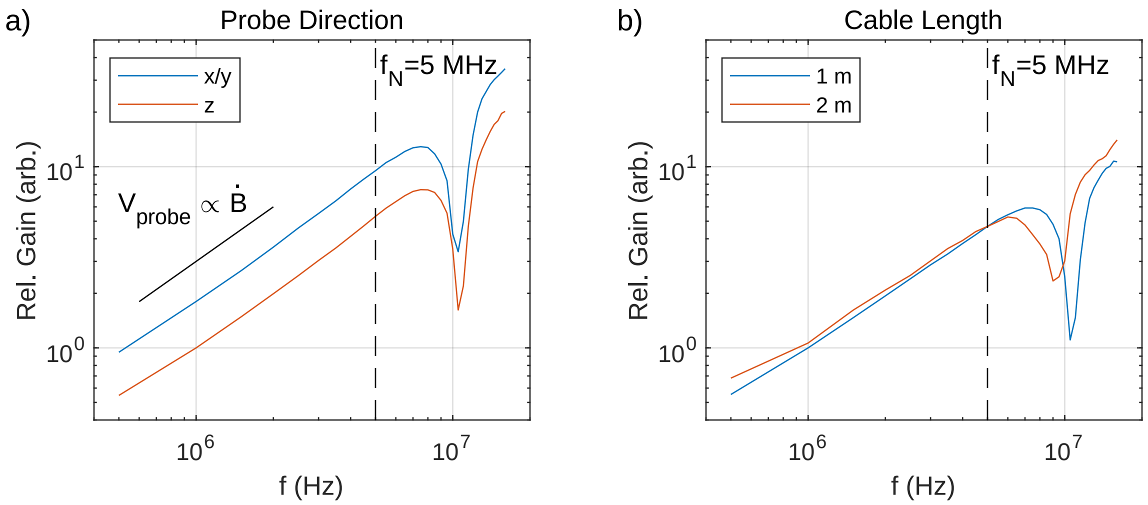

Figure 5.7: (a) The frequency response of the gain for a fast $\dot{B}$ probe. The gain is normalized to the output of the Z direction at 1 MHz. (b) Frequency response of the Z direction probe for different lengths of cable outside the 3 m probe shaft. As the leads increase in length, the resonance in the cable shifts to lower frequencies.

The following are descriptions of three linear arrays in use for the TREX experiments utilizing the $\dot{B}$ probes detailed above. The scale of the three $\dot{B}$ probe arrays relative to the full TREX configuration is also shown in Fig. 5.9 with extensive discussion of their usage covered in Chapter 6.

1. **Linear Probe:** The linear probe measures over 98 cm with the use of 14 3-axis $\dot{B}$ coils. The central 60 cm of the array alternates between six slow probes and 5 fast probes with 6 cm spacing. Each side then extends with two more slow probes with 9.5 cm spacing. The array sits inside an alumina tube and is attached to a stainless steel shaft for a total assembled length of $\sim$ 3 m, allowing for extended reach and coverage area inside the vessel. The linear probe enters the vessel through a boxport at $R = 40$ cm aligned with the Z-axis and can be scanned along Z.

2. **Hook Probe:** The hook probe consists of 14 3-axis $\dot{B}$ probes, alternating between slow and fast probes with 6 cm spacing for a total coverage of 78 cm. Visible in Fig. 5.9, the probe gets its name from the 90° turn in the stainless steel shaft before connecting to the alumina

tube around the probes, allowing the array to be aligned with the Z-axis. Entering the vessel at $Z = -25$ cm, the probe can be moved to different radial locations from $R = 0$ cm to $R = 90$ cm and can reach from $Z = -95$cm to $Z = 45$ cm by rotating the probe about its shaft by 180°.

3. **Speed Probe:** The speed probe is a stationary probe array at $Z = 0$ cm (the equator) spanning from $R = 0$ cm to $R = 90$ cm and made of 16 single-axis $\dot{B}$ coils with 6 cm spacing. The single-axis coils are aligned with Z to measure the axial field.

All three probe assemblies are hermetically sealed from the vacuum inside the vessel and do not require feedthroughs for the probe leads. With no need for an outer garage assembly, this allows for the maximum extension of the probes inside the vessel but eliminates the ability to install the probes while the vessel is under vacuum. This is only a minor issue as in the case of the hook probe, due to its geometry, a vacuum break is already required for installation.

5.2.2 $\mathrm{T_e}$ Probe

As in the previous experiments and covered in Section 3.2.4, a T_e probe is used for the following experiments to gather plasma density and temperature data. Under certain conditions, the old design shown in Fig. 3.10 suffers from shadowing effects in which the probe tips become shielded by the rest of the probe body. To alleviate this problem, the new design attempts to reduce the overall proportions of the probe head and to extend the Langmuir probe tips away from the main body. The body is 3D printed in two interlocking halves with holes for eight 1/16 in. diameter molybdenum probe tips on each side. The probe tips are press fit into the mounting holes in the body, making contact with an exposed signal wire in the hole. Typically, molybdenum is difficult to make an electrical connection to, but this press fit connection has proven to be a very relilable and could be used in many probe designs utilizing molybdenum electrodes. Short lengths of PTFE tubing cover the base of the electrodes to limit the collection area towards the tips and away from the body of the probe. A $\dot{B}$ coil extends past the probe body to limit pickup from the Langmuiir probe currents and allows for accurate timing of the T_e probe signals relative to the

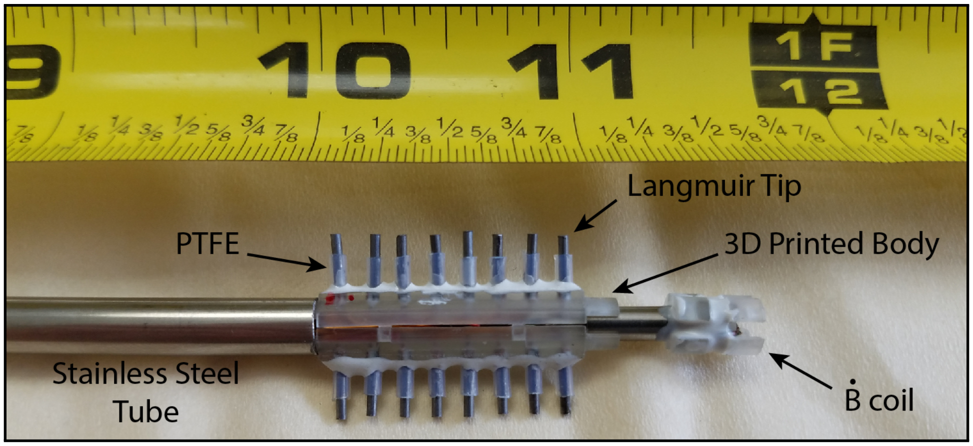

Figure 5.8: Picture of the upgraded T_e probe constructed for TREX experiments.

reconnection magnetic fields. A small stainless steel tube attaches the probe head assembly to the rest of the probe shaft. As shown in Fig. 5.9, the T_e probe is inserted at $R = 40$ cm through the boxport opposite the linear probe, but is transferable to any location through the proper gate valve. The same circuit hardware and measurement technique discussed in Section 3.2.4 is used here with sense resistors and divider resistors optimized for the plasma parameters observed in the new TREX configuration.

5.3 New configuration

Using the upgraded components discussed in this chapter, a 3D CAD model of the full TREX configuration is shown in Fig. 5.9. The individual diagnostics are highlighted to show their position relative to the internal drive coils. The directions of the initial Helmholtz and drive coil fields are opposite those used in Chapter 4. This is the preferred orientation on TREX with the chosen coordinate system but can be easily reversed as needed. In addition, the array of plasma guns discussed in Section 2.3.2 are used for plasma generation instead of the $\mathrm{LaB_6}$ cathodes. These create a more uniform and steady plasma that fills the vacuum chamber and removes the need for the preceding heater pulses. As a consequence of this change, the background plasma temperature and density is naturally lower from the plasma guns ($T_e \sim 4$ eV and $n_e \lesssim 10^{18}$ m^{-3}) compared to the cathodes plus heater pulses ($T_e \sim 10$ eV and $n_e \gtrsim 10^{18}$ m^{-3}).

For the experiments covered in Chapter 6, only three coils are used to drive magnetic reconnection instead of the four possible. In early studies with the upgraded hardware, it was found that a stable magnetic island formed between the two innermost coils with a current layer on either side. This entire structure of two X-points and an O-point was then driven toward the central axis, similar to previous experiments. At this time, it is thought that the island is a result of the forced geometry from the drive coils. Removing one end coil was determined to break the symmetry and allow for a single, steady reconnection current layer to form. The addition of a toroidal field also proved to prevent the island from forming.

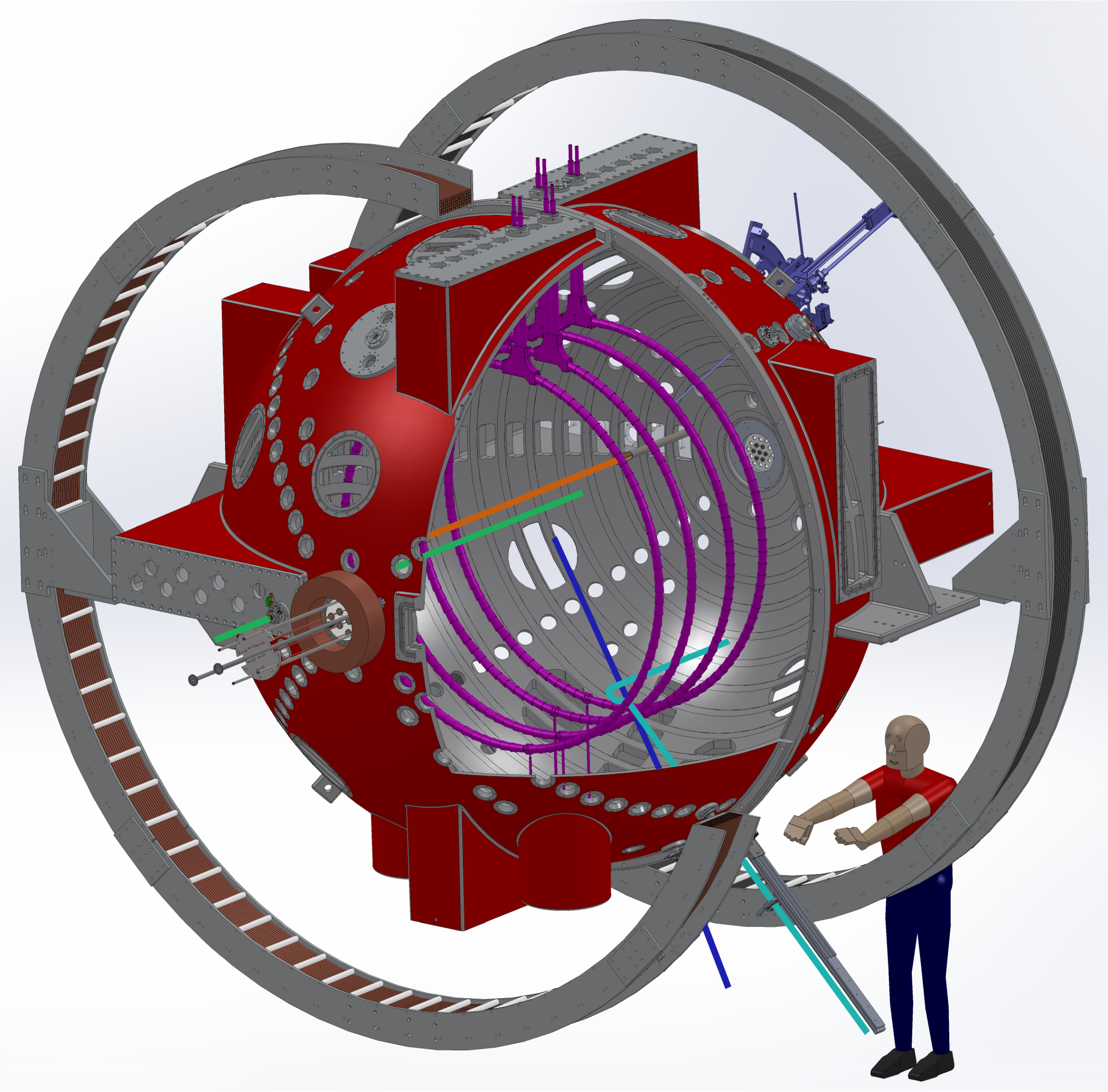

Figure 5.9: A 3D CAD rendering of the TREX configuration for the experiments in Chapter 6. The four 0.92 m reconnection drive coils (purple) enter/exit the vessel through the top boxports. The diagnostic suite includes the linear probe (green), speed probe (blue), hook probe (light blue), and T_e probe (orange).

Chapter 6

Regulation of the Normalized Rate of Driven Magnetic Reconnection through Shocked Flux Pileup

The following chapter focuses on reconnection experiments following the upgrades discussed in Chapter 5 in which the absolute rate of reconnection is set by the external drive. A shock interface between the supersonically driven plasma inflow and a region of magnetic flux pileup permits the normalized rate of reconnection to self-regulate to a fixed value. The observations demonstrate the role of shock formation in driven reconnection and confirm previous theoretical results on the normalized rate of reconnection.

6.1 Background

Magnetic reconnection is a fundamental process in plasma systems which allows for the magnetic topology to change rapidly, converting stored magnetic energy into plasma energy [27]. While reconnection occurs in a localized diffusion region [9], it often leads to dramatic changes in the macroscopic behavior of a variety of systems including solar flares [5], the Earth's magnetosphere [7], and magnetic fusion experiments [88].

In reconnection models the upstream magnetic field B_{rec} is important because its tension sets the acceleration of the reconnection exhaust, yielding an outflow speed $v_{\text{out}} \simeq v_A$, where $v_A = B_{\text{rec}}/\sqrt{\mu_0 n_i m_i}$ is the Alfvén speed [4]. Furthermore, in fast reconnection not only the outflow speed but also the inflow speed (in the frame of the reconneciton layer) is Alfvénic [28]. The normalized reconnection rate $\alpha = v_{\text{in}}/v_{\text{out}}$ has been studied through numerical simulations with typical values of $\mathcal{O}(0.1)$ [89] but have been shown to be weakly dependent on system size [90, 91]. By Faraday's law, the absolute rate is characterized by the inductive electric field $E_{\text{rec}} = v_{\text{in}} B_{\text{rec}}$ [92] and is typically influenced by conditions external to the reconnection region [93, 94]. Nevertheless, it is expected from theory that the reconnection dynamics regulate the current in the reconnection layer such that α remains fixed [29].

The dynamical interplay between shocks and reconnection has many applications to both astrophysical and space plasmas but has only recently been studied in more depth [95, 96]. For some driven reconnection scenarios, prevalent when stellar winds interact with planetary magnetospheres, a process called magnetic flux pileup regulates the upstream magnetic field B_{rec} such that the ratio of the forced inflow speed and the outflow speed is consistent with the normalized rate [97]. Examples include the transition from the supersonic solar wind which is compressed at the Earth's bow shock to the magnetosheath upstream of reconnection sites in the dayside magnetopause [98, 99, 100].

Despite its importance, experimental studies of flux pileup and the role of shock formation are still limited. At dominant plasma pressure, $\beta = nT/(B^2/2\mu_0) \gg 1$, flux pileup has been inferred during the collision of laser produced plasma bubbles [14] in qualitative agreement with numerical models [101], as well as in Z-pinch experiments driven by exploding wire arrays [102]. For both scenarios, the strong drive yields transient fast reconnection at relatively high Lundquist numbers $S = \mu_0 L v_A / \eta \simeq 10^3$, where η is the electrical resistivity and L is the system size. Meanwhile, for $\beta < 1$ pileup has only been demonstrated during slower Sweet-Parker-like reconnection [4] between coalescing flux ropes with $S \simeq 30$ [103]. For all cases above, no shock formation was reported though it likely plays a role in the observed flux pileup.

In the following, a quantitative experimental study of magnetic flux pileup and the normalized reconnection rate on TREX is provided. The drive is applied from only one inflow, causing the reconnection layer to move super-Alfvénically into the opposing inflow and providing a unique setup that permits the study of magnetic pileup and the associated shock formation under collisionless conditions, $S \sim 10^3$–10^4, where the plasma dynamics are dominated by the magnetic field pressure, $\beta \simeq 0.1$. Furthermore, the large reconnection layer size (half-length of $L \simeq 0.8$ m) facilitates direct probing by simple electrostatic and magnetic diagnostics. Super-Alfvénic plasma flows and shock formation are common in heliospheric and astrophysical settings, and the TREX configuration enables the first detailed experimental demonstration of the role of shocked flux pileup in regulating a steady normalized rate during supersonically driven magnetic reconnection.

6.2 Experimental Configuration

The experimental setup is shown in Fig. 6.1, outlining the coordinate system used in the following analysis and the location of the drive coils and diagnostics discussed in Chapter 5. For this set of experiments, the reconnection drive is configured to use three of the four internal coils. A representative discharge is presented in Fig. 6.2 showing the broader timing involved for a single event. At $t = 0$ ms a gas puff is sent to the array of six pulsed plasma guns [56] with a steady state, axial magnetic field Helmholtz coil in the positive Z direction. 12 ms later, the plasma gun arc is triggered, generating a 10 ms pulse of plasma as indicated by the steady $I_{\text{arc}} \simeq 1$ kA through each plasma gun in Fig. 6.2(b). At $t = 18$ ms, the 0.92 m reconnection drive coils, located at $Z = \pm 0.15$ m and 0.40 m, are pulsed opposite the Helmholtz field. As the current rapidly increases, new magnetic flux is injected by the coils such that a reconnection current layer forms and is driven towards the central axis. Fig. 6.1(8) shows a 2D profile of the resulting toroidal Hall magnetic fields and poloidal field lines for the specific configuration presented later in Fig. 6.7. As shown in Fig. 6.2(e,f), the duration of a reconnection event occurs over only the first < 100 μs of the current pulse. While the exact parameters used in following experiments will differ, the general structure of the event presented holds for all TREX shots.

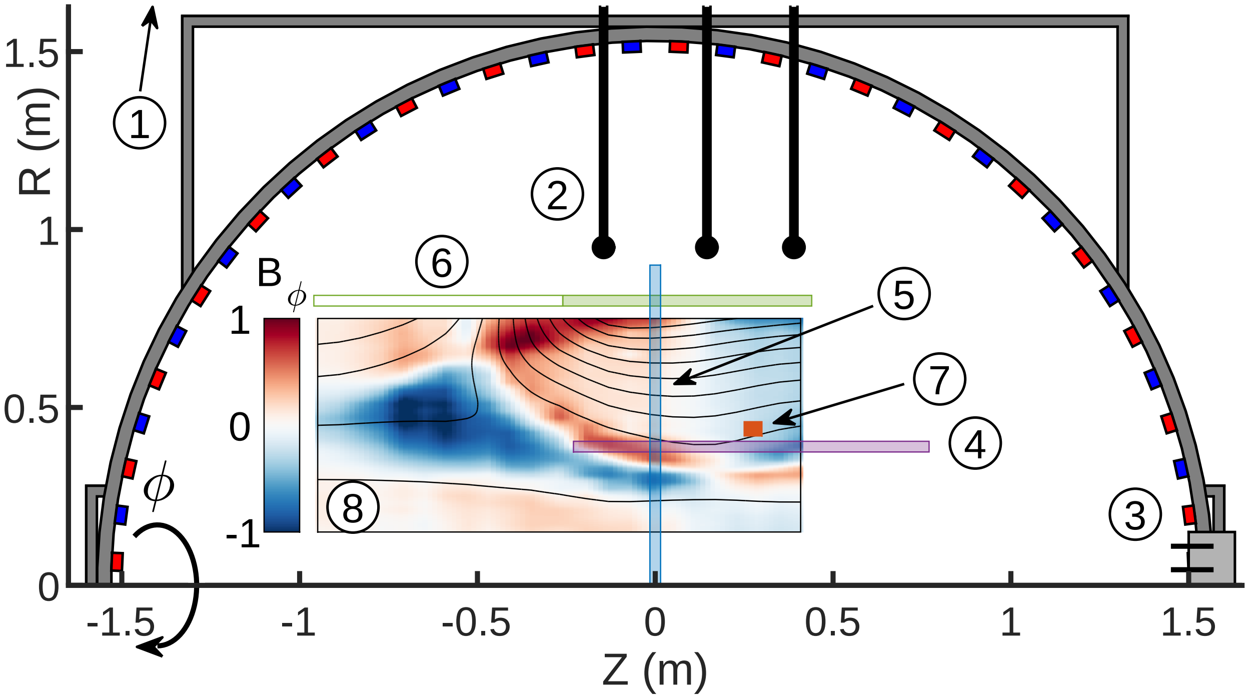

Figure 6.1: The TREX configuration consists of (1) the external Helmholtz coil (at $R = 2$ m), (2) the internal reconnection drive coils, and (3) the plasma gun array added to the 3 m spherical vacuum vessel. The diagnostics consist of three linear $\dot{B}$ arrays, (4) the linear probe, (5) the speed probe, and (6) the hook probe, as well as the localized T_e probe (7). The colored segments indicate each probe's spatial extent. (6) and (7) are toroidally offset from (4) by 145° and 18°, respectively. (8) An example 2D profile of the toroidal Hall magnetic fields as measured by probe (6).

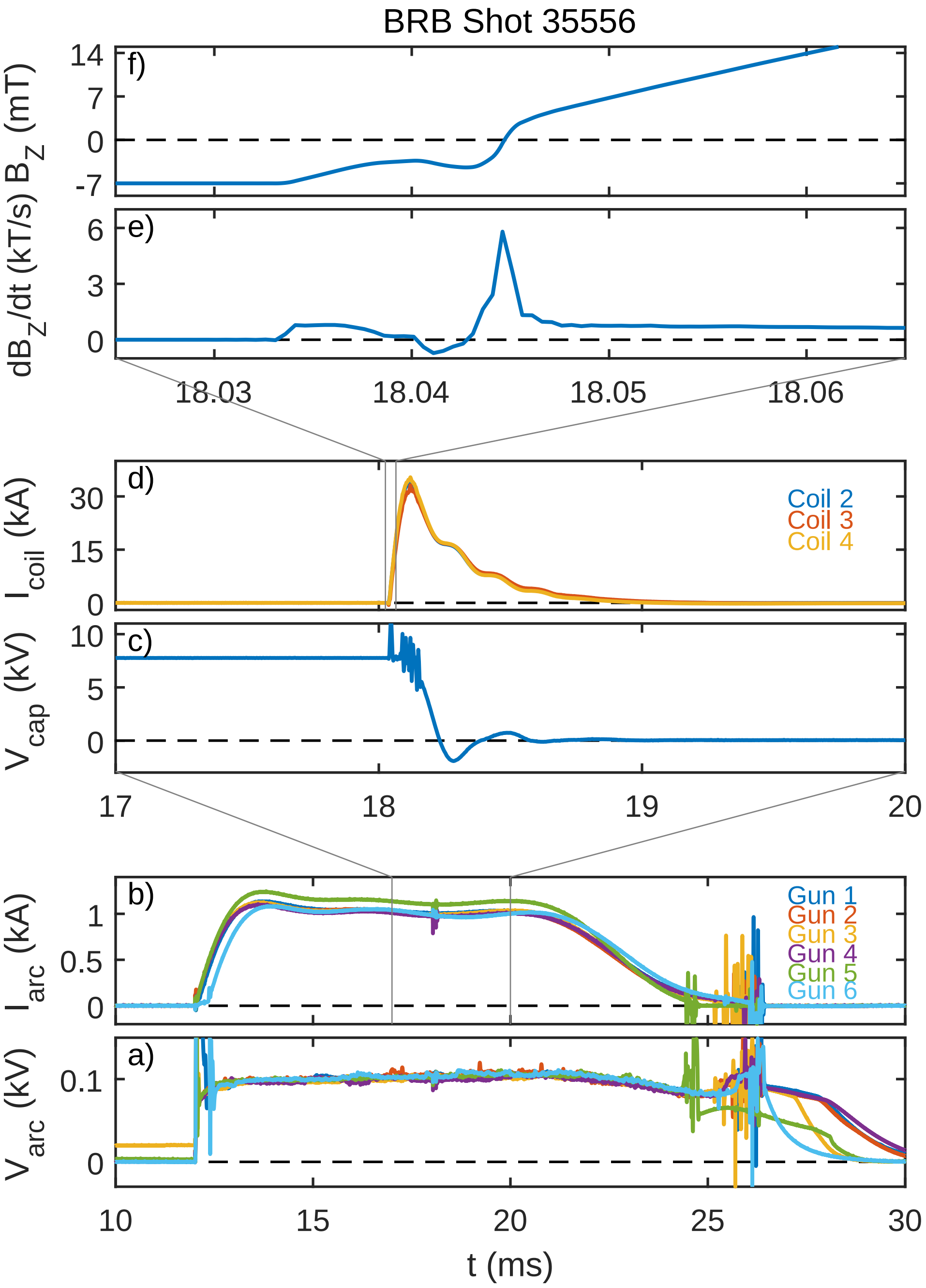

Figure 6.2: Traces of plasma gun current (a) and voltage (b), drive capacitor voltage (c), and drive coil currents (d) for a hydrogen discharge with $V_{\text{drive}} = 8$ kV and $B_H = 7$ mT using 3 drive coils (Coil 1 disconnected). (e,f) Magnetic traces of $\partial B_Z/\partial t$ and B_Z from the linear probe at $R = 0.4$ m. The reconnection event is only a small portion of the overall plasma discharge.

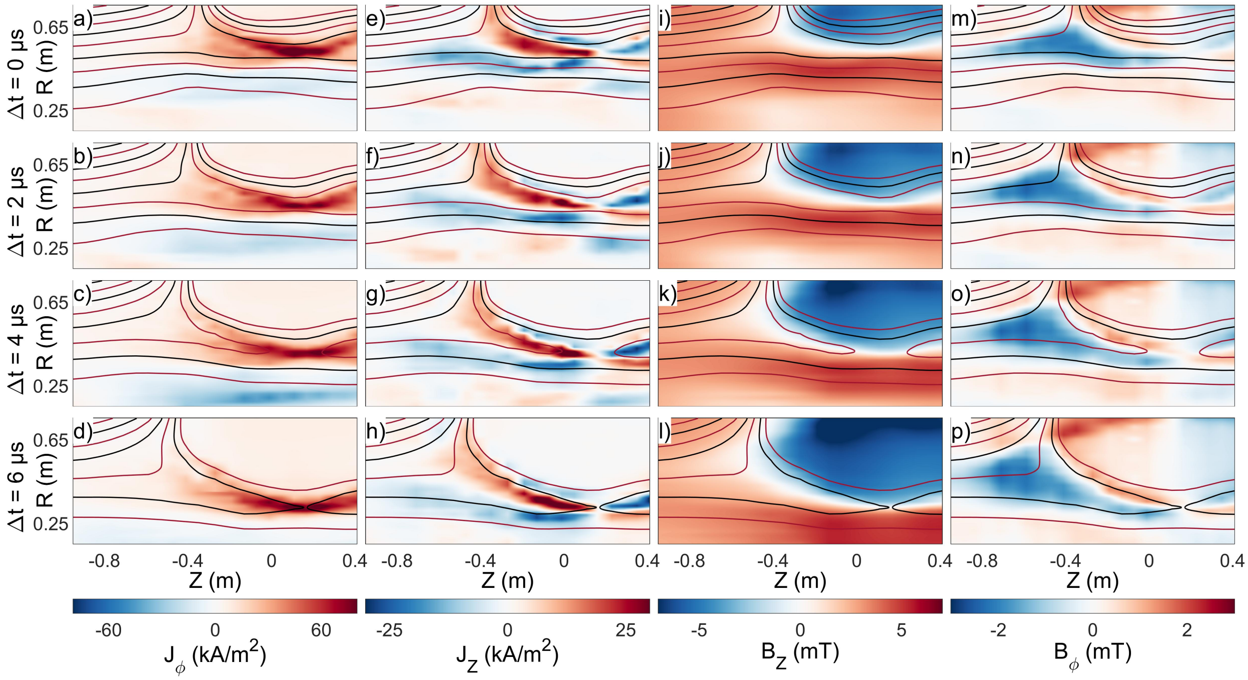

Figure 6.3: Profiles of (a-d) the toroidal current density J_ϕ, (e-h) the poloidal current density J_Z, (i-l) the reconnecting magnetic field B_Z, and (m-p) the toroidal Hall magnetic field B_ϕ at different times during a shot in H_2 with $B_H = 5$ mT and $V_{\text{drive}} = 5$ kV. The current layer geometry remains roughly constant while propagating from $R = 0.55$ m to $R = 0.31$ m.

6.3 Reconnection Geometry

The reconnection dynamics driven in the TREX configuration are highly reproducible. Reconnection is induced by energizing the three internal coils of radius ~ 0.92 m to inject magnetic flux opposing a background magnetic field generated by a set of external Helmholtz coils. The evolution of the resulting magnetic configuration is characterized by scanning the hook probe (Fig. 6.1(6)) to different radial positions over ∼50 reproducible discharges with the same experimental settings. Figure 6.3 shows profiles of the reconnection geometry acquired for a typical TREX configuration where reconnection was driven in Hydrogen gas (H_2) with a drive voltage of $V_{\text{drive}} = 5$ kV and Helmholtz field of $B_H = 5$ mT. At the time of the first row of sub-figures, the reconnection geometry is already established. As time increases from top to bottom, the reconnection layer of high toroidal current density J_ϕ propagates from $R = 0.55$ m to $R = 0.31$ m at $v_{\text{layer}} \simeq 40$ km/s. This current layer separates the two reconnection inflows with reversed axial magnetic field B_Z shown in Fig. 6.3(i-l). Particularly, at $\Delta t = 4$ μs in Fig. 6.3(c), a blue ribbon of negative J_ϕ current is observed at $R \simeq 0.23$ m corresponding to the shock formation and magnetic pileup described later in the chapter. Meanwhile, the in-plane current J_Z gives rise to the toroidal Hall magnetic field B_ϕ.

The overlaid field lines are contours of constant magnetic flux, coinciding with the magnetic field lines. All panels consider the same set of contour levels such that the motion of the field lines can be followed in time. Within the two inflow regions, the field lines are all observed to move downwards, with those above the reconnection layer moving faster than the layer and those below the layer moving slower than the layer. In the frame of the reconnection layer, field lines are therefore moving together at a rate that is constant in time (see analysis below). While the length of the reconnection exhaust does increase slightly in time, the structure of the inner part of the reconnection region is steady as it translates to lower values of R.

6.4 Calculating $\mathbf{E}_{\mathbf{rec}}$

The speed probe (Fig. 6.1(5)) provides data critical to evaluate the speeds for the shock and reconnection layers. In addition, the analysis of the speed probe data provides detailed information on the temporal evolution of the inductive electric field as the reconnection layer transits the radial cross section.

The magnetic pickup loops comprising the speed probe are arranged to measure $\partial B_Z/\partial t$ along a vertical chord at $Z = 0$ m. An example of $\partial B_z/\partial t(t, R)$ acquired in a single shot is shown in Fig. 6.4(a). According to Ampere's law we have $\mu_0 J_\phi = \partial B_R/\partial Z - \partial B_Z/\partial R$. Because of the elongated shock and reconnection geometry observed in Fig. 6.3 it is clear that, in general, $|\partial B_Z/\partial R| \gg |\partial B_R/\partial Z|$. It then follows that

$$\mu_0 J_\phi \simeq -\frac{\partial B_Z}{\partial R} \simeq -\frac{1}{v_{\text{layer}}}\frac{\partial B_Z}{\partial t}\,. \tag{6.1}$$

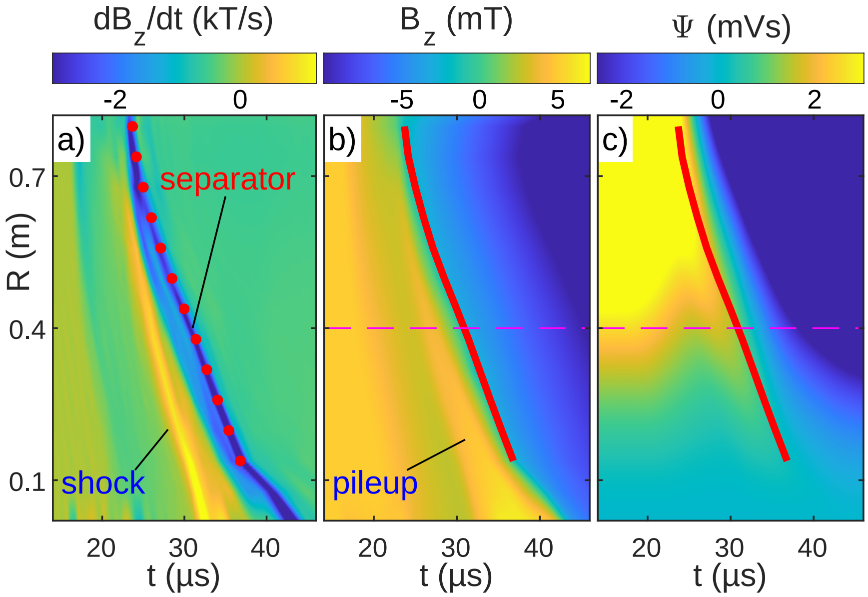

Figure 6.4: (a) Profile of $\partial B_Z/\partial t$ along R versus time from the speed probe. The reconnection current layer (separator) corresponds to the band of negatively peaked $\partial B_Z/\partial t$. A shock front, corresponding to the positive peak in the profile, leads the current layer. (b) Profile of B_Z, integrated from (a). A region of pileup follows the shock front at lower R. (c) Profile of the magnetic flux Ψ, calculated from (b). The red line in (b-c) indicates the reconnection separator.

The profile in Fig. 6.4(a) therefore provides a direct image of the toroidal current as a function of (t, R), where the reconnection separator (current layer) is identified as the positive ridge of $\partial B_Z/\partial t$ and the shock front leading the separator is the negative ridge of $\partial B_Z/\partial t$. The local slopes of these fronts in the (t, R)-plane yield the speeds v_{pile} and v_{layer}, for the shock and reconnection layer, respectively.

Taking into account the background Helmholtz magnetic field, B_H, the profile of B_Z in Fig. 6.4(b) is readily obtained as

$$B_Z(t, R) = B_H + \int_0^t \frac{\partial B_Z}{\partial t'} dt' \,, \tag{6.2}$$

where we have marked the region of magnetic pileup corresponding to the magnetic field compression at the shock front. In addition, the red line indicates the trajectory of the separator, $R_X(t)$.

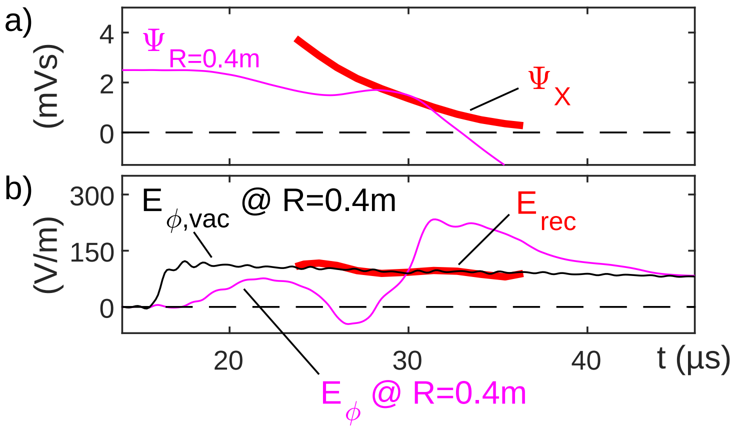

Figure 6.5: (a) Time trace of Ψ at $R = 0.4$ m [along the dashed pink line in Fig. 6.4(c)] and the magnetic flux evaluated along the separator trajectory [red line in Fig. 6.4(c)]. (b) Inductive electric field E_ϕ evaluated at $R = 0.4$ m and along the separator trajectory, denoted as the reconnection electric field E_{rec}. E_ϕ at $R = 0.4$ m is also provided for a separate shot in vacuum.

For this chapter the magnetic flux function is defined as

$$\Psi(t, R) = 2\pi \int_0^R R' B_Z(t, R') dR' \,, \tag{6.3}$$

or the total poloidal flux through a toroidal loop of radius R, which differs from the magnetic flux function defined in Eq. 3.5 by a factor of 2π. In turn, $\Psi(t, R)$ is readily computed and shown in Fig. 6.4(c).

With the knowledge of the separator trajectory $R_X(t)$, the absolute rate of magnetic reconnection can be inferred directly from the profile of $\Psi(t, R)$. Assuming axisymmetry (which will be verified below), the amount of magnetic flux below the separator is given by

$$\Psi_X = \Psi(t, R_X(t)) \,. \tag{6.4}$$

As shown by the red line in Fig. 6.5(a), Ψ_X decreases in time corresponding to the reconnection rate of the full system, $-d\Psi(t, R_X(t))/dt$, the inductive loop voltage along the separator. Then, by Faraday's law, the reconnection rate per unit length toroidally along the X-line is given by the inductive electric field

$$E_{\text{rec}}(t) = -\frac{1}{2\pi R_X(t)} \frac{d\Psi(t, R_X(t))}{dt} \,. \tag{6.5}$$

The inferred profile of $E_{\text{rec}}(t)$ is shown by the red line in Fig. 6.5(b) and is observed to be near constant in time. This is in contrast to the behavior of the inductive electric field observed in the lab-frame at $R = 0.4$ m (magenta line) during a plasma discharge which is strongly modified from the vacuum electric field observed with the same drive (black line). As is evident by the magenta line, the reconnection drive from 17 μs$<\ t\ <$19 μs is fully shielded by the plasma current channel building close to the coils as they are first energized. Then, once the reconnection geometry fully forms and travels past $R = 0.4$ m, the magenta line follows a characteristic wave pattern about the black vacuum-line corresponding to the perturbation in the inductive electric field from the steadily moving reconnection current layer. At $t \simeq 30$ μs, the current layer peak has reached $R = 0.4$ m, and the magenta and red traces coincide. Therefore, at the X-line, the reconnection electric field E_{rec} is identical to the inductive electric field observed in the lab-frame, which is expected here since $B_Z = 0$. The reconnection electric field calculated along the separator trajectory is roughly equivalent to the vacuum electric field measured at $R = 0.4$ m but is thought to be mostly coincidental for this case. As will be shown in Section 6.6, the reconnection electric field does correlate to the applied drive voltage, but there is significant spread in the measured E_{rec} for different experimental configurations that otherwise would have equivalent vacuum electric fields.

The analysis above relied on an assumption of toroidal symmetry. This symmetry has been experimentally verified by the work of other graduate students after the conclusion of the presented experimental run using a specially built curved $\dot{B}$ probe which is inserted into the plasma at $R = 0.4$ m and near the Z location of the X-line. The probe array then measures $\partial B_Z/\partial t$ with magnetic pickup loops along a 90 arc in the ϕ direction. The data in Fig. 6.6 shows how the reconnection layer reaches the curved probe simultaneously (at $t \simeq 32$ μs) along its full toroidal arc. Some structure and variation observed in $\partial B_Z/\partial t$ in the vicinity of the reconnection layer may be associated with a lower-hybrid drift instability and is the subject of continuing research on TREX. Nevertheless, the simultaneous observation of the peak current along the full probe is direct evidence that the reconnection layer propagates inwards with strong toroidal symmetry. This data therefore validates the assumption of toroidal symmetry in evaluating $\Psi(t, R_X(t))$, from which the toroidal inductive electric field, E_{rec} is inferred. Note, however, that additional electrostatic

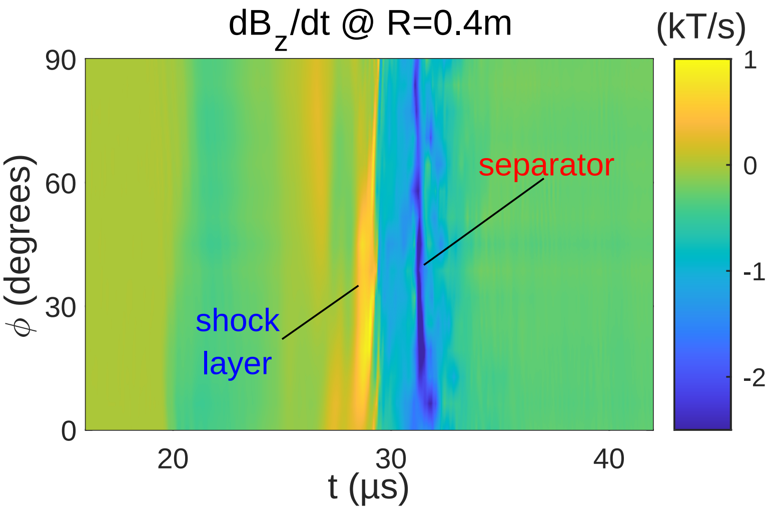

Figure 6.6: Time series of $\partial B_Z/\partial t$ (representative of J_ϕ) evaluated along a 90 arc in the ϕ direction. This data was taken for a single shot with a specially made curved magnetic probe array located at $R = 0.4$ m and $Z = 0.2$ m, parallel to ϕ. As in Fig. 6.4(a), the shock front, indicated by the positive peak, leads the separator (current layer), indicated by the negative peak.

electric fields may still be present in the toroidal direction, but their integral along the full X-line will vanish as electrostatic fields always have $-\oint \nabla\Phi \cdot d\mathbf{l} = 0$.

Finally, the experimental configuration presented here strongly resembles that of Chapter 4 in which spontaneously forming plasmoids cause strong fluctuations in the inductive electric field and toroidal current but are observed at much less frequent rates. The root cause of the plasmoids in the earlier TREX experiments is not known, and therefore it is difficult to determine the exact reason for the reduction. One possible explanation stems from the upgraded drive system which permits the application of drive voltages increased by a factor of 10–100 compared to those in Chapter 4. The dynamics of the current layer may therefore be dominated by the drive, suppressing the formation and growth of similar magnetic islands. However, this is in contrast to the expectation that current layers typically become more susceptible to plasmoid formation at increased current layer length and larger S. Another potential difference between the two configurations is the suppression of 3-dimensional effects associated with the change from the LaB$_6$ cathodes to the plasma gun array for plasma generation, as well as from the changes in the drive. Regardless of the origin of the plasmoids on TREX, it is simple to screen the speed probe data for the characteristic fluctuations that accompany plasmoids in these discharges to confirm that no plasmoids are included in the following dataset.

6.5 Shock Front and Magnetic Flux Pileup

As discussed in Chapter 4, the TREX experiment operates in a low collisional regime where Hall physics becomes important [62]. An example event is presented in Fig. 6.7 in H_2 with $V_{\text{drive}} = 5$ kV and $B_H = 5$ mT. The data in Fig. 6.7(a-c), taken from Fig. 6.3 at $\Delta t = 4$ μs, include the reconnecting magnetic field component B_Z as well as profiles of the toroidal current J_ϕ and in-plane Hall current J_Z. The steady motion of the reconnection layer demonstrated in Fig. 6.3 and the nearly constant layer speed shown in Fig. 6.4 facilitates the "jogging" method applied to obtain the profiles of n_e, V_f, and T_e in Fig. 6.7(d-f) measured at fixed $R = 0.4$ m and scanned in Z over multiple discharges. The time traces at each Z position are converted to a radial chord of measurements with

$$R' = R - R_0 = (t - t_0)v_{\text{layer}}\,, \tag{6.6}$$

where t_0 is the time the current layer passes $R_0 = 0.4$ m. The density profile is asymmetric with larger densities at low R. In the vicinity of the reconnection region the floating potential in Fig. 6.7(e) has a structure similar to that observed by the Cluster mission during reconnection in the Earth's magnetotail [104]. In addition, a sharp jump in the potential structure, $\Delta V_s \simeq 15$ V, is observed at $R' \simeq -0.2$ m providing evidence of a collisionless shock normal electric field E_R.

The far upstream plasma (low R) acts as the leading inflow, and its speed, in the frame of the reconnection layer, typically exceeds the local Alfvén speed. This upstream inflow must therefore be throttled in order for reconnection to take place at the appropriate rate. Thus, a region of magnetic pileup is observed to interface between the reconnection and upstream regions. Figure 6.8(a) shows a diagram of this configuration in which the upstream region, denoted by the color blue, is separated from the red reconnection layer by a shock in green and a region of pileup in purple. The differences are clear in Fig. 6.8(b) where an increase from the upstream field corresponds with a negative spike in toroidal current, driven by the electron $E \times B$-drift with E_R and B_Z. The surface

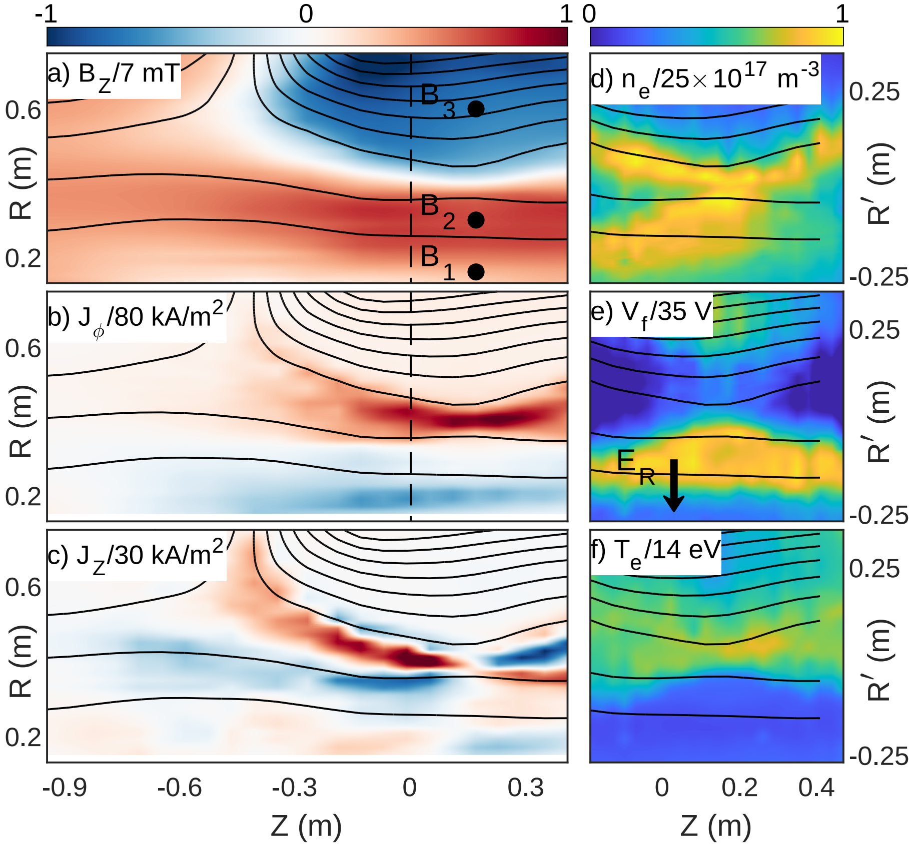

Figure 6.7: Profiles of a reconnection discharge in H_2 with $B_H = 5$ mT and $V_{\text{drive}} = 5$ kV. (a-c) The reconnecting magnetic field B_Z, toroidal current density J_ϕ, and poloidal current density J_Z are reconstructed from a radial scan with the hook probe array. Contours of constant Ψ are overlaid in black representing the poloidal magnetic field lines. (d-f) The electron density n_e, plasma floating potential V_f, and electron temperature T_e measured by scanning the electrostatic probe along Z at $R = 0.4$ m. Here, $R' = t' v_{\text{layer}}$ indicates the radial profile inferred from the temporal probe signal centered around $R = 0.4$ m.

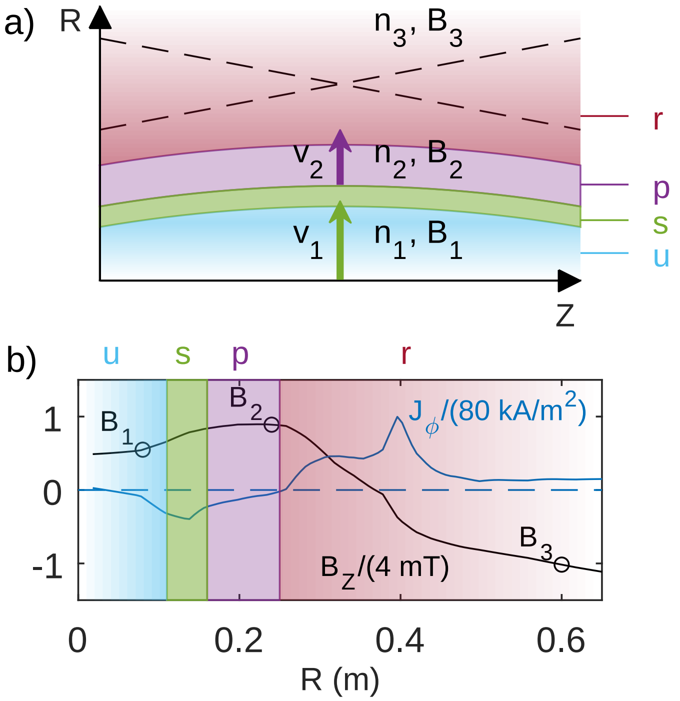

Figure 6.8: (a) A cartoon depiction of different regions within a TREX discharge. As the current layer is driven into the background plasma, a shock interface (green) separates a region of pileup (purple) from the far upstream (blue), preceding the reconnection layer (red). (b) Radial profiles of B_Z and J_ϕ from the speed probe along the dashed line in Fig. 6.7 at $Z = 0$ m.

current density across the shock can then be estimated as

$$K = \frac{en_e \Delta V_s}{B} \simeq 1.6\,\mathrm{kA/m}\,, \tag{6.7}$$

which is in agreement with the observed magnetic pileup of

$$\Delta B = \mu_0 K \simeq 2\ \ \mathrm{mT} \tag{6.8}$$

across the shock. The radial electric field E_R is also responsible for reducing the speed of the incoming ions traveling across the shock.

As a consequence of the high Lundquist number regime ($S > 10^3$) in which TREX operates, the negative toroidal current is not expected to be an inductive response to the collapsing reconnection current sheet. Outside the diffusion region, the pressure tensor and electron inertia terms in Ohm's law can be neglected such that $\mathbf{E} + \mathbf{v_e} \times \mathbf{B} \simeq \eta \mathbf{J}$. Using the experimental parameters within the shock,

$$\eta J_\phi \simeq 5 \cdot 10^{-5}\,\Omega\mathrm{m} \times 30\,\mathrm{kA/m^2} = 1.5\,\mathrm{V/m}\,, \tag{6.9}$$

which is much smaller than the typical inductive electric field $|E_\phi| \gtrsim 50$ V/m. Therefore, in the shock layer, $\mathbf{E} \simeq -\mathbf{v_e} \times \mathbf{B}$ and the role of E_ϕ is to drive radial flows of the electron fluid such this fluid strictly follows the radial motion of the magnetic field lines.

The profiles in Fig. 6.8 provide a qualitative picture of the TREX configurations whereas the exact details, how fast each layer moves or the amount of pileup, depend both on the reconnection dynamics as well as the imposed experimental settings. The gas species, number of plasma guns, Helmholtz field, and drive voltage all control certain aspects of a reconnection event. Figure 6.9 highlights how the magnetic field evolves throughout a shot for three different cases with varying gas, B_H, and V_{drive}. Each individual probe trace from the speed probe is normalized to 1 mT and offset by its respective radial location, mapping out the magnetic field as the layer moves past each probe toward the central axis. The solid red line indicates the trajectory of the layer where $B_Z = 0$ mT. The red dashed segment marks the region of interest corresponding to $R = 0.4$ m, the radial location of other probes, and where the following analysis is completed. Compared to Fig. 6.9(a) with $v_{\text{layer}} = 33$ km/s, the layer in Fig. 6.9(b) only moves at 22 km/s, indicative of the heavier ion species. Additionally, both v_{layer} and B_{rec} increase with V_{drive} when comparing Figs. 6.9(a,c). In each case, a shock front, indicated by the green line, propagates at a speed $v_{\text{pile}} > v_{\text{layer}}$ ahead of the current layer as it is driven into the relatively stationary bulk plasma. The shock compresses the upstream field to match the allowable reconnection rate, setting how quickly magnetic flux is transferred through the diffusion region, and thereby resulting in the observed B_{rec} and v_{layer}.

To document how different experimental settings yield different speeds of the reconnection layer, Fig. 6.10 includes 9 examples of $B_Z(t, R)$ similar to that in Fig. 6.4(b). V_{drive} increases from 3 kV to 5 kV, left to right, with gases of H_2, D, and He changing from top to bottom while keeping a constant $B_H = 4$ mT. The red dots represent $B_Z = 0$ mT at the location of each probe. The

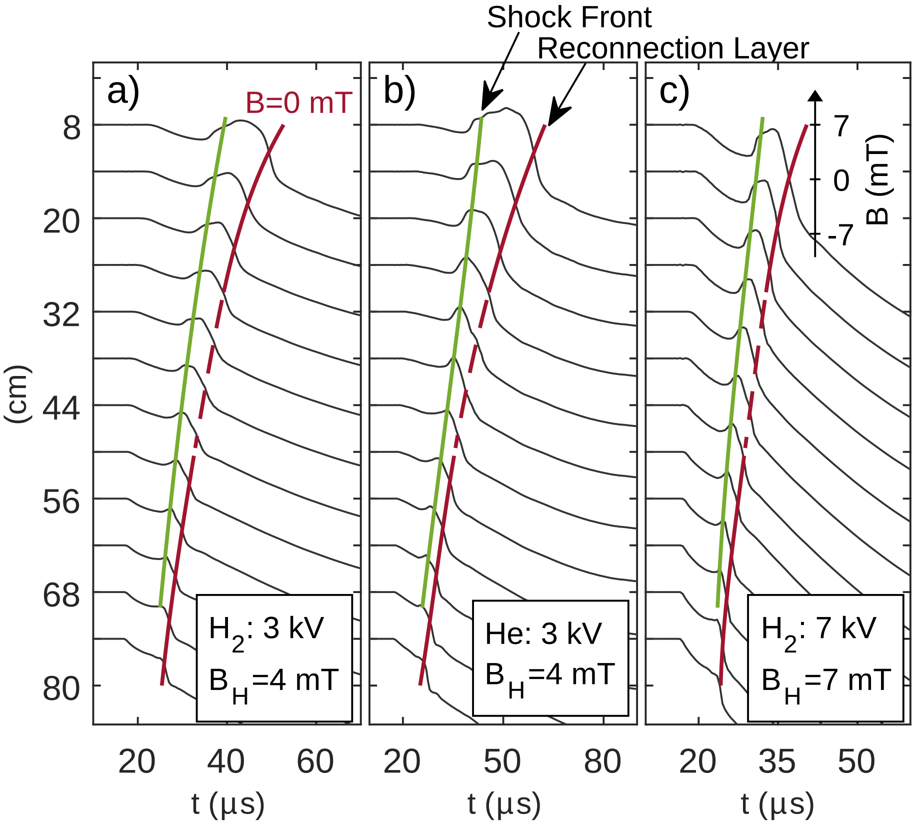

Figure 6.9: (a-c) Stack plots of magnetic field versus time from the speed probe for three different cases. The scales are normalized such that 1 mT=1 cm and offset by the R location of each probe. The changing time axes are indicative of the difference in timescales for these discharges. Using the method described in Fig. 6.4, the red line follows the $B = 0$ mT contour while the green line indicates the shock front leading the current layer.

black line indicates a constant velocity trajectory at v_{layer} where v_{layer} is determined by choosing the slope of the $B_Z = 0$ mT contour at $R = 0.4$ m.

Figures 6.9 and 6.10 present a subset of the larger overall scan performed on TREX consisting of 882 total shots with all experimental parameters for this dataset shown in Table 6.1. Every possible combination of gas and number of plasma guns with the specified sets of Helmholtz field and drive voltage were explored, encompassing 90 different configurations of ~10 shots each. Sets of B_H and V_{drive} were chosen to roughly balance each other in order to create reconnection layers

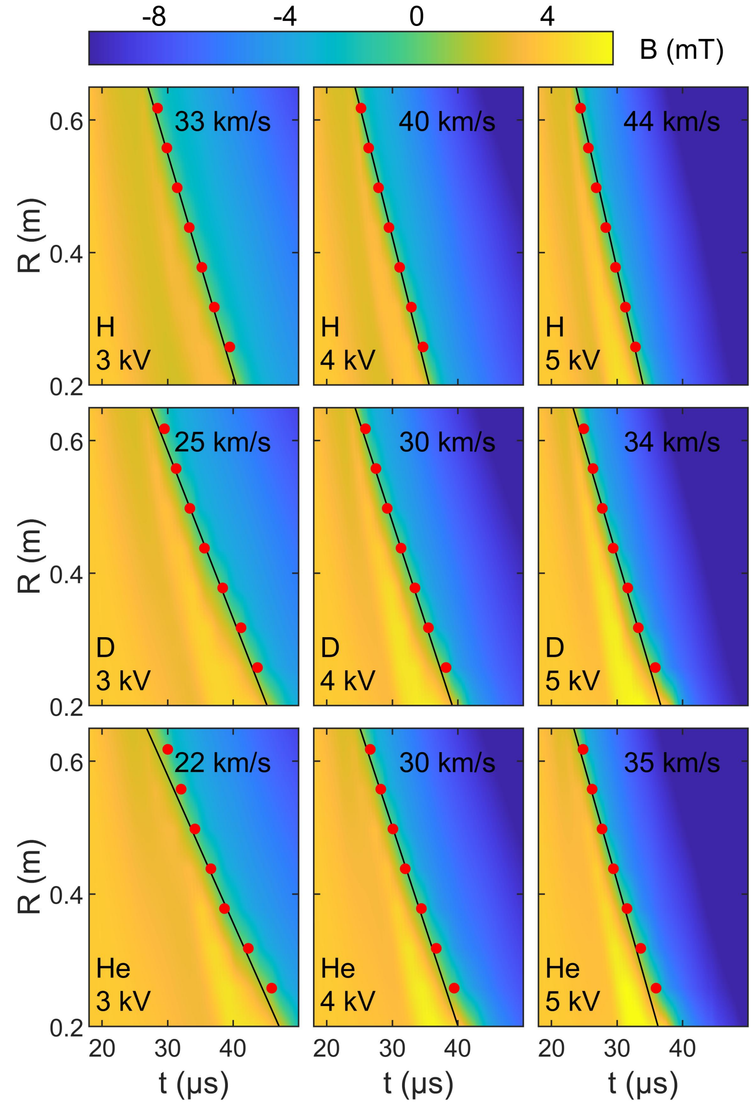

Figure 6.10: Comparison of $B_Z(R, Z = 0)$ calculated from the speed probe for varying experimental conditions.

Gas	Number of Guns
H_2	2
D	6
He	

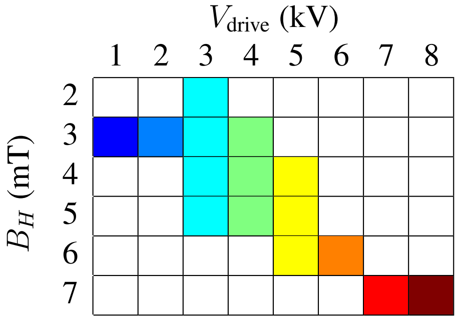

B_H (mT) \ V_{drive} (kV)	1	2	3	4	5	6	7	8
2			🟦					
3	🟦	🟦	🟦	🟩				
4			🟦	🟩	🟨			
5			🟦	🟩	🟨			
6					🟨	🟧		
7							🟥	🟫

Table 6.1: The experimental parameters used for the dataset presented, including gas species, number of plasma guns, voltage drive, and Helmholtz field. B_H was chosen to approximately balance the resulting reconnecting field set by V_{drive}.

that are only slightly asymmetric. Extreme cases of V_{drive} relative to B_H (or the inverse) are not considered here.

Through this parameter scan, we find that the amount of pileup is not only regulated by the reconnection process, but rather the magnetic field and density adjust to remain in force balance with the upstream plasma, consistent with the Rankine-Hugoniot jump conditions for shocked flows [105, 106, 107, 108]. In addition to magnetic and plasma pressure, the ram pressure associated with the flowing mass into and out of the shock interface must be included in the total pressure,

$$P_\alpha = m_i n_\alpha v_\alpha^2 + \frac{B_\alpha^2}{2\mu_0} + n_\alpha T_\alpha \,, \tag{6.10}$$

where the subscript α corresponds to individual regions indicated in the simplified drawing in Fig. 6.8(a). Flux and particle continuity provide further constraints on the allowable parameters such that

$$\begin{aligned} \frac{n_1}{B_1} &= \frac{n_2}{B_2} \\ \frac{n_1}{v_2} &= \frac{n_2}{v_1} \,, \end{aligned} \tag{6.11}$$

where subscripts 1 and 2 correspond to the upstream and pileup regions, respectively. Using Eqs. 6.10 and 6.11, the total pressures for both regions across the shock interface are then

$$\begin{aligned} P_1 &= m_i n_1 v_1^2 + \frac{B_1^2}{2\mu_0} + n_1 T_1 \\ P_2 &= m_i n_1 v_1^2 \frac{B_1}{B_2} + \frac{B_2^2}{2\mu_0} + n_1 T_2 \frac{B_2}{B_1} \,, \end{aligned} \tag{6.12}$$

where $T = T_e + T_i \simeq T_e$ throughout the experiment. The velocities in Eqs. 6.12 are described in the frame of the shock layer, but v_1 can simply be taken as v_{pile}, the shock velocity measured in the lab frame. Typical values for v_{pile} range from $1.1 M_{\text{MS}}$ to $1.5 M_{\text{MS}}$, where M_{MS} is the magnetosonic Mach number. As seen in Fig. 8 of Ref. [108], for the observed plasma beta of $\beta \sim 0.1$, the critical Mach number at which all ions will be reflected from an incoming perpendicular shock is ~ 2.7, well above the observed range of v_{pile} for these experiments. Additionally, the electron inertial length $d_e \sim 1$ cm at the shock front is larger than the characteristic magnetic Reynolds length scale, $L_m = \eta/(\mu_0 v_{\text{pile}}) \sim 0.1$ cm. Therefore, the observed shocks tend to steepen to the size of a few d_e wide, consistent with a sub-critical dispersive (rather than resistive) shock [108].

The upstream and pileup pressures are easily computed from measurements and are plotted in Fig. 6.11(a) where each data point corresponds to the average of all shots for a single configuration in Table 6.1. The dashed line of slope 1 shows good agreement between the total pressure on either side of the shock front and that force balance is satisfied across the interface regardless of the externally imposed conditions. A representative set of pressure profiles is given in Fig. 6.11(b) which shows a discrete drop in ram pressure across the shock front that is largely balanced by a rise in magnetic pressure, as expected.

For this set of experiments, shocks are observed to form in all Hydrogen and Deuterium cases and most of the Helium cases. Deriving a strict drive-threshold for the shock formation is difficult with the given dataset as the background magnetic field and drive voltage are not fully independent. Rather, B_H is adjusted within a range that decreases with decreasing reconnection drive. Furthermore, after triggering the reconnection drive but before the reconnection and shock layers have fully formed, the background field declines, which is most pronounced at higher V_{drive}. The upstream Alfvén speed of the shock is then indirectly related to the reconnection drive. In

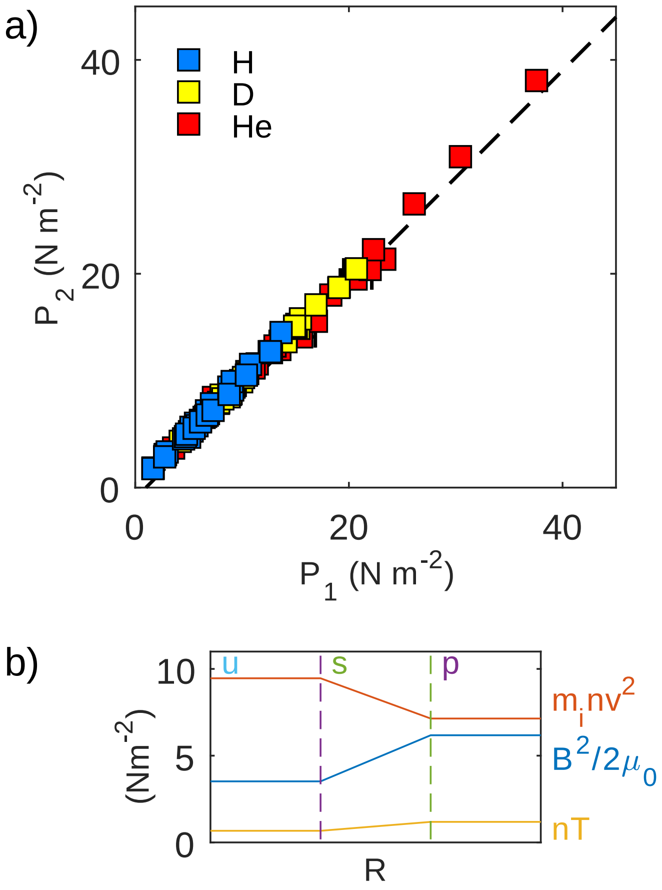

Figure 6.11: (a) A comparison of the total pressures P_1 and P_2 for all configurations of the dataset. (b) Depiction of the change in ram, magnetic, and plasma pressures for the event in Fig. 6.8(b) going from the upstream (u) to the pileup (p) regions across the shock interface (s). The standard deviation error for each configuration generally falls below the marker size.

other experiments not presented here, shock formation is not found to occur for $V_{\text{drive}} < 300$ V in Hydrogen.

6.6 Reconnection Rate

In conjunction with the pileup front, the reconnection region also freely develops given the existing parameters, typically exhibiting both magnetic and density asymmetries across the layer. To account for this, flux and particle continuity into the layer can be used to derive an expected scaling for asymmetric reconnection [85] dependent on both inflow magnetic field and density values $B_2,\ B_3,\ n_2,$ and n_3. The expected reconnection rate is then written as

$$E_{\text{rec}} = \alpha v_{\text{Ah}} B_{\text{red}} \,, \tag{6.13}$$

where α is a factor dependent on the specific geometry of the layer. This is similar to the symmetric reconnection rate but modified by a reduced magnetic field

$$B_{\text{red}} = \frac{2B_2B_3}{B_2 + B_3} \tag{6.14}$$

and a hybrid Alfvén speed,

$$v_{\text{Ah}} = \left(\frac{1}{\mu_0 m_i}\frac{B_2B_3(B_2+B_3)}{n_3B_2+n_2B_3}\right)^{1/2} \,, \tag{6.15}$$

where m_i is the ion mass. Typically, $B_2 < B_3$ while $n_3 < n_2$. As indicated in Figs. 6.7(a) and 6.8(b), values for v_{Ah} and B_{red} are determined by choosing measurements $\sim 1d_i$ away from either side of the layer, consistent with procedures used in theory [29]. The location of the flux pileup values naturally sits $\gtrsim 0.6d_i$ away from the reconnection layer.

As described in Sec. 6.4, the measured reconnection electric field E_{rec} is readily computed by finding the change in magnetic flux along the X-line trajectory (Eq. 6.5). Then carrying out the above analysis for all shots in the scan provides an overall scaling of E_{rec} to $v_{\text{Ah}}B_{\text{red}}$, shown in Fig. 6.12, for the TREX experiment. The absolute electric field only shows a significant dependency on V_{drive} as seen in Fig. 6.12(a). As V_{drive} is increased from 1 kV to 8 kV, E_{rec} increases roughly proportionally over the range. Additionally, E_{rec} increases linearly to $v_{\text{Ah}}B_{\text{red}}$ on the x-axis such that the normalized reconnection rate

$$\alpha = \frac{E_{\text{rec}}}{v_{\text{Ah}}B_{\text{red}}} \approx 0.53 \pm 0.05 \tag{6.16}$$

is constant. This value for α in the experiment is larger than the typical rate $\alpha \sim 0.1$ often associated with fast reconnection. It is important to note that both the density and ion species are included through the v_{Ah} term in the scaling. The same results are shown in Figs. 6.12(b-c) with respect to the gas and number of plasma guns used, respectively. As evidence that the ions are

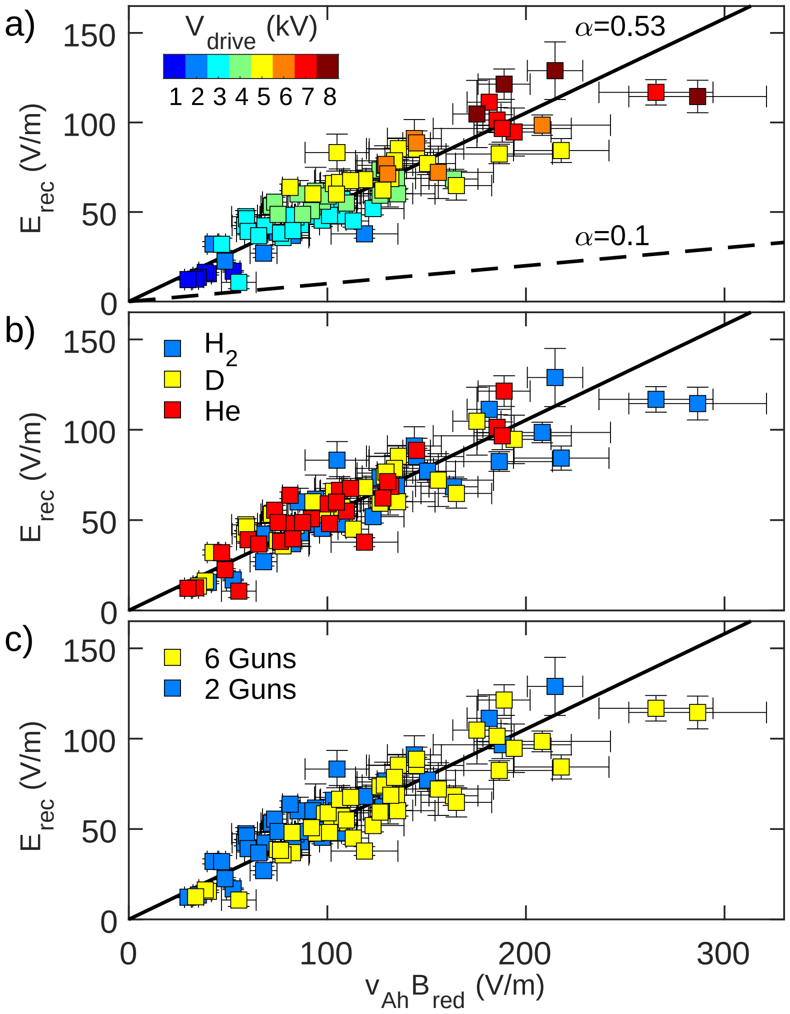

Figure 6.12: (a) Scaling of the reconnection rate with respect to V_{drive}. Each data point represents the average of all shots for a single configuration with errorbars indicating the weighted variance for each group. The solid line fit to the full dataset with slope $\alpha = E_{\text{rec}}/v_{\text{Ah}}B_{\text{red}}$ represents the average reconnection rate compared to the dashed line of slope $\alpha = 0.1$. (b-c) The same data as in (a) mapped to the ion species and plasma gun number, respectively.

magnetized, no noticeable change in scaling is observed for $m_p \leq m_i \leq 4m_p$ or between 6 and 2 guns, which corresponds to a factor of 2 difference in density between similar configurations. Another representation of the data is provided in Fig. 6.13, displaying $\alpha = E_{\text{rec}}/(v_{\text{Ah}}B_{\text{red}})$ as a function of the normalized system size L/d_i, where $L \simeq 0.8$ m is the half-length of the current

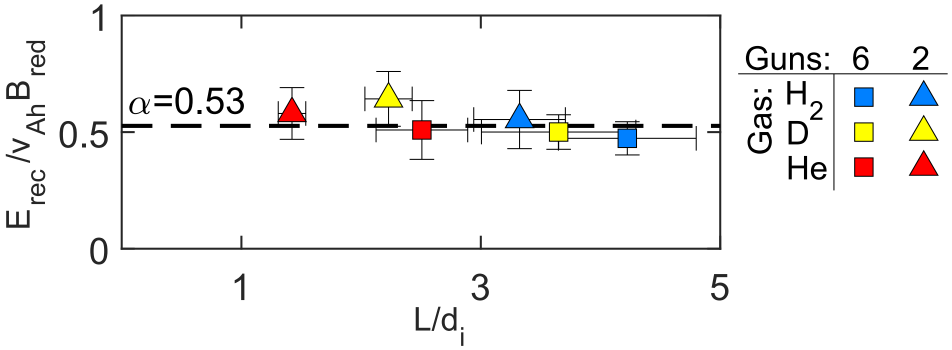

Figure 6.13: The reconnection rate α as a function of the normalized system size L/d_i. Each data point represents all discharges from with similar ion species and number of plasma guns.

layer. The observed reconnection rate is in agreement with theoretical results [90] in which α becomes large for small island coalescence ($L/d_i < 5d_i$) but moderately declines for larger system size. Additionally, recent studies of reconnection in the subsolar magnetopause in which the solar wind electric field largely controls the local reconnection rate under certain conditions [100] show similar influence from external conditions on the reconnection rate.

The results presented thus provide experimental confirmation of previous numerical studies on flux pileup. Simulations of laser produced plasma bubbles have shown that the reconnection rate only matches the expected rate when taking into consideration flux pileup [101], while laboratory experiments of this nature also see rates of $\alpha > 0.5$ [14]. However, as a main difference, the observed reconnection rate on TREX is steady in nature, as E_{rec} is nearly constant during the full layer transit time.

In conclusion, recent experiments on TREX have shown a systematic regulation of the reconnection electric field through the externally applied loop voltage of the drive coils. Additionally, magnetic pileup is associated with shock formation at the interface to the upstream plasma. While the absolute reconnection electric field is set externally, the current in the reconnection layer and the shock formation ultimately regulate the level of flux pileup such that the normalized reconnection rate remains constant over all experimental configurations.

Chapter 7

Conclusion

As the first experimental endeavor outside of the plasma dynamo research on the original MPDX device, the development and implementation of TREX was instrumental in realizing the full potential and versatility of the BRB as part of a basic plasma facility. At the beginning of this research, much of the BRB experimental facility was already constructed with active development from other students and research staff. The primary contributions of the author to the greater facility were the addition of the Helmholtz coil and associated power supplies and controls, as well as implementing the set of fast digitizers into the data acquisition system. The capacitor banks used for the TREX drive system were developed and constructed by the author with the oversight of senior technician Paul Nonn. The internal drive coils were originally designed by engineer John Wallace and constructed and implemented onto the device by the author. The various magnetic diagnostics were largely the project of other graduate students in the TREX group with some guidance from the author. The continued development of the T_e probe, based off previous experimental work, was the sole responsibility of the author. The experimental campaigns for TREX were largely group efforts involving the entire TREX team. As such, shared between members are often multiple avenues of research utilizing the same datasets. While the initial setup and calibration of magnetic diagnostics were the responsibility of other students, the analysis contained herein was performed by the author with supervision from Prof. Jan Egedal and with input from the rest of the TREX team.

7.1 Summary of Thesis

The beginning of this thesis covered the basic details of magnetic reconnection and its importance to many astrophysical and terrestrial plasma systems. A major focus of Chapter 1 was the prevalence of collisionless reconnection and the importance of the recently identified kinetic regime where kinetic effects such as electron pressure anisotropy fundamentally alter the reconnection dynamics. This is born out by recent spacecraft missions like NASA's MMS, already making measurements of the electron diffusion region in Earth's magnetosphere at unprecedented detail. The primary motivation for the creation of the Terrestrial Reconnection Experiment at the University of Wisconsin-Madison has been and still remains the study of fully collisionless reconnection in the laboratory to support the plethora of theoretical and observational work in the area. While the expected physics in the kinetic regime are not the subject of the subsequent results contained in this thesis, it remains the driving factor in the development of the experimental hardware comprising TREX.

With the experimental motivation explained, Chapter 2 continued with a description of the facility in which TREX resides. Due to its versatility, the novel BRB device proved to be the perfect base for a new magnetic reconnection experiment. With much of the development of the BRB device and its components completed, this lessened the overhead required to construct and prepare a fully new experimental device from scratch. Following descriptions of the general BRB components, the specific hardware for the first implementation of TREX was covered in Chapter 3. This introduced the components that transform the BRB into a reconnection experiment, namely the reconnection drive system and dedicated diagnostic suite.

Using this configuration, results from the first TREX experimental campaign were described in Chapter 4. The following list compiles the observations and conclusions included in the report, providing new insights into the dynamics of reconnection.

1. Demonstrated magnetic reconnection with Lundquist number of $S \sim 10^3$ and relative system size of $L/d_i \sim 1$, placing these experiments deeply into the collisionless regime where collisions do not play an important role in force balance in the reconnection region.

2. At the relatively low drives associated with this configuration, the current layers are susceptible to magnetic tearing and the formation of plasmoids, or magnetic islands.

3. These plasmoids have a drastic effect on the reconnection dynamics during an event with observations of strongly varying electric field and current density as the plasmoids are formed and ejected.

4. These constitute the first observations of plasmoids in a regime characterized by high S and low L/d_i and are unexpected by theory.

Chapter 5 covered improvements to the device hardware that followed the above experiments. These upgrades attempted to address the ruggedness of the experimental components as well as attain higher S and reach into the aforementioned kinetic regime. The primary change to the hardware was an increase in loop voltages of over $10\times$ from the previous configuration. Following these changes to the device, another experimental campaign was performed to study the properties of the increased drive and better understand the reconnection process on TREX. The following list describes the main results presented in Chapter 6.

1. At the higher drive strength, plasmoids are much less prominent, demonstrating the driven nature of the experiment.

2. Showed the systematic control of the reconnection electric field through the applied loop voltage of the drive coils and observed a fixed normalized reconnection where $E_{\text{rec}} \simeq 0.5 v_{\text{Ah}} B_{\text{red}}$.

3. Observed the formation of subcritical shocks upstream of the current layer and showed that pressure balance over the shock interface allows for magnetic pileup leading the current layer.

4. While the electric field is set externally, the current in the reconnection layer and shock formation allow the reconnection process to proceed at a constant normalized rate.

7.2 Future Work

This dissertation represents only the first results from the Terrestrial Reconnection Experiment with many other experimental studies occurring in parallel. Numerous research projects could follow based on this foundational work. Regarding the early plasmoid experiments, there still remains a question as to what the root cause of the observed plasmoids is. More experimentation is necessary to better understand the underlying processes than is present in the current dataset. Additionally, with the help of collaborators at Los Alamos National Laboraotry, the TREX group has had success implementing the TREX configuration into a cylindrical PIC code with realistic experimental parameters. Simulations with correspondingly low drive provide an opportunity to study the kinetic dynamics that otherwise would be difficult to implement in the experiment.

For the second set of experiments presented, questions regarding the specific reconnection rate on TREX remain. In particular, is the observed reconnection rate a consequence of the macro-scale geometry set by the drive coils? The current layer length seems to be controlled largely by the extent of the drive coils. While not necessarily a quick task, an easy way to see a change in the aspect ratio of the reconnection geometry is to add more drive coils to the setup. With a significant enough change in the length of the current layer, it is expected that the normalized reconnection rate on TREX would decrease. This is another area that would benefit from the use of simulations to alleviate the experimental hurdles in order to test this conjecture.

Finally, as has been stressed throughout this thesis, TREX has been developed with the particular motivation of conducting an experimental study of magnetic reconnection in the kinetic regime where electron pressure anisotropy can develop unimpeded by Coulomb collisions. To date, TREX has operated with parameters up to $S \sim 10^4$ and relative system size of $L/d_i \lesssim 8$, below the expected threshold of $S \gtrsim 10^5$ to reliably reach the kinetic regime given by Eq. 1.23. An important implication of the results from Chapter 6 are that the reconnection magnetic field is largely controlled by the applied loop voltage since $V_{\text{loop,x}} = 2\pi E_{\text{rec}} \propto v_A B_{\text{rec}}$ and thus $B_{\text{rec}} \propto V_{\text{loop,x}}^{-1/2}$. Because the necessary value of v_A used in S depends on the size of B_{rec}, then S is also largely controlled by the applied loop voltage. With this in mind, plans are currently in place to optimize the reconnection drive with a more ideal drive geometry by replacing the drive coils with a "drive cylinder." The present design shown in Fig. 7.1 has a length and diameter both of 1.5 m. The larger Lundquist number is achieved in part because the cylinder has more efficient penetration of loop voltage in its interior compared to discrete coils. In addition, estimates suggest the current layer will nearly double in length. With a reduction in the density to keep L/d_i similar to the current configuration and a corresponding reduction in the collision frequency, the result will be a Lundquist number similar to the desired $S \sim 10^5$.

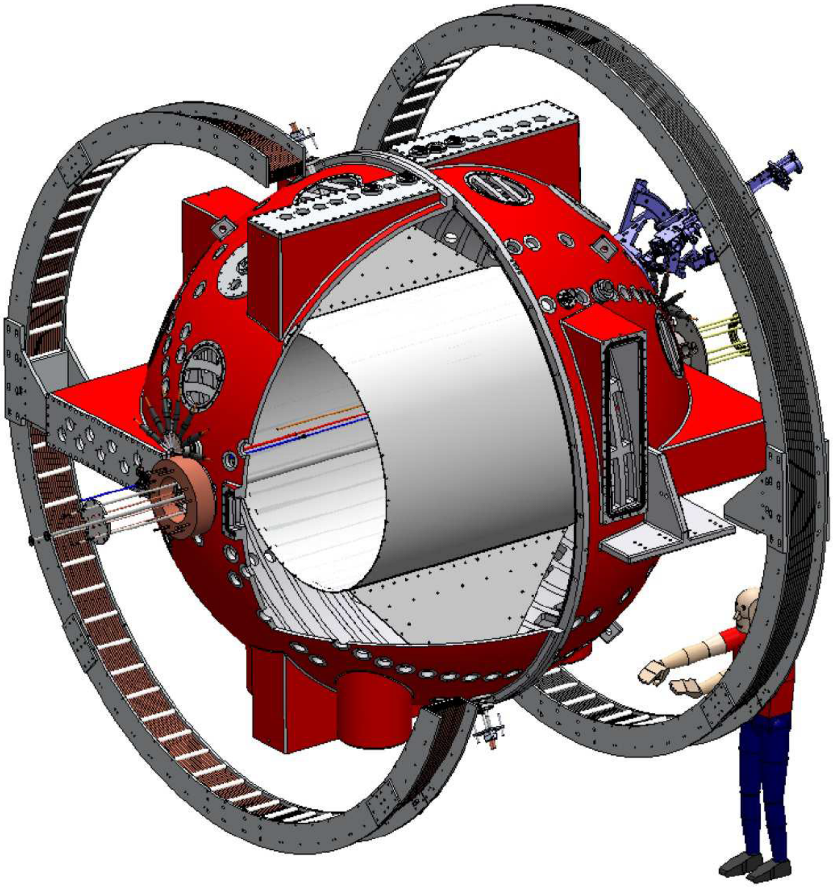

Figure 7.1: TREX with the reconnection drive coils replaced by a drive cylinder.

References

[1] E. Priest and T. Forbes, *Magnetic reconnection: MHD Theory and Applications* (Cambridge University Press, 2000).

[2] J. Dungey, Philos. Mag. **44**, 725 (1953).

[3] P. Sweet, in *Electromagn. Phenom. Cosm. Phys.*, IAU Symposium, Vol. 6, edited by B. Lehnert (1958) p. 123.

[4] E. N. Parker, J. Geophys. Res. **62**, 509 (1957).

[5] S. Masuda, T. Kosugi, H. Hara, S. Tsuneta, and Y. Ogawara, Nature **371**, 495 (1994).

[6] K. Shibata and S. Tanuma, Earth, Planets Sp. **53**, 473 (2001).

[7] T. D. Phan, L. M. Kistler, B. Klecker, G. Haerendel, G. Paschmann, B. U. Sonnerup, W. Baumjohann, M. B. Bavassano-Cattaneo, C. W. Carlson, A. M. DiLellis, K. H. Fornacon, L. A. Frank, M. Fujimoto, E. Georgescu, S. Kokubun, E. Moebius, T. Mukai, M. Øieroset, W. R. Paterson, and H. Reme, Nature **404**, 848 (2000).

[8] V. Angelopoulos, J. P. McFadden, D. Larson, C. W. Carlson, S. B. Mende, H. Frey, T. Phan, D. G. Sibeck, K.-H. Glassmeier, U. Auster, E. Donovan, I. R. Mann, I. J. Rae, C. T. Russell, A. Runov, X.-Z. Zhou, and L. Kepko, Science (80-.). **321**, 931 (2008).

[9] J. L. Burch, R. B. Torbert, T. D. Phan, L. J. Chen, T. E. Moore, R. E. Ergun, J. P. Eastwood, D. J. Gershman, P. A. Cassak, M. R. Argall, S. Wang, M. Hesse, C. J. Pollock, B. L. Giles, R. Nakamura, B. H. Mauk, S. A. Fuselier, C. T. Russell, R. J. Strangeway, J. F. Drake, M. A. Shay, Y. V. Khotyaintsev, P. A. Lindqvist, G. Marklund, F. D. Wilder, D. T. Young,

K. Torkar, J. Goldstein, J. C. Dorelli, L. A. Avanov, M. Oka, D. N. Baker, A. N. Jaynes, K. A. Goodrich, I. J. Cohen, D. L. Turner, J. F. Fennell, J. B. Blake, J. Clemmons, M. Goldman, D. Newman, S. M. Petrinec, K. J. Trattner, B. Lavraud, P. H. Reiff, W. Baumjohann, W. Magnes, M. Steller, W. Lewis, Y. Saito, V. Coffey, and M. Chandler, Science (80-.). **352** (2016), 10.1126/science.aaf2939.

[10] Y. Nagayama, K. M. McGuire, M. Bitter, A. Cavallo, E. D. Fredrickson, K. W. Hill, H. Hsuan, A. Janos, W. Park, G. Taylor, and M. Yamada, Phys. Rev. Lett. **67**, 3527 (1991).

[11] M. Yamada, F. M. Levinton, N. Pomphrey, R. Budny, J. Manickam, and Y. Nagayama, Phys. Plasmas **1**, 3269 (1994).

[12] J. Egedal, W. Fox, N. Katz, M. Porkolab, K. Reim, and E. Zhang, Phys. Rev. Lett. **98**, 015003 (2007).

[13] Y. Ren, M. Yamada, H. Ji, S. Dorfman, S. P. Gerhardt, and R. Kulsrud, Phys. Plasmas **15**, 1 (2008).

[14] G. Fiksel, W. Fox, A. Bhattacharjee, D. H. Barnak, P. Y. Chang, K. Germaschewski, S. X. Hu, and P. M. Nilson, Phys. Rev. Lett. **113**, 1 (2014).

[15] M. Yamada, J. Geophys. Res. Sp. Phys. **104**, 14529 (1999).

[16] M. R. Brown, C. D. Cothran, and J. Fung, Phys. Plasmas **13**, 056503 (2006).

[17] J. D. Hare, L. G. Suttle, S. V. Lebedev, N. F. Loureiro, A. Ciardi, J. P. Chittenden, T. Clayson, S. J. Eardley, C. Garcia, J. W. D. Halliday, T. Robinson, R. A. Smith, N. Stuart, F. Suzuki-Vidal, and E. R. Tubman, Phys. Plasmas **25**, 055703 (2018).

[18] J. P. Freidberg, *Ideal Magnetohydrodynamics* (Plenum Press, New York, 1987).

[19] T. Tajima and K. Shibata, *Plasma Astrophysics* (Addison-Wesley, Reading, 1997).

[20] R. Giovanelli, Nature **158**, 81 (1946).

[21] E. G. Zweibel and M. Yamada, Annu. Rev. Astron. Astrophys. **47**, 291 (2009).

[22] D. Biskamp, Phys. Fluids **29**, 1520 (1986).

[23] H. Ji, M. Yamada, S. Hsu, and R. Kulsrud, Phys. Rev. Lett. (1998).

[24] W. Daughton, V. Roytershteyn, B. J. Albright, H. Karimabadi, L. Yin, and K. J. Bowers, Phys. Rev. Lett. **103**, 065004 (2009).

[25] B. Sonnerup, Comput. Phys. Commun. **49**, 143 (1988).

[26] D. A. Uzdensky and R. M. Kulsrud, Phys. Plasmas **13**, 062305 (2006).

[27] E. G. Zweibel and M. Yamada, Proc. R. Soc. A Math. Phys. Eng. Sci. **472** (2016), 10.1098/rspa.2016.0479.

[28] J. Birn, J. F. Drake, M. a. Shay, B. N. Rogers, R. E. Denton, M. Hesse, M. Kuznetsova, Z. W. Ma, a. Bhattacharjee, a. Otto, and P. L. Pritchett, J. Geophys. Res. **106**, 3715 (2001).

[29] M. A. Shay, J. F. Drake, B. N. Rogers, and R. E. Denton, J. Geophys. Res. Sp. Phys. **106**, 3759 (2001).

[30] A. Le, J. Egedal, W. Daughton, J. F. Drake, W. Fox, and N. Katz, Geophys. Res. Lett. **37**, 1 (2010).

[31] Y. Ren, M. Yamada, S. Gerhardt, H. T. Ji, R. Kulsrud, and A. Kuritsyn, Phys. Rev. Lett. **95**, 55003 (2005).

[32] M. Øieroset, T. D. Phan, M. Fujimoto, R. P. Lin, and R. P. Lepping, Nature **412**, 414 (2001).

[33] T. D. Phan, G. Paschmann, C. Twitty, F. S. Mozer, J. T. Gosling, J. P. Eastwood, M. Øieroset, H. Rème, and E. A. Lucek, Geophys. Res. Lett. **34**, L14104 (2007).

[34] L. Comisso and A. Bhattacharjee, J. Plasma Phys. **82** (2016), 10.1017/S002237781600101X.

[35] N. F. Loureiro, A. A. Schekochihin, and S. C. Cowley, Phys. Plasmas **14** (2007), 10.1063/1.2783986.

[36] A. Bhattacharjee, Y.-M. Huang, H. Yang, and B. Rogers, Phys. Plasmas **16**, 112102 (2009).

[37] M. Øieroset, R. P. Lin, T. D. Phan, D. E. Larson, and S. D. Bale, Phys. Rev. Lett. **89**, 195001 (2002).

[38] K.-J. Hwang, M. L. Goldstein, D. E. Wendel, A. N. Fazakerley, and C. Gurgiolo, J. Geophys. Res. Sp. Phys. **118**, 4199 (2013).

[39] J. Egedal, W. Fox, N. Katz, M. Porkolab, M. Øieroset, R. P. Lin, W. Daughton, and J. F. Drake, J. Geophys. Res. Sp. Phys. **113**, n/a (2008).

[40] J. Egedal, A. Le, and W. Daughton, Phys. Plasmas **20** (2013), 10.1063/1.4811092.

[41] A. Le, J. Egedal, W. Daughton, W. Fox, and N. Katz, Phys. Rev. Lett. **102**, 085001 (2009).

[42] J. Ng, J. Egedal, A. Le, W. Daughton, and L. J. Chen, Phys. Rev. Lett. **106**, 1 (2011).

[43] O. Ohia, J. Egedal, V. S. Lukin, W. Daughton, and A. Le, Phys. Rev. Lett. **109**, 1 (2012).

[44] A. Le, J. Egedal, O. Ohia, W. Daughton, H. Karimabadi, and V. S. Lukin, Phys. Rev. Lett. **110**, 1 (2013).

[45] A. Le, J. Egedal, and W. Daughton, Phys. Plasmas **23** (2016), 10.1063/1.4964768.

[46] A. Le, J. Egedal, W. Daughton, V. Roytershteyn, H. Karimabadi, and C. Forest, J. Plasma Phys. **81**, 305810108 (2015).

[47] W. Daughton and V. Roytershteyn, Space Sci. Rev. **172**, 271 (2012).

[48] H. Ji and W. Daughton, Phys. Plasmas **18**, 111207 (2011).

[49] C. M. Cooper, J. Wallace, M. Brookhart, M. Clark, C. Collins, W. X. Ding, K. Flanagan, I. Khalzov, Y. Li, J. Milhone, M. Nornberg, P. Nonn, D. Weisberg, D. G. Whyte, E. Zweibel, and C. B. Forest, Phys. Plasmas **21**, 013505 (2014).

[50] E. J. Spence, K. Reuter, and C. B. Forest, Astrophys. J. **700**, 470 (2009).

[51] D. B. Weisberg, E. Peterson, J. Milhone, D. Endrizzi, C. Cooper, V. Désangles, I. Khalzov, R. Siller, and C. B. Forest, Phys. Plasmas **24**, 056502 (2017).

[52] C. B. Forest, K. Flanagan, M. Brookhart, M. Clark, C. M. Cooper, V. Desangles, J. Egedal, D. Endrizzi, I. V. Khalzov, H. Li, M. Miesch, J. Milhone, M. Nornberg, J. Olson, E. Peterson, F. Roesler, A. Schekochihin, O. Schmitz, R. Siller, A. Spitkovsky, A. Stemo, J. Wallace, D. Weisberg, and E. Zweibel, J. Plasma Phys. **81**, 1 (2015), arXiv:1506.07195 [physics.plasm-ph] .

[53] C. M. Cooper, D. B. Weisberg, I. Khalzov, J. Milhone, K. Flanagan, E. Peterson, C. Wahl, and C. B. Forest, Phys. Plasmas **23**, 102505 (2016).

[54] E. E. Peterson, D. A. Endrizzi, M. Beidler, K. J. Bunkers, M. Clark, J. Egedal, K. Flanagan, K. J. McCollam, J. Milhone, J. Olson, C. R. Sovinec, R. Waleffe, J. Wallace, and C. B. Forest, Nat. Phys. **15**, 1095 (2019).

[55] D. B. Weisberg, *Pursuing the Plasma Dynamo and MRI in the Laboratory: Hydrodynamic Studies of Unmagnetized Plasmas at Large Reynolds Number*, Ph.D. thesis, University of Wisconsin - Madison (2016).

[56] G. Fiksel, A. F. Almagri, D. Craig, M. Iida, S. C. Prager, and J. S. Sarff, Plasma Sources Sci. Technol **5**, 78 (1996).

[57] M. Bongard, G. Bodner, M. Burke, R. Fonck, J. Pachicano, J. Perry, C. Pierren, J. Reusch, A. Rhodes, N. Richner, C. Rodriguez Sanchez, C. Schaefer, and J. Weberski, Nucl. Fusion **59**, 076003 (2019).

[58] M. I. Brookhart, *Subcritical Onset of Plasma Fluctuations and Magnetic Self-Organization in a Line-Tied Screw Pinch*, Ph.D. thesis, University of Wisconsin - Madison (2015).

[59] a. Kesich, J. Bonde, J. Egedal, W. Fox, R. Goodwin, N. Katz, a. Le, and Others, Rev. Sci. Instrum. **79**, 1 (2008).

[60] N. Hershkowitz, in *Plasma Diagnostics Disch. Parameters Chem.*, edited by O. Auciello and D. L. Flamm (Academic Press, Inc., 1989) 1st ed., Chap. 3, pp. 113–183.

[61] I. H. Hutchinson, *Fusion Technol.*, 2nd ed., Vol. 17 (Cambridge University Press, 2002).

[62] J. Olson, J. Egedal, S. Greess, R. Myers, M. Clark, D. Endrizzi, K. Flanagan, J. Milhone, E. Peterson, J. Wallace, D. Weisberg, and C. B. Forest, Phys. Rev. Lett. **116**, 1 (2016).

[63] J. F. Drake, M. Swisdak, H. Che, and M. A. Shay, Nature **443**, 553 (2006).

[64] M. Yamada, Y. Ren, H. Ji, J. Breslau, S. Gerhardt, R. Kulsrud, and A. Kuritsyn, Phys. Plasmas **13**, 52119 (2006).

[65] W. Daughton, J. Scudder, and H. Karimabadi, Phys. Plasmas **13**, 072101 (2006).

[66] W. Daughton, V. Roytershteyn, H. Karimabadi, L. Yin, B. J. Albright, B. Bergen, and K. J. Bowers, Nat. Phys. **7**, 539 (2011).

[67] L. J. Chen, A. Bhattacharjee, P. A. Puhl-Quinn, H. Yang, N. Bessho, S. Imada, S. Muehlbachler, P. W. Daly, B. Lefebvre, Y. Khotyaintsev, A. Vaivads, A. Fazakerley, and E. Georgescu, Nat. Phys. **4**, 19 (2008).

[68] M. Øieroset, T. D. Phan, J. P. Eastwood, M. Fujimoto, W. Daughton, M. A. Shay, V. Angelopoulos, F. S. Mozer, J. P. McFadden, D. E. Larson, and K. H. Glassmeier, Phys. Rev. Lett. **107** (2011), 10.1103/PhysRevLett.107.165007.

[69] H. S. Fu, J. B. Cao, Y. V. Khotyaintsev, M. I. Sitnov, A. Runov, S. Y. Fu, M. Hamrin, M. André, A. Retinò, Y. D. Ma, H. Y. Lu, X. H. Wei, and S. Y. Huang, Geophys. Res. Lett. **40**, 6023 (2013).

[70] S. Takasao, A. Asai, H. Isobe, and K. Shibata, Astrophys. J. **745**, L6 (2012).

[71] N. Nishizuka, H. Takasaki, A. Asai, and K. Shibata, Astrophys. J. **711**, 1062 (2010).

[72] G. Lapenta, S. Markidis, M. V. Goldman, and D. L. Newman, Nat. Phys. **11**, 690 (2015).

[73] M. I. Sitnov, M. Swisdak, and A. V. Divin, J. Geophys. Res. Sp. Phys. **114**, n/a (2009).

[74] N. F. Loureiro and D. A. Uzdensky, Plasma Phys. Control. Fusion **58**, 14021 (2016).

[75] S. Dorfman, H. Ji, M. Yamada, J. Yoo, E. Lawrence, C. Myers, and T. D. Tharp, Geophys. Res. Lett. **40**, 233 (2013).

[76] J. D. Hare, L. Suttle, S. V. Lebedev, N. F. Loureiro, A. Ciardi, G. C. Burdiak, J. P. Chittenden, T. Clayson, C. Garcia, N. Niasse, T. Robinson, R. A. Smith, N. Stuart, F. Suzuki-Vidal, G. F. Swadling, J. Ma, J. Wu, and Q. Yang, Phys. Rev. Lett. **118**, 1 (2017).

[77] W. Gekelman and H. Pfister, Phys. Fluids **31**, 2017 (1988).

[78] W. Gekelman, P. Pribyl, Z. Lucky, M. Drandell, D. Leneman, J. Maggs, S. Vincena, B. Van Compernolle, S. K. P. Tripathi, G. Morales, T. A. Carter, Y. Wang, and T. DeHaas, Rev. Sci. Instrum. **87**, 025105 (2016).

[79] B. U. O. Sonnerup, *Magnetic field reconnection, in Solar System Plasma Physics, vol. 3* (edited by L. T. Lanzerotti, C. F. Kennel, and E. N. Parker, pp. 45 108, North-Holland, New York, 1979).

[80] A. Borg, M. Øieroset, T. Phan, F. Mozer, A. Pedersen, C. Mouikis, J. McFadden, C. Twitty, A. Balogh, and H. Rème, Geophy. Res. Lett. **32**, 19105 (2005).

[81] J. Yoo and M. Yamada, J. Geophys. Res. Sp. Phys. **117**, 12202 (2012).

[82] J. T. Gosling, S. Eriksson, T. D. Phan, D. E. Larson, R. M. Skoug, and D. J. McComas, Geophys. Res. Lett. **34**, n/a (2007).

[83] T. D. Phan, M. A. Shay, J. T. Gosling, M. Fujimoto, J. F. Drake, G. Paschmann, M. Oieroset, J. P. Eastwood, and V. Angelopoulos, Geophys. Res. Lett. **40**, 4475 (2013).

[84] J. Yoo, M. Yamada, H. Ji, J. Jara-Almonte, C. E. Myers, and L.-J. Chen, Phys. Rev. Lett. **113**, 95002 (2014).

[85] P. A. Cassak and M. A. Shay, Phys. Plasmas **14**, 102114 (2007).

[86] H. Ji, Y. Ren, M. Yamada, S. Dorfman, W. Daughton, and S. P. Gerhardt, Geophys. Res. Lett. **35**, n/a (2008), arXiv:1001.0082 .

[87] D. A. Uzdensky, N. F. Loureiro, and A. A. Schekochihin, Phys. Rev. Lett. **105**, 235002 (2010).

[88] J. A. Wesson, Plasma Phys. Control. Fusion **28**, 243 (1986).

[89] Y. H. Liu, M. Hesse, F. Guo, W. Daughton, H. Li, P. A. Cassak, and M. A. Shay, Phys. Rev. Lett. **118** (2017), 10.1103/PhysRevLett.118.085101.

[90] J. Ng, Y. M. Huang, A. Hakim, A. Bhattacharjee, A. Stanier, W. Daughton, L. Wang, and K. Germaschewski, Phys. Plasmas **22** (2015), 10.1063/1.4935302.

[91] H. Karimabadi, J. Dorelli, V. Roytershteyn, W. Daughton, and L. Chacón, Phys. Rev. Lett. **107**, 1 (2011).

[92] M. Hesse and J. Birn, Adv. Sp. Res. **13**, 249 (1993).

[93] W. I. Axford, Rev. Geophys. **7**, 421 (1969).

[94] W. I. Axford, in *Magn. Reconnect. Sp. Lab. Plasmas, Geophys. Monogr. Ser.*, edited by E. W. H. Jr. (American Geophysical Union (AGU), 1984) pp. 1–8.

[95] Y. Matsumoto, T. Amano, T. N. Kato, and M. Hoshino, Science (80-.). **347**, 974 (2015).

[96] H. Karimabadi, V. Roytershteyn, H. X. Vu, Y. A. Omelchenko, J. Scudder, W. Daughton, A. Dimmock, K. Nykyri, M. Wan, D. Sibeck, M. Tatineni, A. Majumdar, B. Loring, and B. Geveci, Phys. Plasmas **21**, 062308 (2014).

[97] J. C. Dorelli and J. Birn, J. Geophys. Res. Sp. Phys. **108** (2003), 10.1029/2001JA009180.

[98] T. Moretto, D. G. Sibeck, B. Lavraud, K. J. Trattner, H. Rème, and A. Balogh, Ann. Geophys. **23**, 2259 (2005).

[99] M. Øieroset, T. D. Phan, J. F. Drake, J. P. Eastwood, S. A. Fuselier, R. J. Strangeway, C. Haggerty, M. A. Shay, M. Oka, S. Wang, L. J. Chen, I. Kacem, B. Lavraud, V. Angelopoulos, J. L. Burch, R. B. Torbert, R. E. Ergun, Y. Khotyaintsev, P. A. Lindqvist, D. J. Gershman, B. L. Giles, C. Pollock, T. E. Moore, C. T. Russell, Y. Saito, L. A. Avanov, and W. Paterson, Geophys. Res. Lett. **46**, 1937 (2019).

[100] J. C. Dorelli, J. Geophys. Res. Sp. Phys. **14**, 2018JA025868 (2019).

[101] W. Fox, A. Bhattacharjee, and K. Germaschewski, Phys. Rev. Lett. **106**, 1 (2011).

[102] L. G. Suttle, J. D. Hare, S. V. Lebedev, G. F. Swadling, G. C. Burdiak, A. Ciardi, J. P. Chittenden, N. F. Loureiro, N. Niasse, F. Suzuki-Vidal, J. Wu, Q. Yang, T. Clayson, A. Frank, T. S. Robinson, R. A. Smith, and N. Stuart, Phys. Rev. Lett. **116**, 225001 (2016).

[103] T. P. Intrator, X. Sun, G. Lapenta, L. Dorf, and I. Furno, Nat. Phys. **5**, 521 (2009).

[104] J. R. Wygant, C. A. Cattell, R. Lysak, Y. Song, J. Dombeck, J. McFadden, F. S. Mozer, C. W. Carlson, G. Parks, E. A. Lucek, A. Balogh, M. Andre, H. Reme, M. Hesse, and C. Mouikis, J. Geophys. Res. Sp. Phys. **110**, 1 (2005).

[105] W. J. Macquorn Rankine, *Philos. Trans. R. Soc. London*, Tech. Rep. (1870).

[106] P. H. Hugoniot, Paris J. Ec. Polytech **57**, 3 (1887).

[107] P. H. Hugoniot, Paris J. Ec. Polytech **58**, 1 (1889).

[108] C. F. Kennel, J. P. Edmiston, and T. Hada, in *Collisionless Shock. Heliosph. A Tutor. Rev. Vol. 34*, Vol. 34 (1985) Chap. 1, pp. 1–36.

Appendix A:
Cathode Power Supply Schematics

Figure A.1 shows the full schematic drawing for the cathode power supply and discharge circuit presented in Section 2.3. The capacitor bank is charged through a simple rectifier circuit to the desired voltage. Residential AC can vary in voltage around the nominal 120 V RMS rating, so this is passed through a constant voltage transformer with a steady 120 V output. A step-up transformer with 480 VAC output follows into a full-bridge diode rectifier with a DC output of 432 V ($\sim V_{\text{RMS}}\sqrt{8}/\pi$) connected across the capacitors. The remaining components are used for control and operation of the charging/discharging of the capacitors across the cathodes.

Two important features of this design are the comparator and IGCT relay circuits shown in Figs. A.2 and A.3, respectively. The comparator circuit functions to disconnect the AC input from the rectifier once the capacitor reaches a target voltage. The capacitor voltage and the voltage set point, controlled through a front panel potentiometer, passes through a standard op-amp comparator circuit that switches a solid state relay (K2), thereby effectively turning off the charging output, leaving the capacitors at the desired voltage. It is critical that the IGCT used to trigger the discharge circuit is in a safe state before charging the capacitors, otherwise risking catastrophic damage to the IGCT. The IGCT relay reads in the IGCT status from a fiber optic output and switches another solid state relay (K1) in series with the charging supply input, preventing charging until the IGCT is in a ready state.

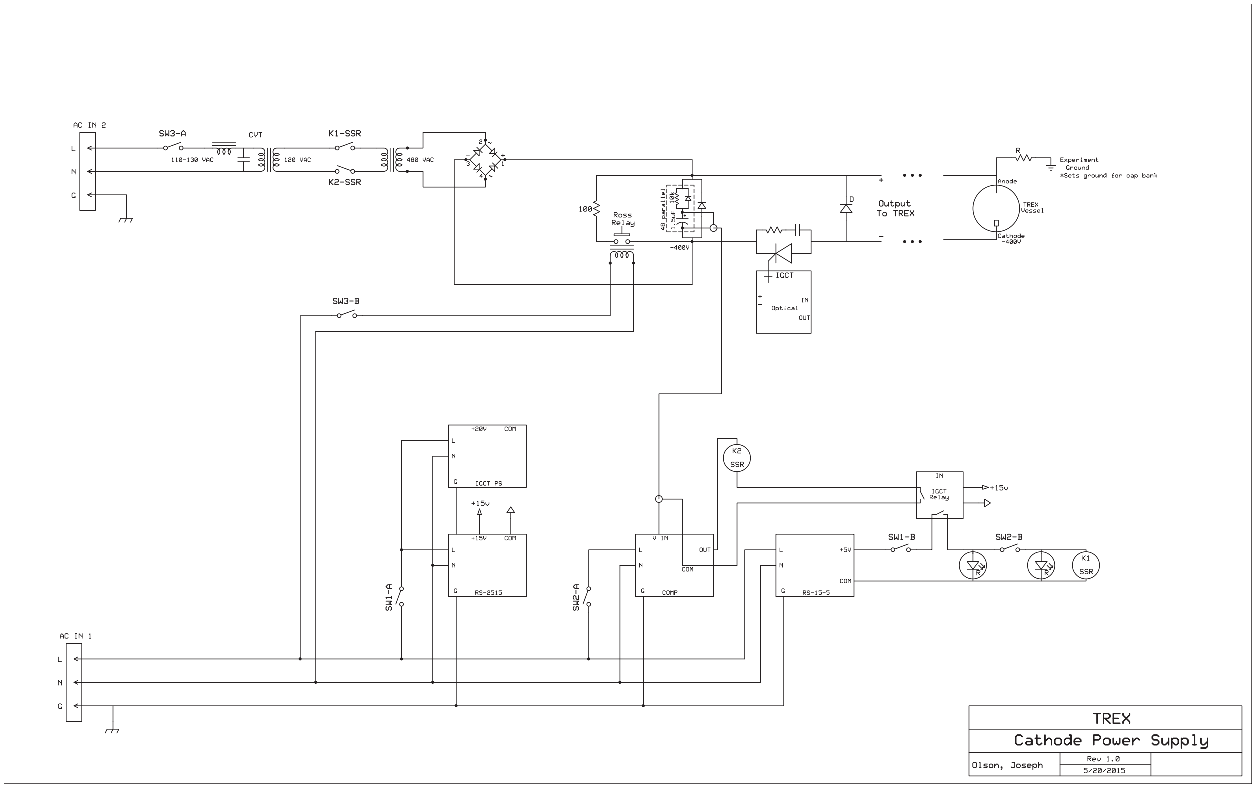

Figure A.1: Full schematic diagram for the cathode discharge circuit used in Chapters. 2 and 4.

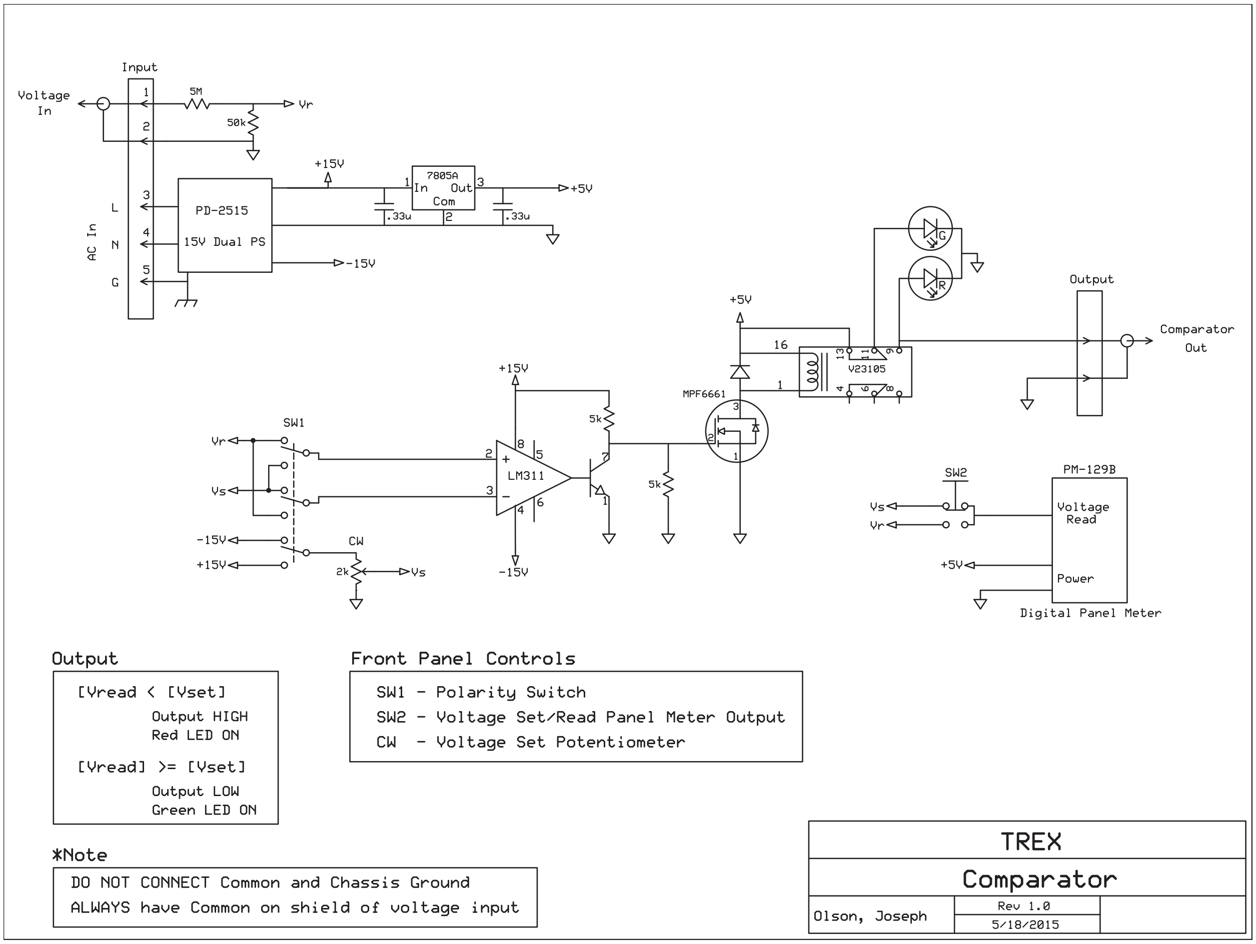

Output

[Vread < [Vset]
Output HIGH
Red LED ON

[Vread] >= [Vset]
Output LOW
Green LED ON

Front Panel Controls

SW1 - Polarity Switch
SW2 - Voltage Set/Read Panel Meter Output
CW - Voltage Set Potentiometer

***Note**

DO NOT CONNECT Common and Chassis Ground
ALWAYS have Common on shield of voltage input

TREX
Comparator
Olson, Joseph
Rev 1.0
5/18/2015

Figure A.2: Schematic diagram of the comparator circuit used to power on/off the charging supply.

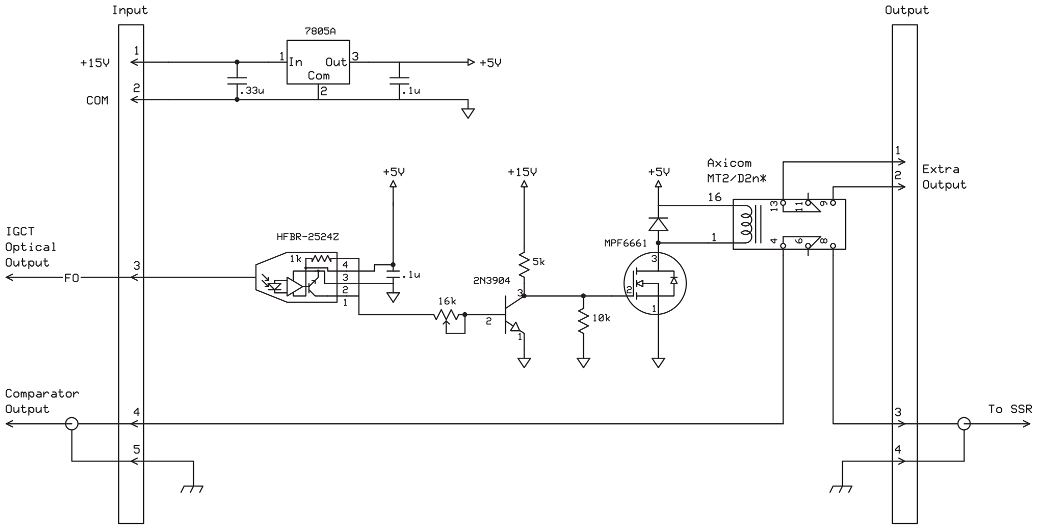

<u>Truth Table</u>

Input	HFBR-2524Z	2N3904	MPF6661	Output
H	0 V	10 V (Cutoff)	0 V (Saturation)	Closed
L	5 V	0 V (Active)	5 V (Cutoff)	Open

TREX

IGCT Relay Circuit

Olson, Joseph
Rev 1.0
5/15/2015

Figure A.3: Schematic diagram of the IGCT ready relay circuit.

Appendix B:
Alpha Power Supply Schematics

The full schematic diagram for the alpha power supplies described in Section 2.6 is shown in Figs. B.1 and B.2, with each figure representing one half of the schematic. The Alphas are constant current power supplies with up to 800 A output current with a simple design. Across the top of each figure are the primary power components. The 3-phase 480 VAC input passes through a series of variable transformers to control the input voltage to a 3-phase step-up transformer and rectifier. This DC output then passes through a bank of active pass transistors used to control the final output current. The remainder of the schematic shows the local/remote controls, interlocks, and other sub-circuits used to control the primary components.

Developed by the author, a separate control circuit is used to interface with the BRB control system through the cRIO controller. This control circuit is shown in Figs. B.3 and B.4 with each diagram representing the units that sit near the Alphas and cRIO, respectively. The primary functionality of the control interface is to convert the available cRIO module inputs/outputs into the appropriate signals for the existing Alpha remote controls while keeping the two systems, Alpha and cRIO, electrically isolated. This is accomplished with the use of optical isolators for binary controls and galvanically isolated current/voltage transducers (LEMs) for monitoring output and set point levels.

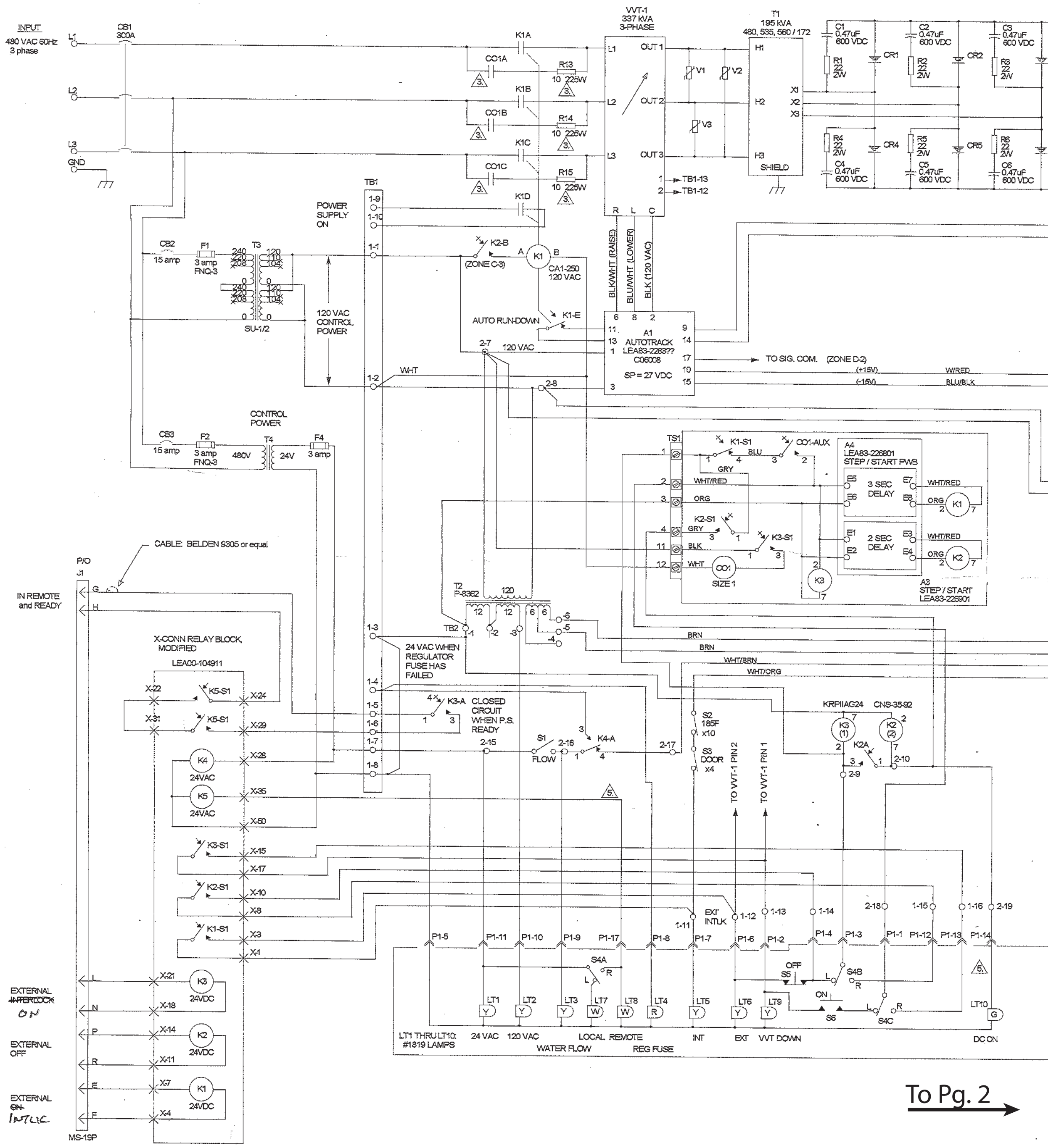

To Pg. 2

Figure B.1: Schematic drawing of the Alpha power supply, Pg. 1.

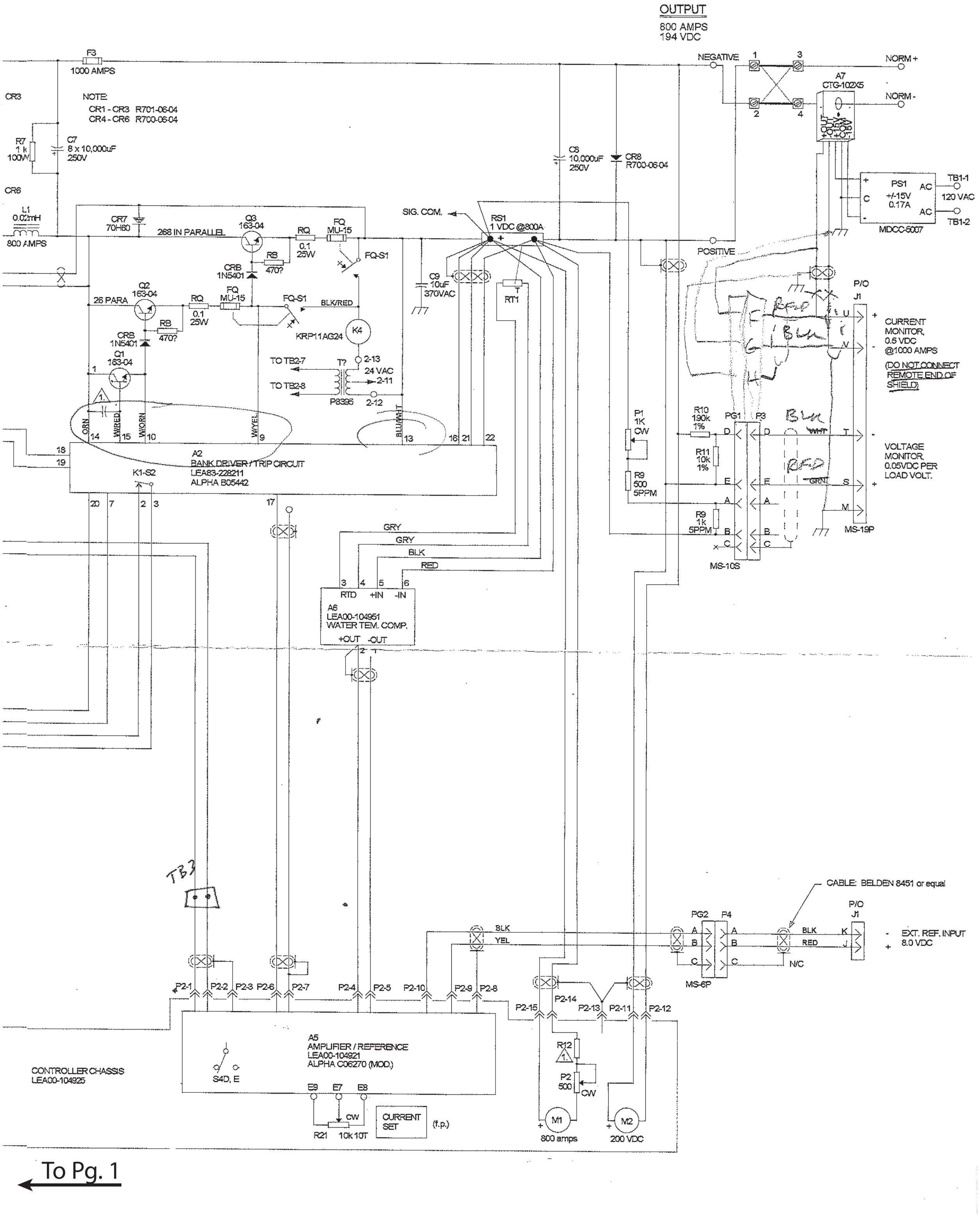

Figure B.2: Schematic drawing of the Alpha power supply, Pg. 2.

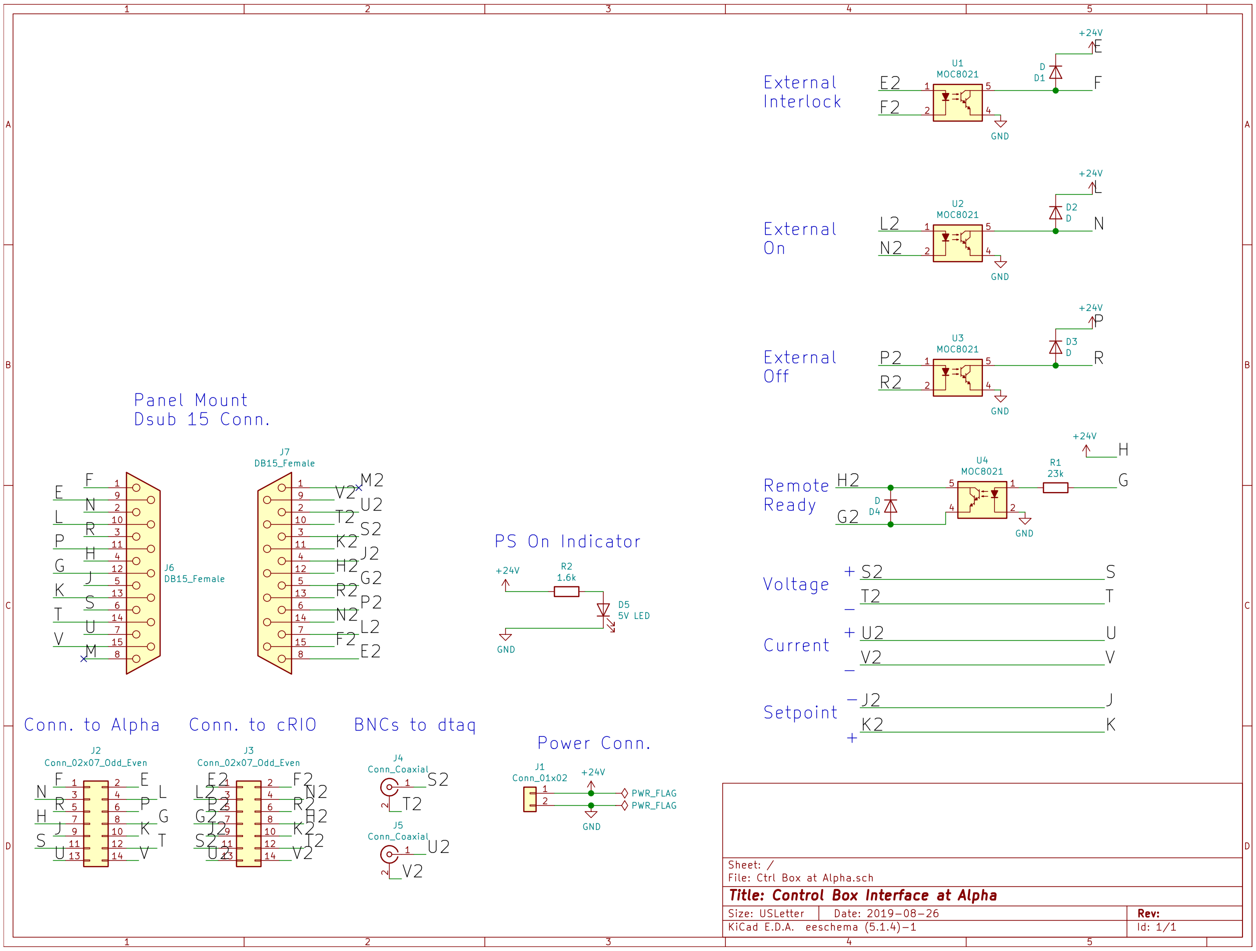

Figure B.3: Schematic diagram of the Alpha control interface sitting at the Alpha.

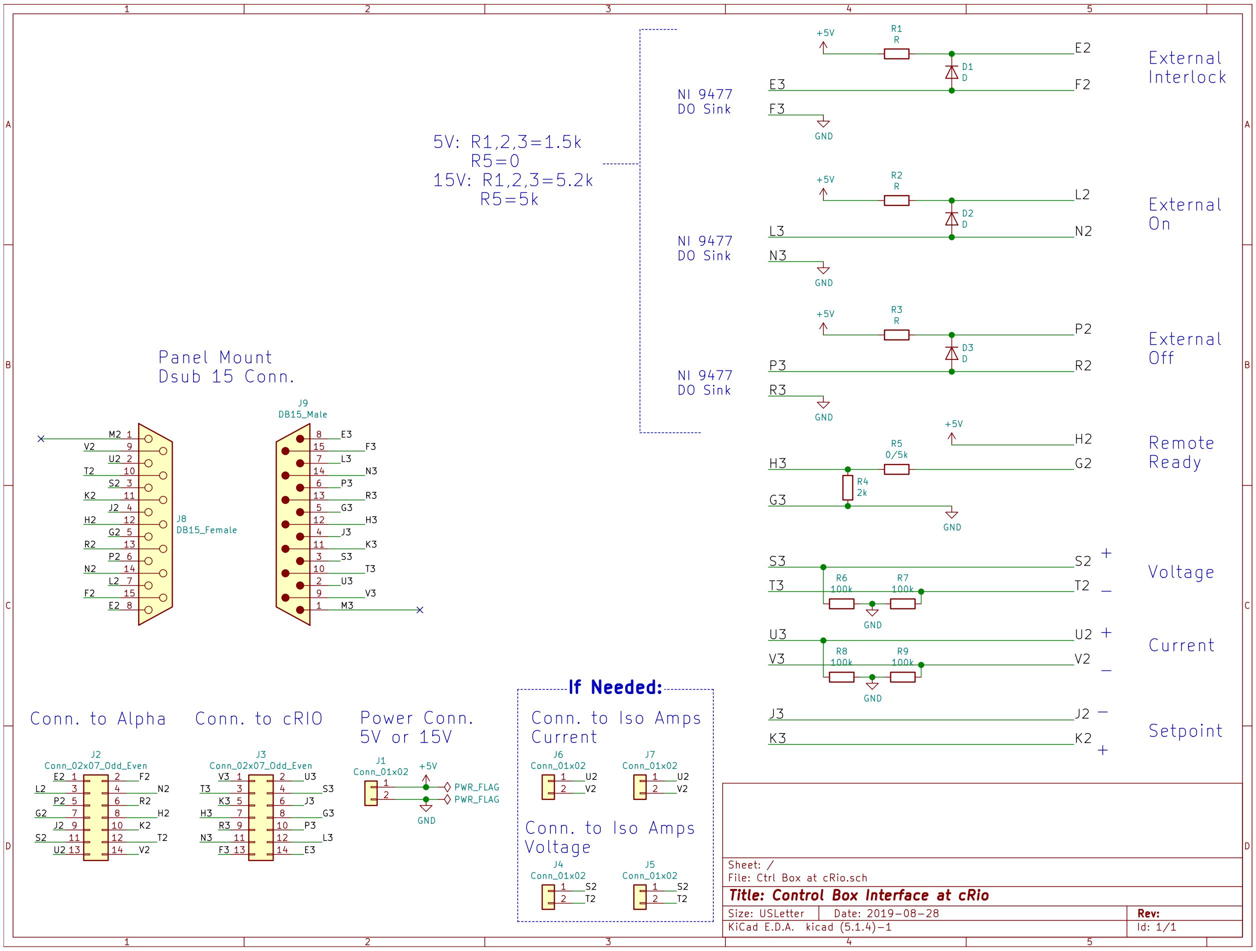

Figure B.4: Schematic diagram of the Alpha control interface sitting at the cRIO.

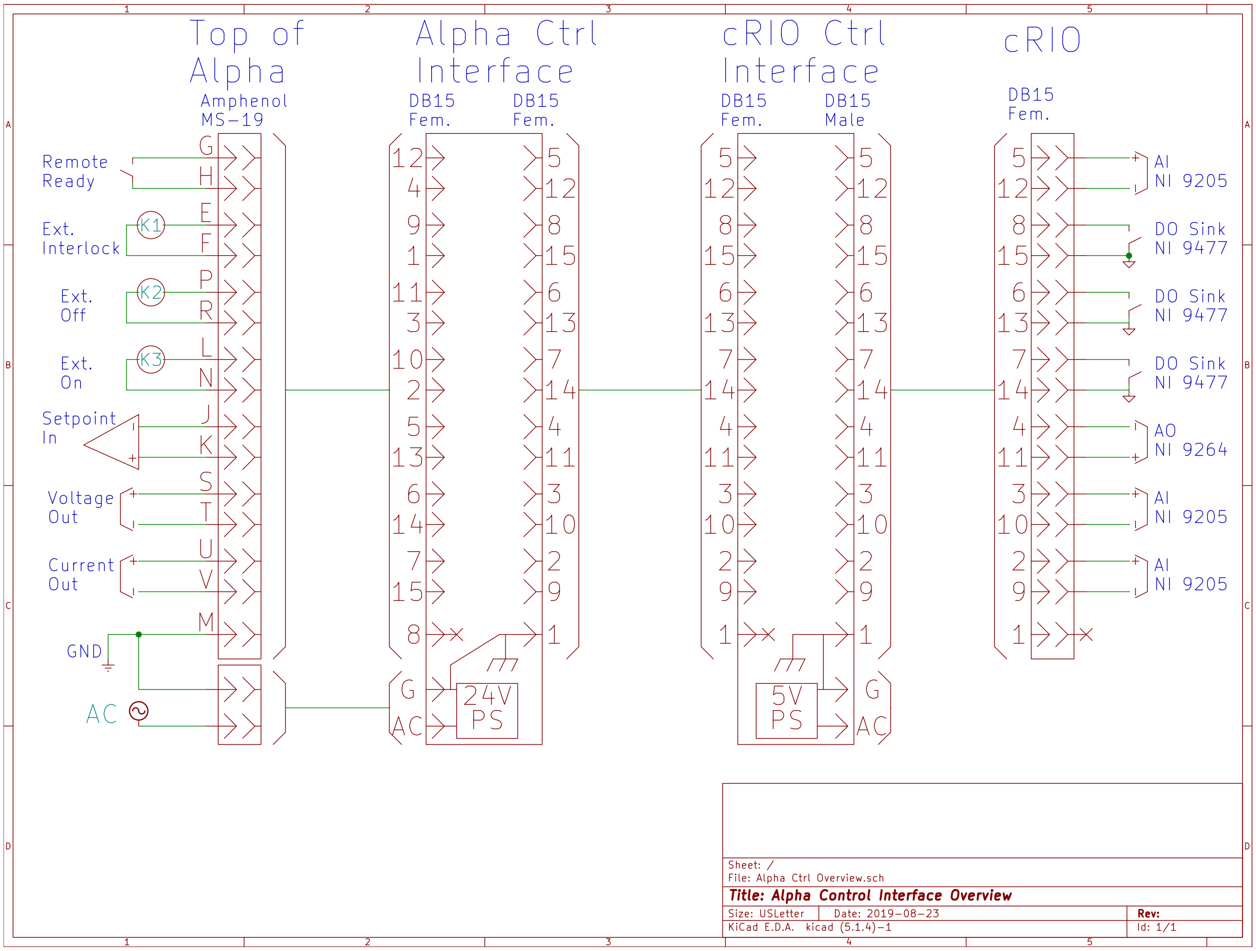

Figure B.5: Overview of the cabling and connections between the various control interfaces for the Alpha power supplies.

Appendix C:
Capacitor Charging Supply Schematics

A simplified diagram for the discharge circuit used in the later TREX experiments is discussed in Section 5.1. This appendix describes the peripheral electronics used to charge and control the capacitor bank, designed and built by the author. This system, shown in Fig. C.1, is centered around a powerful CCDS power supply from General Atomics Electronics Systems able to charge at a constant 4 kJ/s rate (constant current). To ensure there is no feedback onto the power supply when the drive circuit is pulsed, potentially damaging the charging circuit, the output of the power supply is only connected to the capacitors through two high voltage vacuum relays which are disengaged once the capacitors reach the set voltage. A small capacitor sits directly across the CCDS output, after a current limiting resistor and flyback diode, provides a safety load in the case that the relays fail to close. A $100\ \Omega$ dump resistor is connected through a normally-closed Ross relay for appropriate discharging of the capacitors.

A control circuit, shown in Fig. C.2, was created to interface between the BRB cRIO control system and the CCDS power supply. This circuit utilizes simple relays and voltage transducers to keep the two system electrically isolated and limit ground loops that could potentially develop. Descriptions of each pin in the cable going to the cRIO are shown in Table C.1. In addition to the 25 pin interface between the control box and the power supply, there are also control signals for the relays used for to engage the engage the output and the dump resistor. Microswitch interlocks connected to each relay ensure proper sequencing of events and to limit the possibility of harm to any of the major components if some part of the sequence is not working properly. The full charging and discharging sequence is described below.

TREX drive circuit charging and discharging operation.

1. The End of Charge (EOC) Reset signal is set, momentarily enabling relay K1 which in turn enables relay K3. K3 remains engaged as the EOC indicator (Pin 13 of DSUB25) is pulled to ground.
2. The Remote Set Point is programmed.
3. The dump relay is opened, closing its microswitch.
4. The high voltage relays are closed, connecting the power supple output to the capacitors and closing the two relay microswitches.
5. The High Voltage On signal is set, but only reaches the CCDS PS if all the microswitches are properly closed.
6. The CCDS PS charges the capacitors to the programmed voltage. The time it takes depends on the size of the capacitor bank.
7. The EOC indicator is lifted from ground by the CCDS PS, disengaging relay K3 which automatically disengages the high voltage relays and disconnecting the power supply output from the capacitor bank.
8. The capacitor bank is either triggered properly or the shot is aborted.
9. The dump relay is close, discharging the remaining voltage on the capacitors.
10. The sequence is repeated when the next experimental shot is ready.
11. The capacitor voltage is actively monitored while the power supply is operating.

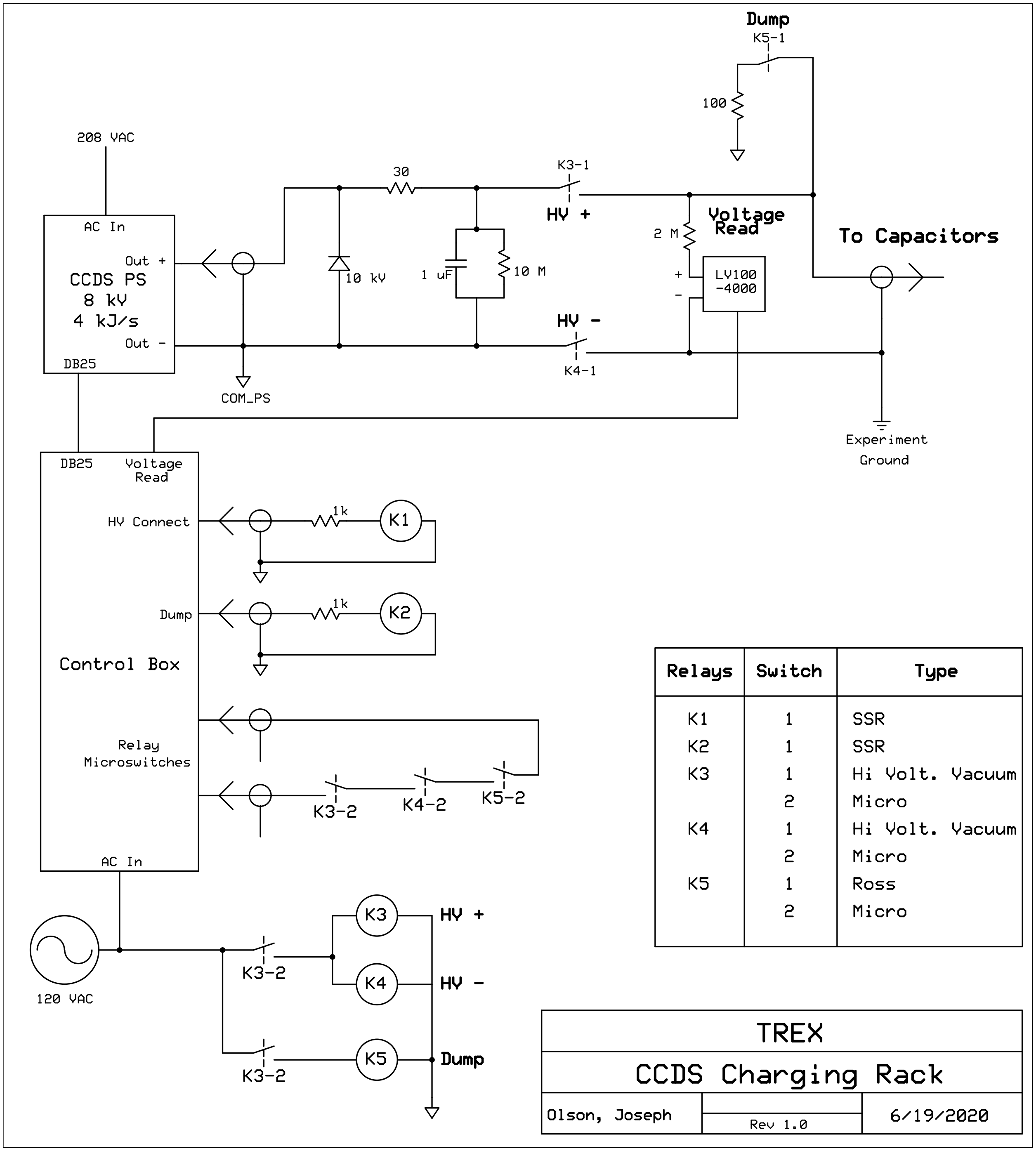

Relays	Switch	Type
K1	1	SSR
K2	1	SSR
K3	1	Hi Volt. Vacuum
	2	Micro
K4	1	Hi Volt. Vacuum
	2	Micro
K5	1	Ross
	2	Micro

Figure C.1: Schematic drawing of the CCDS charging rack.

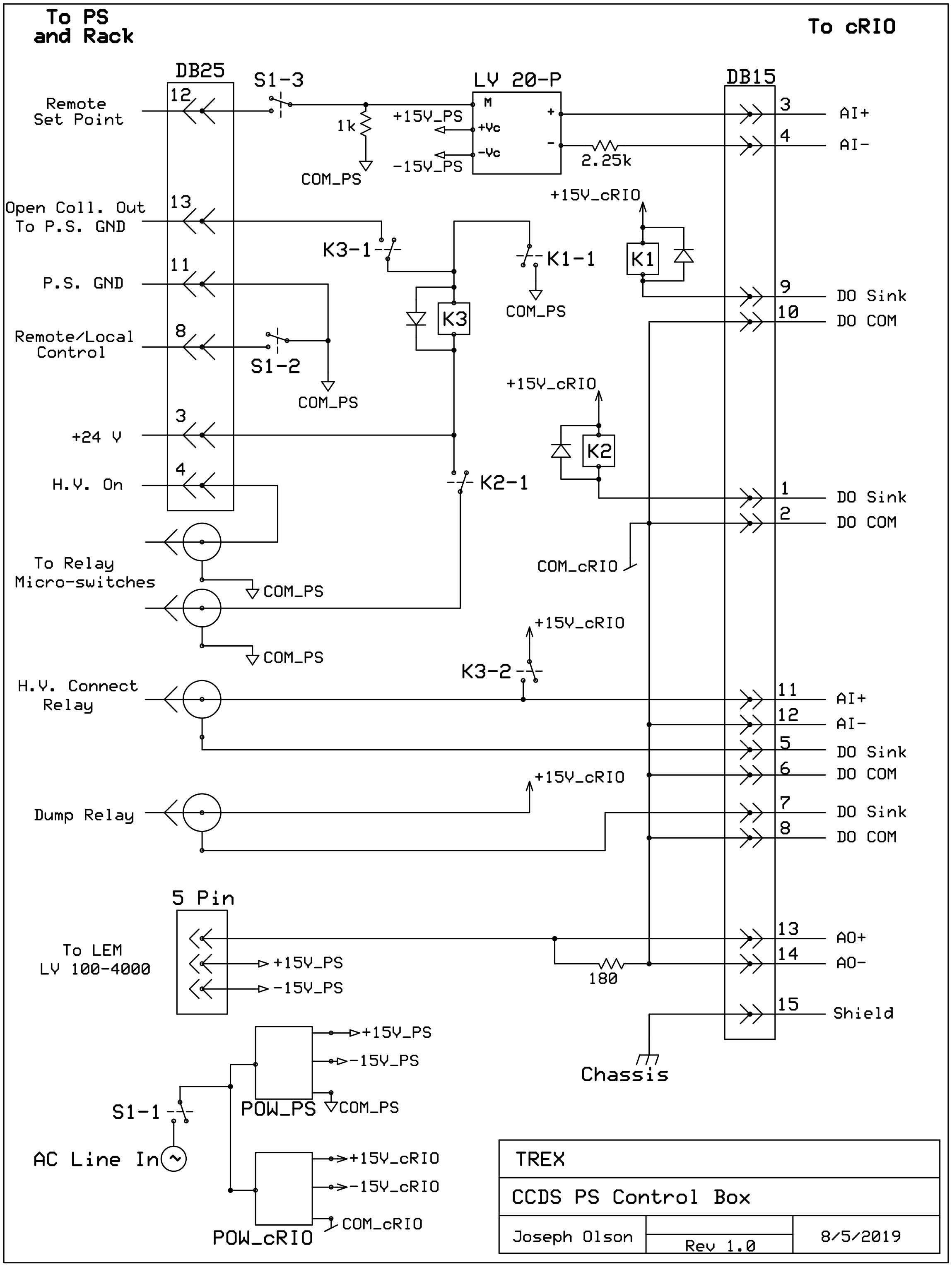

Figure C.2: Schematic drawing of the control interface for the CCDS charging rack.

Function	DSUB15 Pin Num.	cRIO Module	Module Channel
High Voltage On	1. DO + 2. DO Com	NI 9477	DO3
Remote Set Point	3. AO + 4. AO Com	NI 9264	AO2
High Voltage Relay Engage	5. DO + 6. DO Com	NI 9477	DO20
Dump Relay Engage	7. DO + 8. DO Com	NI 9477	DO4
End of Charge Reset	9. DO + 10. D0 Com	NI 9477	DO19
End of Charge Indicator	11. AI + 12. AI −	NI 9205	ACH6
Capacitor Voltage Reading Output	13. AI + 14. AI −	NI 9205	ACH7
Shield	15. No Conn.		

Table C.1: Descriptions of the DSUB15 interface cable from the CCDS control box to the cRIO.